UNIVERSITÀ DEGLI STUDI DI ROMA
“LA SAPIENZA”

The electron-phonon interaction in strongly correlated electron systems

Thesis submitted for the degree of
Doctor Philosophiæ

Candidate

Giorgio Sangiovanni

Advisors

Dr. Massimo Capone
Prof. Claudio Castellani

Roma - Ottobre 2004
DOTTORATO IN FISICA - XVII ciclo
Coordinatore: Prof. Valeria Ferrari

Contents

Chapter 1

Introduction

1.1 Plan of the work

The purpose of this work is to analyze the properties of a strongly correlated electron system coupled to phonons.

In the **first chapter** we introduce the main motivations for such a study and give a brief overview of the materials for which this investigation is thought to be relevant.

Chapter 2 contains a review of some of the known results about the electron-electron and the electron-phonon interactions, and can be therefore skipped by the expert reader. The Hubbard-Holstein model, used to describe a coupled electron-phonon system in the presence of strong correlation, is introduced. We also discuss the approach used to solve it, the Dynamical Mean Field Theory, and present the numerical techniques which we have applied.

The core of the work is represented by **Chapter 3** and **4**. The results about the electron-phonon interaction close to the Mott transition, reported in two recent works, are presented in these two chapters [1, 2].

Chapter 5, extending to finite temperature a previous result on the Holstein model [3], addresses the issue of retardation and its influences on the local magnetic moment formation in the Hubbard model. The results presented here are still unpublished [4].

The last part of the work contains the **Conclusions**, an two **Appendices**. In the first one we calculate the Kondo coupling in the presence of the electron-phonon interaction and in the second one, we derive a general criterion for pair formation at finite temperature.

1.2 Strongly correlated systems and high temperature superconductivity

High-temperature superconductivity and, in particular, the physics of the cuprates occupy a central role in solid states physics and attract the efforts of a big part of the condensed matter community. Nowadays, after almost twenty years of investigations, a theory which explains their rich phase diagram and their many anomalies is still lacking.

There are many points of view and lots of different approaches to this challenging problem. In this work, we focus on two of the most important properties of these materials:

First of all, the cuprates are Mott insulator, i.e. materials in which the Coulomb repulsion between electrons is large and is able to immobilize the carriers in the case of an half-filled band. This has an influence in the whole phase diagram, where *d*-wave superconductivity is found and, at higher temperatures, the so-called pseudogap appears. This is a depression of spectral weight at the Fermi level in absence of an obvious broken symmetry, which shows up in different physical quantities and gives the anomalous metallic behavior, characteristic of lightly doped cuprates.

The second point is the role of the lattice degrees of freedom: There are in fact a number of indications of the presence of a substantial electron-phonon coupling in these compounds, although its role is still unclear. What we can say is that, in the cuprates, the electron-phonon interaction has a different behavior than in conventional weakly-correlated material and, although not necessarily directly connected with the superconducting mechanism itself, it constitutes one of the relevant open issues in the physics of the cuprates.

In this Introduction we want to discuss how and to which extent the two aspects, namely the strong correlation and the electron-phonon coupling, are relevant for the physics of the cuprates. In this section we focus on the consequences of strong correlation, while, in the second, on the most recent experimental evidences about the electron-phonon interaction in the cuprates.

In Fig. 1.1 we show a schematic phase diagram of the cuprates. The undoped compound is a Mott insulator with antiferromagnetic order. This is rapidly destroyed with increasing doping and the superconducting “dome” appears. The highest critical temperature, which, in some cases can reach more than 100K, is achieved for a value of the doping between 15% and 20%, called optimal doping.

The physics of cuprates is strongly influenced by their highly anisotropic structure in

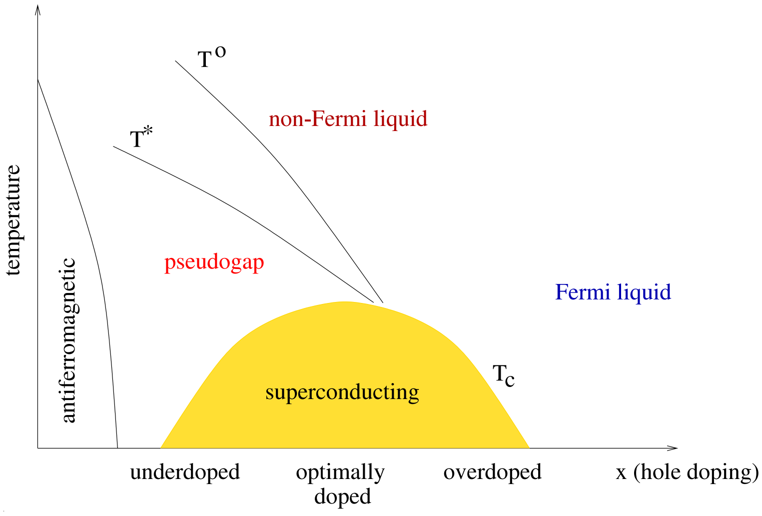

Figure 1.1: Schematic phase diagram of the cuprates

which two-dimensional Copper-Oxide planes are separated by layers of other atoms (Ba, O, La,...). In addition, a large local Coulomb repulsion is present on the Cu sites. In other words, the main characteristic of these compounds is the presence of strong correlation, directly confirmed by the existence of the Mott insulating phase at half-filling. At half-filling, the localized spins on the Cu sites align with antiferromagnetic long-range order, as predicted by the simplest description of a strongly correlated system: the Hubbard model [5]. Indeed, in the limit of large electron-electron repulsion U, the Hubbard model maps onto an antiferromagnetic Heisenberg model at half-filling, with coupling given by $J = 4t^2/U$, where t is the hopping amplitude. In the case of the cuprates at half-filling this description works, in fact, very well [6].

When these materials are doped by chemical substitution, the added holes are mainly localized on the Oxygen sites, making the description in terms of a single band model less founded. Nevertheless, as showed by Zhang and Rice [7], the more realistic three-band model, in which the Oxygen's p_x and p_y orbitals are considered along with the Cu d orbital, can be reduced, out of half-filling, to an effective single-band one. Many studies focused, in fact, on the Hubbard model, viewed as an effective single-band model for the cuprates, as well as on its large-U limit for finite doping, the t-J model. In the original P. W. Anderson's idea [8], the t-J model is the ideal framework to explain the presence of two apparently inconceivable phenomena in the phase diagram of the cuprates: the Mott insulating state and superconductivity. This is based on the concept of spin-charge separation and the existence of a resonating valence bond (RVB) state made of spin singlets between neighboring sites. Remarkably, the d-wave symmetry of the superconducting state comes also naturally from the presence of the J-term [9].

The connection between high-temperature superconductivity and strong correlation is confirmed by many other experimental evidences in the cuprates, in addition to the direct observation of the Mott insulating phase at half-filling. The main ones are the narrow electronic bands found by angle resolved photoemission spectroscopy (ARPES), the small weight of the coherent quasiparticle excitations and of the superfluid density, the pseudogap...(for a review see Ref. [10]).

Within the simple single-band Hubbard model, some of the characteristic of the cuprates as strongly correlated superconductors can still be captured [11]. In particular, the results of a variational Monte Carlo study on the Hubbard model are in agreement with some of the properties of the cuprates, like the non-monotonic behavior of the order parameter, the existence of a scale which monotonically decreases with doping, like T^* and a quasiparticle weight proportional to the doping level, in the nodal directions where the d-wave gap vanishes [12]. These studies were carried out assuming a large value of the electronic repulsion (more than one time the bandwidth).

All the anomalous characteristics of the cuprates we have mentioned present clear deviations from the Fermi liquid paradigm which rules the physics of standard metals. These violations becomes less pronounced with increasing doping, and, only in the deeply overdoped region, the Landau theory of Fermi liquid is recovered. This shows how much the physics of the cuprates is influenced by the presence of a sizable U, despite the effect of correlation is, in general, less important the farther one goes from half-filling. In any case, a theory entirely relying on electronic correlation, does not explain the highly unconventional physics of these compounds.

The discovery of superconductivity in other system, like the fullerenes, where electron-electron repulsion is also sizable and the superconducting state, with s-wave symmetry, is of clear electron-phonon origin, has triggered many theoretical studies of coupled electron-phonon systems in the presence of strong correlation. Recently, a scenario in which high-temperature superconductivity is driven by strong correlation has been formulated within a multi-band Hubbard model with a negative Hund-rule term [13, 14]. In that context superconductivity is found close to the Mott transition and it is enhanced by the presence of a strong Hubbard repulsion, leading to a theory of strongly correlated superconductivity which shares many similarities also with the idea of an RVB state in the cuprates.

In the next section we will show that there are evidences for which purely electronic interactions are not the only ingredient in the physics of cuprates. A sizable electron-phonon coupling has been detected, in fact, by different experiments. Nevertheless its features are contradictory: substantial isotope effects are visible on quantities like the pseudogap temperature and the superfluid density, while signs of phononic scales are almost unrecognizable in resistivity and the superconducting transition temperature is only weakly dependent on the mass of the ions.

While the role played by the electron-phonon interaction in the cuprates continues to be highly debated, a theory which explains the behavior of the electron-phonon interaction in the presence of a strong electronic repulsion has not yet been formulated. Therefore in this work we study the Hubbard-Holstein model within a non-perturbative framework trying to understand the non-trivial competition between the two interactions. We believe that this study can guide us in the difficult task of understanding the puzzling properties of the electron-phonon interaction observed in cuprates.

1.3 Experimental evidences of lattice effects and electron-phonon interaction in cuprates

In this section we give a brief description of the recent evidences of lattice effects in the cuprates and point out the inadequacy of standard theories of coupled electron-phonon systems in explaining these experimental results.

These evidences come from different experiments on the various cuprates. The first ones focused on the isotope effect on the transition temperature T_c. Nevertheless, differently from the case of conventional superconductors, the effect has been found either tiny [15] or, in any case, smaller than in the BCS theory [16, 17]. On the other hand, it turns out that other quantities, like the in-plane penetration depth, are more sensible to isotope substitution than T_c, as evidenced through magnetization measurements [18], torque magnetometry experiments [19] and muon spectroscopy [20]. The isotope effect on the superfluid density and on the effective mass of the quasiparticles can be obtained from these measurements and it has been argued that the isotope effect on this last quantity, for underdoped $\mathrm{YBa_2Cu_3O_7}$, is of the order of 5% [21]. Such an influence of phonons on

m^*, is quite surprising for two reasons: the first one is that the Migdal-Eliashberg theory for the electron-phonon interaction predicts that m^* does not depend at all on the mass of the ions [22, 23]; the second reason is that the large values assumed by the effective mass in the cuprates are mainly due to correlation effects. Nevertheless, anticipating here the results of Chapter 3, we will see that it is possible, starting from an Hubbard model with an electron-phonon coupling and treating the two interactions non-pertubatively, to obtain large isotope effects on quantities whose absolute value is entirely determined by correlation alone, like the quasiparticle effective mass [2].

A dependence on the mass of the Oxygen atoms has been observed also in the pseudogap temperature T^*, which shows a larger effect, compared to that of T_c. More interestingly, the shift on T^* has the opposite sign with respect of that of T_c [24]. A justification of this phenomenon has been given in a recent work by Andergassen *et al.* [25], but, we have to say that a general explanation of the dependence of the various quantities on the ion's mass, in the cuprates, is far from being obtained. The inclusion of effects beyond the Migdal-Eliashberg theory is instead the key point of a different work, which tries to explain the anomalous isotope effects observed in cuprates within the non-adiabatic theory of the electron-phonon interaction [26].

Leaving the issue of isotope effect, we now want to mention other experiments indicating the presence of a substantial electron-phonon coupling in the cuprates.

Phonon branches measured by inelastic neutron scattering can be, in most cases, quite well reproduced by models based on interaction potential, including also screening effects [27, 28]. A notable exception is constituted by a high energy ($\sim$ 70-80 meV) in-plane bond-stretching phonon mode, the half-breathing mode, which anomalously softens, along the [100] direction, upon doping [28, 29, 30]. In Fig. 1.2, the frequency of this high energy longitudinal optic phonon branch in $\mathrm{La}_{2-x}\mathrm{Sr}_x\mathrm{CuO}_4$ is reported, as found in Ref. [29].

The interest in these experimental results grew immediately. Such a strong renormalization of the phonon frequency of an undoped system upon adding free carriers, is, in fact, an indication of a strong coupling to the correspondent phonon mode. Moreover it has been suggested that this mode favors charge ordering [29]. Stripe patterns with periodicity of $4a$ would be, in fact, related to the lattice distortion with $\mathbf{q}$=($\pi/2a$,0,0) ($\zeta = 0.25$ in the notation of Fig. 1.2), as it can be seen in Fig. 1.3. Although we have not discussed it in this introduction, the presence of one-dimensional charge textures (stripes) is a largely debated issue in the physics of the cuprates, so it is easy to understand the interests in

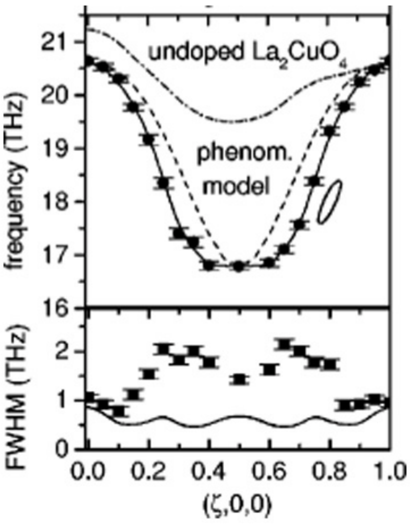

Figure 1.2: Dispersion of the highest longitudinal optic phonon mode in $La_{2-x}Sr_xCuO_4$ from Ref. [29] as function of the wave vector **q**= (ζ,0,0)$2\pi/a$. Bottom: linewidths determined by fitting a Gaussian line shape to the observed profiles.

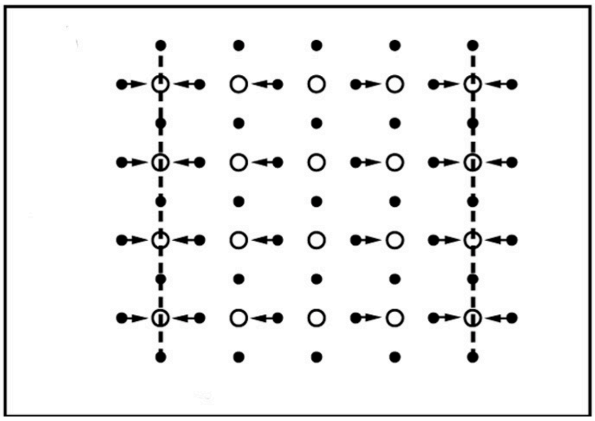

Figure 1.3: Half-breathing longitudinal optic phonon mode for $\mathbf{q} = (\pi/2a, 0, 0)$. Full dots and open circles depict, respectively, O and Cu atoms. The dashed lines denote positions where an extra charge will be dynamically accumulated on the Cu atoms due to the displacements of the neighboring O atoms. The in-plane motion of Oxygen atoms, described by $\exp[i\mathbf{q}\cdot\mathbf{r}]$, is represented here by the function $\cos[(\pi/2a)\cdot na - \pi/4]$.

these experimental findings.

Other observations in optimally-doped $YBa_2Cu_3O_7$ show that, in this compound, the in-plane Oxygen bond-stretching mode has a very steep dispersion along the [100] and [010] directions [31], while, the [110] direction is much less anomalous. Therefore, the main characteristic of this phenomenon, which seems to be common to Cu-O planes of the cuprates, is the strong anisotropy between the [100] and the [110] directions. Along this latter direction, in fact, the phonon renormalization is much weaker with respect to [100] one. An explanation of this unconventional behavior has been given within the t-J model with electron-phonon interactions derived from a three-band model [32].

The last result we want to discuss comes from recent photoemission studies. ARPES measurements on different cuprates have, in fact, evidenced the presence of a "kink" in the electronic dispersion. The first indications came from the nodal direction [33, 34, 35] where the kink near 70 meV was observed both in normal and superconducting samples. Further studies have shown a similar phenomenon also near the anti-nodal point (π,0) [36]. Similarly, a sharp feature in the self-energy has been observed in optical measurements [37].

In Fig. 1.4 we report the dispersions obtained by Zhou and co-workers [35], in $La_{2-x}Sr_xCuO_4$ along the nodal direction and at a temperature of 30K. It can be seen that the position of the kink is almost fixed at 70 meV independently of the doping level. This has been interpreted as the signature of coupling to the same half-breathing in-plane Cu-O bond-stretching phonon detected by inelastic neutron scattering.

Although for the anti-nodal kink other explanations, involving spin degrees of freedom, have been given [38] and a partial agreement with experiments has been found invoking charge-order fluctuations [39], the phononic origin of the nodal kink seems founded (see Ref.[40] for a related discussion). Nonetheless, the phononic point of view poses a number of questions, which are far from being clarified: it requires a strong anisotropy of the electron-phonon interaction to account for the different behavior between the nodal and the anti-nodal direction and it is difficult to reconcile with the fact that the high energy part of the dispersion anomalously depends on doping while, closer to Fermi level, the band remains almost untouched. The anomalous behavior of the high energy part of the dispersion has been also evidenced in a more recent study on isotope substitution in optimally doped $Bi_2Sr_2CaCu_2O_{8+\delta}$ [41]. The temperature dependence and the evolution of the kink from the nodal to the anti-nodal direction are analyzed, but other experimental

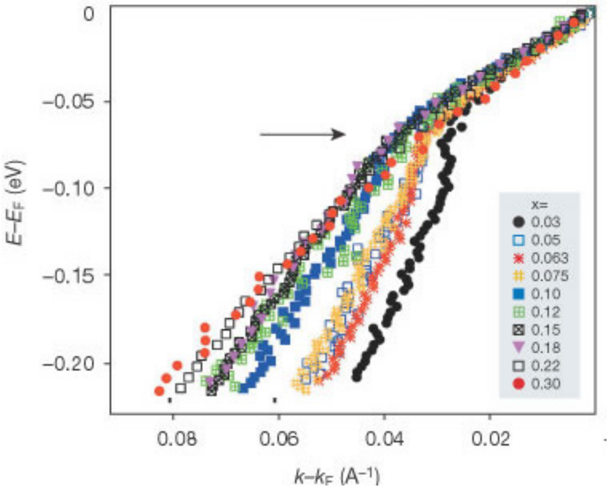

Figure 1.4: Electronic dispersion in $La_{2-x}Sr_xCuO_4$ measured at $T = 30$K along the nodal direction. From Ref. [35].

data are needed in order to shed some light on the interpretation of these results.

In this introduction we have shown that the various evidences about the presence of a substantial electron-phonon coupling in cuprates are difficult to arrange in a consistent framework and are apparently in direct contradiction with other experimental results, like, for example, the perfectly linear resistivity as a function of temperature observed at optimal doping.

From the theoretical side, a full comprehension of a coupled electron-phonon systems in the presence of a strong electronic correlation still lacks. Although nowadays many things are well established when the two interactions are considered separately, the full problem is relatively new in the literature and rises many compelling questions. The search for the answers to these open issues constitutes the main motivation for the present work.

Chapter 2

The Hubbard-Holstein model

2.1 General properties and techniques

A strongly correlated system coupled to phonons can be described through the Hubbard model supplemented by a Holstein coupling term. This is called the single-band Hubbard-Holstein model: The Hamiltonian is made by a kinetic tight-binding term, a local Coulomb repulsion between the electrons and dispersionless Einstein phonons coupled to the local electronic density. The Hubbard-Holstein model is clearly a highly simplified description both of the electron-electron and the electron-phonon interaction, but it is expected to contain the most relevant ingredients of a system in which the electrons experience, at the same time, an instantaneous short-range repulsion and a retarded attraction mediated by local lattice vibrations.

As we will see throughout this work, this model has a very rich phase diagram where the presence of many energy scales leads to the existence of a large number of competing phases. Our study focuses on the paramagnetic and non-superconducting sector of the Hubbard-Holstein model, where the interesting physics of the transition between the metal and the Mott insulator emerges, not hidden by broken-symmetry phases. In particular, we will extensively study the strongly correlated regime in the presence of a moderate electron-phonon coupling. We will also focus on the opposite case, in which the electron-phonon interaction is more relevant than the electron-electron repulsion, and in the final chapter of this work, we will extend the analysis at finite temperature, without considering the Coulomb repulsion.

The Hubbard-Holstein model represents an ideal playground where the interplay between the repulsive Hubbard interaction and the retarded attractive one mediated by phonons can be studied, evidencing the non-trivial effects coming from their competition. This is important, as we have discussed in the first chapter, for the physics of the cuprates, where the mutual influence of strong correlation and electron-phonon interaction is a relevant point, and it also constitutes a challenging issue as a pure theoretical problem.

In this chapter we describe the Hubbard-Holstein model and the early approaches used to solve it; then we introduce the method that we will use to investigate it, beyond the perturbative level: the Dynamical Mean Field Theory.

2.1.1 Electron-electron correlation

The electronic term is described through the repulsive Hubbard model, whose Hamiltonian reads

$$H = -t \sum_{\langle i,j \rangle \sigma} \left(c^{\dagger}_{i\sigma} c_{j\sigma} + c^{\dagger}_{j\sigma} c_{i\sigma} \right) + U \sum_{i} n_{i\uparrow} n_{i\downarrow} \tag{2.1}$$

where $c_{i\sigma}$ ($c^{\dagger}_{i\sigma}$) are destruction (creation) operators for fermions with spin σ on site i and t is the hopping amplitude. The typical electronic scale is set by the non-interacting half-bandwidth D, which is proportional to the hopping amplitude t.[1].

Formulated independently by Hubbard [5], Gutzwiller [42] and Kanamori [43], the Hubbard model, although relatively simple, is not exactly solvable, except in the peculiar one-dimensional case. It has been introduced to capture the basic mechanism of the transition between a metallic and a localized insulating state, driven by a local electron-electron repulsion, as argued in the early proposals given by Peierls and then by Mott [44, 45]. In the paramagnetic sector, in fact, the main ingredient of the Hubbard model is the competition between the kinetic term, which tends to delocalize the electrons, and the local repulsion which opposes this tendency by imposing constraints on the electron motion. In fact, the hopping of an electron to a single-occupied neighboring site has an energy cost of U, so, if the repulsion is large with respect to the hopping amplitude, the system is insulating at half-filling. The parameter which rules this competition is thus

- $u = \frac{U}{D}$ - degree of correlation (ratio of the Hubbard repulsion to the semi-bandwidth)

A different idea of a metal-insulator transition, originally introduced by Slater [46], is associated to an effective doubling of the unit cell caused by the antiferromagnetic ordering. In the Hubbard model, in fact, depending on the kind of lattice and on the dimensionality,

---

[1] The coefficient relating the half-bandwidth D to the hopping t depends on the dimensionality and on the type of lattice used

the Mott transition can be hidden by the presence of antiferromagnetic long-range order. For the Hubbard model on a d-dimensional (hyper)cubic lattice with nearest neighbor hopping only, for example, the ground state is insulating for arbitrary small U, and it is always antiferromagnetically ordered at half-filling. Therefore the Mott transition is not visible unless one introduces a mechanism for frustrating the antiferromagnetic order (for example, with the inclusion of next-nearest neighbor hopping or considering different kinds of lattice).

Nevertheless, the reason why a full description of the Mott transition has been given only recently after the introduction of the Dynamical Mean Field Theory [47], comes from another fact. The difficulty is found, in fact, in the, already mentioned, non-trivial competition between the kinetic and the interaction terms, on which resides the non-perturbative character of the phenomenon. In the early approaches to the solution of the Hubbard model, one of the two limiting cases was chosen and then one moved towards the transition introducing perturbatively the missing physics. These methods fail when they are used too far from their starting point and give necessarily a partial description of the transition. Nevertheless they have been useful to gain physical insight of this phenomenon and to describe the two sides of the transition separately. It is therefore useful to give a brief description of two of these early approaches.

The first one, introduced by Hubbard himself [5], starts from the insulating side of the transition and describes it introducing an effective band picture. The density of states (DOS) of the insulator is made by two bands centered at $\pm U/2$ of width W, associated respectively to holes (lower band) and doubly occupied sites (upper band). The gap between the bands is of the order of $U - W$. Decreasing U the gap shrinks, up to a critical value $U \simeq W$ for which the gap closes. The metal-insulator transition is associated with the closure of the Hubbard gap, when the two bands merge giving rise to a metal.

In the scheme introduced by Brinkman and Rice [48] instead, the transition is approached from below, i.e. from the metallic side. The metallic Fermi liquid phase obtained for small U is renormalized by the interaction. Using the Gutzwiller approximation [42], it is found that the number of double occupied sites, in the paramagnetic phase, goes to zero for $U = U_{BR}$ [48] and the transition is obtained when the effective mass diverges ($m^*/m \propto (U - U_{BR})^{-1}$) and the metallic phase is destroyed. This approach therefore describes the opposite side of the transition with respect to the Hubbard picture and correctly treats the low energy physics in the metallic phase.

A step forward is possible with the introduction of the slave boson technique. In the Kotliar-Ruckenstein approach, the original interacting fermionic problem is represented through a mixed fermionic and bosonic Hamiltonian in which the bosons are auxiliary fields, which label empty, doubly occupied and singly occupied sites [49]. The fermions can be integrated out from this new action to give a pure bosonic one, on which the saddle-point mean-field approximation gives the result of the Gutzwiller approximation. One can proceed beyond the mean-field level and take into account the fluctuations of the bosonic fields, but this is a hard problem to handle in practice and a real new perspective of the Mott transition is not easy to obtain along this line. It has been shown, anyway, that fluctuations around the saddle-point reconstruct the lower and the upper Hubbard bands, and that the disappearance of the metallic peak coincides with the closure of the gap [50, 51].

The main difficulties encountered in the study of the Mott transition come therefore from the non-perturbative nature of this phenomenon which poses serious technical problems. As a consequence, after the original ideas and, subsequently, the first experimental evidences for the existence of a Mott transition in V_2O_3 [52], a relatively long time has passed before a satisfying description of the metal-insulator transition driven by the correlation has been given. This was obtained within the Dynamical Mean Field Theory, as we will see later in this Chapter [47, 53]. Nowadays, the existence of a Mott transition is well established in other transition-metal oxides as well as in other compounds like some organic materials [54, 55].

2.1.2 Electron-phonon coupling

The interaction with the lattice is introduced through the Holstein model [56, 57], in which the local electronic density in coupled to disperionless Einstein phonons. Its Hamiltonian reads

$$H = -t \sum_{\langle i,j \rangle \sigma} \left(c^{\dagger}_{i\sigma} c_{j\sigma} + c^{\dagger}_{j\sigma} c_{i\sigma} \right) - g \sum_{i} n_i (a_i + a^{\dagger}_i) + \omega_0 \sum_i a^{\dagger}_i a_i \tag{2.2}$$

It contains an hopping term for the fermions, already introduced for the Hubbard model (2.1), with an amplitude t. a_i ($a^{\dagger}_i$) are destruction (creation) operators for local vibrations of frequency ω_0 on site i and g is the coupling constant between the electronic density and the local displacement. $n_i = c^{\dagger}_{i\uparrow} c_{i\uparrow} + c^{\dagger}_{i\downarrow} c_{i\downarrow}$ is the total electronic density at site i.

A coupling constant which does not depend on the mass M of the harmonic oscillators can be defined:

$$g' = g\sqrt{2M\omega_0} \tag{2.3}$$

In terms of the phonon coordinates $X_i = \left(a_i + a_i^\dagger\right)/\sqrt{2M\omega_0}$, the coupling term can be written therefore as $-g'\sum_i n_i X_i$ and the pure phononic part in (2.2) becomes equal to $\sum_i \left(P_i^2/2M + KX_i^2/2\right)$, where $K = M\omega_0^2$ and P_i are the conjugate momenta[2]. Since the phononic degrees of freedom enter quadratically into the problem, it is possible to integrates them out from the action. The result is a dynamical density-density interaction between the electrons of the form

$$V_{el-ph}(\omega) = -\frac{g^2\omega_0}{\omega_0^2 - \omega^2} = -\frac{\lambda D}{2}\frac{\omega_0^2}{\omega_0^2 - \omega^2} \tag{2.4}$$

Since the local phonon coordinates X_i are coupled to the total density $n_{i\uparrow} + n_{i\downarrow}$ at each site, the dynamical interaction (2.4) coming out from the integration over X_i, acts between electrons with opposite spin, as well as with parallel spin.

In the last identity of Eq. (2.4) we have introduced the standard dimensionless electron-phonon coupling

$$\lambda = \frac{2g^2}{\omega_0 D} \tag{2.5}$$

which is the ratio between characteristic lattice and electronic energy scales. There are two other important quantities for the Holstein model:

- $\gamma = \frac{\omega_0}{D}$ - adiabatic parameter (ratio of the phonon frequency to the semi-bandwidth)
- $\alpha = \frac{g}{\omega_0}$ - parameter associated to the lattice displacement (ratio of the coupling constant g to the phonon frequency)

The value of γ is a ratio between the electronic and the phononic time scales: for $\gamma \ll 1$ the regime is called adiabatic and the dynamics of the phonons is slow compared to the typical kinetic energy of the electrons. Exactly in the adiabatic limit ($\gamma \to 0$, keeping λ constant) the phonon becomes a classical static field and one could proceed by solving the electronic problem at fixed phonon coordinates, as in the Born-Oppenheimer approximation, and then average over the coordinates. The motion of the electrons is instead slow with respect to the phonon dynamics in the opposite antiadiabatic limit ($\gamma \to \infty$, keeping λ constant), in which the phonon-mediated interaction between the electrons $V_{el-ph}(\omega)$ becomes instantaneous. By looking at (2.4), it is in fact clear that, in the antiadiabatic

---

[2] We work with $\hbar = 1$

limit one obtains an instantaneous interaction and the original Holstein model becomes an attractive Hubbard one, with coupling $U/D = -\lambda$ between electrons with opposite spin.

Away from this two limiting cases, the phonon dynamics plays an important role as well. To measure the strength of the electron-phonon interaction, for instance, one has to consider the coupling constant g together with the phonon frequency ω_0. In fact, although we have generically indicated λ as the "standard" electron-phonon coupling, it has been evidenced in previous studies [58, 59, 60], that λ, which measures the energetic convenience to form a bound state, is the control parameter when γ is small, while, for large γ, the physics is mainly controlled by α. Let us consider the so called Lang-Firsov transformation [61]

$$U = \mathrm{e}^{\alpha \sum_i (a_i - a_i^\dagger)(n_{i\uparrow} + n_{i\downarrow})} \tag{2.6}$$

which shifts the phonon operators:

$$a_i^{(\dagger)} \rightarrow a_i^{(\dagger)} + \alpha(n_{i\uparrow} + n_{i\downarrow}) \tag{2.7}$$

and adds an exponential factor to each fermion:

$$c_{i\sigma} \rightarrow c_{i\sigma}\mathrm{e}^{\alpha(a_i - a_i^\dagger)} \tag{2.8}$$

In terms of these new degrees of freedom, the polarons, the coupling term in the Holstein Hamiltonian (2.2) disappears and the mixing between electrons and phonons enters exponentially in the hopping term. For large γ and in the strong electron-phonon coupling regime, it can be shown that polarons are long-living independent excitations [59]. The effective mass of these mixed quasiparticles has an exponential behavior controlled by α

$$\frac{m^*}{m} = \mathrm{e}^{\alpha^2} \tag{2.9}$$

On the other hand, an analytic solution of the Holstein model cannot be given in the general case. In fact, as in the case of the Hubbard model, one has to deal with an interaction with four fermionic operators, with the additional difficulty of the retardation effect. Nevertheless quite a lot is nowadays known about this model, like, for instance, the possibility of inducing charge-density wave instability, as well as superconductivity [62]. The normal phase of the Holstein model is important as well and its full comprehension is an unavoidable step for the study of the electron-phonon interaction in the presence of the Hubbard repulsion. This, in fact, is known to suppress rapidly these broken-symmetry phases, since it makes charge fluctuations energetically unfavored.

The conventional approach to the weak and intermediate-coupling regimes of electron-phonon interacting systems, is represented by the Migdal-Eliashberg theory [22, 23], in which vertex corrections are neglected assuming a small value of γ. The Migdal-Eliashberg approach is particularly suited to describe superconductivity beyond the BCS level, but it can be successfully applied to the particular case of disperionless Einstein phonons in the normal state. The weak-coupling picture that emerges is characterized by the presence of a Fermi-liquid metallic phase, with the effective parameters renormalized by the electron-phonon interaction (m^*, for example, grows linearly with λ). This picture does not hold for stronger electron-phonon couplings where the Migdal-Eliashberg approach begins to fail because vertex correction cannot be neglected any more. Multiple-phonon contributions to the electronic Green function start to be important and manifest themselves in the spectral properties, as it is captured even by calculations which do not consider vertex corrections [63]. Vertex corrections are instead taken into account in a more advanced formulation [64, 65] in which the regime for intermediate values of γ can be accessed. This approach, still in part analytic, has been applied to the study of superconducting compounds, like the fullerenes and $\mathrm{MgB_2}$, in the attempt to explain their non-standard physics without having to assume an unphysical large value for the electron-phonon coupling λ [66]. In any case, all the perturbative approaches based on the free-electron limit cannot adequately describe the intermediate-strong electron-phonon coupling regime, even if one drastically simplifies the problem by studying the Holstein model with only one electron in the lattice (zero-density case) [56, 57]. Already in this zero-density limit, in fact, the many-body nature of this problem comes out through the dressing of the electron by a multi-phonon cloud which moves coherently with it so as to form a quasiparticle, the polaron, which, in the context of the Holstein model is a short-ranged composite object (small polaron) [59].

From the technical point of view, polaron formation can be studied by looking at the probability distribution function for the phonon field $P(X)$. This function has, in fact, one single peak for $X = 0$, when λ is small, while develops two maxima when λ exceeds the value of the crossover to the polaronic regime. This criterion, also used in the finite density case in which lattice polarization is associated to multi-polaron formation, can be easily understood if one neglects the hopping term in (2.2) and looks for the minima of the potential $V_{at}(X)$, as if the quantum phonons were classical variables:

$$V_{at}(X) = \frac{1}{2} M \omega_0^2 X^2 - g' n X \qquad (2.10)$$

So, although in this "classical" scheme the crossover is described in a simplified way, the connection between the occupation of a lattice site and the distortion of the corresponding local oscillator is correctly captured. The minimum of the parabolic potential, in fact, is shifted for different values of n: If the site is single occupied ($n = 1$), the minimum is for $X_{at}^{(0)} = g'/K$, if it is empty ($n = 0$), one has $X_{at}^{(0)} = 0$, while, if the site is double occupied ($n = 2$), $X_{at}^{(0)} = 2g'/K$. In Fig. 2.1 we show the probability distribution function of the

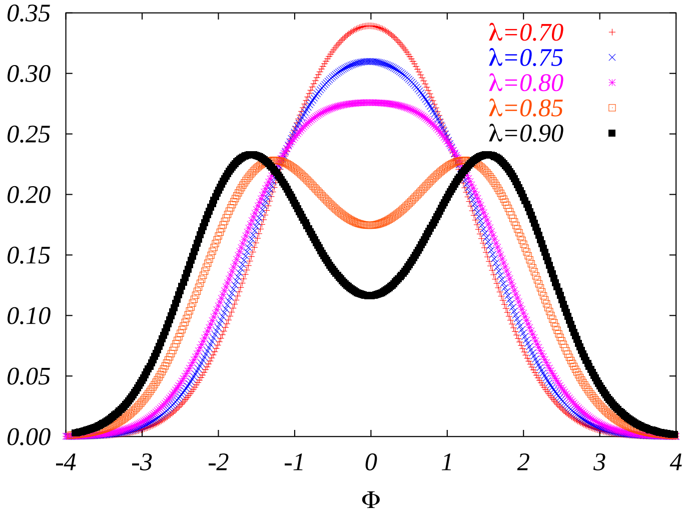

Figure 2.1: Evolution with the electron-phonon coupling λ of the probability distribution function of the field $\Phi = (a + a^\dagger)/\sqrt{2}$ at half-filling for $U = 0$ (pure Holstein case) and $\omega_0 = 0.2D$, calculated with Dynamical Mean Field Theory at zero temperature.

field $\Phi = (a + a^\dagger)/\sqrt{2} = X\sqrt{M\omega_0}$, as calculated within Dynamical Mean Field Theory. After this rescaling and by shifting the curve of the quantity $\alpha\sqrt{2} = \sqrt{\lambda D/\omega_0}$ which makes the distribution symmetric with respect to $\Phi = 0$, one gets, for small λ, the mono-modal shape around $\Phi = 0$. Increasing λ, the shape becomes bimodal. Correspondingly, the probability of having empty and double-occupied sites gets larger, due to the increased attractive interaction. The position of the two peaks increases with λ, as it can be observed in the figure, and eventually reaches the two atomic values $\Phi = \pm\alpha\sqrt{2}$, for larger λ. The crossover takes places where the curvature of the distribution function, for $\Phi = 0$, changes sign.

As we have said, the intermediate region is not accessible with conventional perturbative methods, while, as anticipated in Fig. 2.1, the Dynamical Mean Field Theory, which does not require any kind of expansion around the free-electron limit, successfully describes the polaronic crossover. This has been done, in fact, both in the single-electron case [59] and for finite-density [67, 3], as we will see in the following section, where also the occurrence of the bipolaronic transition and its interplay with the polaronic crossover will be discussed.

To conclude, we recall that the intermediate-strong coupling regime of the Holstein model has been investigated with Monte Carlo methods, both in the one-dimensional [68] and in the two-dimensional case [62]. Furthermore, a very efficient method for the single-electron case is used in Ref. [69, 70], while there are also approaches based on the Lang-Firsov transformation [71].

2.1.3 The electron-electron and the electron-phonon interaction

The full Hamiltonian of the Hubbard-Holstein model reads

$$H = -t \sum_{\langle i,j \rangle \sigma} \left(c^{\dagger}_{i\sigma} c_{j\sigma} + c^{\dagger}_{j\sigma} c_{i\sigma} \right) + U \sum_{i} n_{i\uparrow} n_{i\downarrow} - g \sum_{i} n_i (a_i + a^{\dagger}_i) + \omega_0 \sum_{i} a^{\dagger}_i a_i \tag{2.11}$$

We have seen that this model has many parameters which controls its physics, already introduced and discussed in sections 2.1.1 and 2.1.2.

- $u = \frac{U}{D}$ - degree of correlation (ratio of the Hubbard repulsion to the semi-bandwidth)
- $\gamma = \frac{\omega_0}{D}$ - adiabatic parameter (ratio of the phonon frequency to the semi-bandwidth)
- $\lambda = \frac{2g^2}{\omega_0 D}$ - standard electron-phonon coupling (ratio of the binding energy to the semi-bandwidth)
- $\alpha = \frac{g}{\omega_0}$ - parameter associated to the lattice displacement (ratio of the coupling constant g to the phonon frequency)

This model, although relatively simple, is expected to display a rich physics as a function of these four parameter, to which also the density n, as well as the temperature T should be added. The first difficulty comes, in fact, from dealing with a wide parameter space. For these reason, one usually varies one or, at most, two parameters at the same time, in order to answer to specific questions. As a matter of fact, with this model one could study different unrelated issues, like, for instance, the suppression of superconductivity due to correlation, as well as the effect of the electron-phonon coupling on the antiferromagnetic properties of the Hubbard model. At finite temperature one could analyze, with this model, pairing and the retardation effects, as well as polaron formation, in the presence of an electronic repulsion. The Hubbard-Holstein model can be studied even with a more general perspective, looking at the competition between an instantaneous and local repulsion and an attraction mediated by a boson with a characteristic frequency (see Eq. 2.4). The bosonic mediator could be of unspecified physical origin: phonon, plasmon, a spin mode... Our interest, as already underlined, focuses mainly on the effect of the electron-phonon coupling in the regime close to the Mott transition. The motivation for this choice comes from the challenging field of high-temperature superconducting cuprates. In this compounds the electronic correlation is probably the main ingredient and, as reported recently, there are indications of the presence of a sizable electron-phonon coupling, which seems to manifest differently in the various quantities and with anomalous characteristics. As we will see, this study is naturally carried out within the Dynamical Mean Field Theory, which we will describe in the following section, but other approaches are also used and give interesting results. Among these we recall the slave boson approach, described in Sec. 2.1.1 for the case of the pure Hubbard model. This approach has been successfully applied to the study of the three-band Hubbard-Holstein model in the infinite-U limit [72], of the single-band Hubbard-Holstein model with the further inclusion of long range [73], and, more recently, to the study of the electron-phonon vertex function in the Hubbard model for finite-U [74]. The vertex function has been studied also with another method based on Hubbard's X operators [75].

A very powerful numerical technique for the investigation of interacting many-body systems is Quantum Monte Carlo [76, 77]. Differently from slave-boson treatments, Quantum Monte Carlo directly solves the original model, restricted to a finite lattice and with a finite temperature scale. This method has been recently used for studying the electron-phonon Holstein vertex in the two-dimensional Hubbard model [78]. The main outcome of this analysis is that, the effective electron-phonon coupling, upon increasing the strength of electron-electron repulsion, is initially suppressed and then, in the strong correlation regime, it starts increasing at small phonon momentum transfer. As a consequence, even if the initial value is never overcome, an anomalous non-monotonic behavior of the electron-phonon vertex function is observed.

2.2 Dynamical Mean Field Theory

Dynamical Mean Field Theory (DMFT) is one of the most reliable tools for the analysis of interacting many-body problems, which, in the last years, has given important contributions to the understanding of the physics of strongly correlated systems as well as coupled electron-phonon systems [53, 47]. DMFT is particularly suited for studying problems in which the local correlations constitute the most relevant part, since it maps the lattice model onto a local theory. The advantage with respect to standard mean field approaches is that DMFT preserves the full quantum dynamics of the problem [79].

The comparison between classical mean field description and DMFT can be done in a transparent way by taking, respectively, the Ising and the Hubbard models, as examples for the two approaches. In the case of the Ising model, one has to solve a problem for interacting spins in the presence of an external magnetic field h

$$H = -\sum_{\langle ij \rangle} J S_i S_j - h \sum_i S_i \tag{2.12}$$

In the mean field approach, the interaction term between spins on nearest-neighbors sites is replaced by a much simpler one in which a single special spin is coupled to an average magnetization produced by the environment. The special site, labeled by o, is governed by the following effective Hamiltonian:

$$H_{eff} = -h_{eff} S_o \tag{2.13}$$

where

$$h_{eff} = h + zJm \tag{2.14}$$

In Eq. (2.14) the magnetization at each site has been introduced: $m = \langle S_i \rangle$. z is the number of nearest-neighbors (coordination number). The local observable m can be calculated through the effective Hamiltonian, giving the well-known Curie-Weiss *self-consistency* equation:

$$m = \tanh\left(\beta h + z\beta J m\right) \tag{2.15}$$

where β is the inverse temperature.

The DMFT extends the standard mean field theory to quantum cases following conceptually the same steps and it constitutes the exact approach for quantum models in the limit of infinite dimensions $d \to \infty$, or, equivalently, for $z \to \infty$. The local effective theory is described through a single-site effective action $S_{eff}[c^\dagger_{o\sigma}, c_{o\sigma}]$, derived by taking the action S of the starting lattice problem and tracing out all the fermionic operators but those of a special site o:

$$\frac{1}{Z_{eff}} \mathrm{e}^{-S_{eff}[c^\dagger_{o\sigma}, c_{o\sigma}]} \equiv \frac{1}{Z} \int \prod_{i \neq o, \sigma} D c^\dagger_{i\sigma} D c_{i\sigma} \mathrm{e}^{-S} \tag{2.16}$$

In the case of the Hubbard model, S_{eff} takes the form:

$$S_{eff} = -\int_0^\beta d\tau \int_0^\beta d\tau' \sum_\sigma c^\dagger_{o\sigma}(\tau) \mathcal{G}_0^{-1}(\tau - \tau') c_{o\sigma}(\tau') + U \int_0^\beta d\tau n_{o\uparrow}(\tau) n_{o\downarrow}(\tau). \tag{2.17}$$

where the effect of the environment of the special site is described by the imaginary-time dependent Weiss field $\mathcal{G}_0(\tau - \tau')$. It has to be stressed, however, that the validity of Eq. (2.17) relies on the assumption of working in $d \to \infty$, since in the case of finite dimension the integration (2.16) would unavoidably determine the appearance of non-Gaussian terms in S_{eff}. $\mathcal{G}_0^{-1}(\tau - \tau')$ can be physically interpreted as the amplitude of probability that a fermion coming from the electronic bath and moving at the time τ on the chosen site o is moving back to the bath at the time τ': this explains the (imaginary) time dependence of the $\mathcal{G}_0^{-1}(\tau - \tau')$.

Like in standard mean field, the single-site effective problem of DMFT is subjected to a self-consistency equation relating the local observable to the effective action. If a Bethe lattice with semicircular density of states and semi-bandwidth D

$$N(\epsilon) = \frac{2}{\pi D} \sqrt{1 - \left(\frac{\epsilon}{D}\right)^2} \tag{2.18}$$

is used, the self-consistency relation takes the form [47]

$$\mathcal{G}_0^{-1}(i\omega_n) = i\omega_n + \mu - \frac{D^2}{4} G(i\omega_n) \tag{2.19}$$

where ω_n are Matsubara frequencies, μ is the chemical potential and $G(i\omega_n)$ is the Fourier transform of the local Green function

$$G(\tau - \tau') = -\left\langle T c_o(\tau) c_o^\dagger(\tau') \right\rangle_{S_{eff}} \tag{2.20}$$

The self-consistency equation (2.19) is a functional relation and gives clearly a richer description with respect of the classical mean field theory. In fact, in DMFT the non-local spatial correlations are treated at mean field level, but the quantum dynamics of the problem is fully taken into account [79]. Moreover, DMFT represents a non-perturbative method which does not assume any particular limit for the strength of the interaction. For this reasons is an ideal tool in the study of non-perturbative phenomena, like the Mott transition.

In practice, the solution of the interacting lattice model is obtained through an iterative procedure: after having obtained a local Green function solving the local problem, a new Weiss field can be found through the self-consistency equation (2.19). The new $\mathcal{G}_0$ is plugged into the impurity action and another $G(i\omega_n)$ is extracted, until convergence is reached.

The difficult step is the solution of the impurity model and the calculation of the Green function $G(i\omega_n)$. This must be done with the help of numerical techniques which we will describe later on in this chapter.

Before concluding this brief description of the ideas at the basis of DMFT, we would like to recall other properties of DMFT, useful for our study and which we will use in the following chapters. The first of these is the possibility of calculating also **k**-dependent quantities. For instance, $G(\mathbf{k}, i\omega_n)$ reads

$$G(\mathbf{k}, i\omega_n) = \frac{1}{i\omega_n + \mu - \epsilon_{\mathbf{k}} - \Sigma(i\omega_n)} \tag{2.21}$$

where the **k**-dependence enters through the band-dispersion $\epsilon_{\mathbf{k}}$ only, while the self-energy, given by

$$\Sigma(i\omega_n) = \mathcal{G}_0^{-1}(i\omega_n) - G^{-1}(i\omega_n) \tag{2.22}$$

is purely local [79]. The local Green function (2.20) in Matsubara frequencies can be written as

$$G(i\omega_n) = \sum_{\mathbf{k}} G(\mathbf{k}, i\omega_n) = \int d\epsilon \frac{N(\epsilon)}{i\omega_n + \mu - \epsilon - \Sigma(i\omega_n)} \tag{2.23}$$

where the sum over **k** can be written as an integral over the density of states.

Through the local Green function, we will characterize the solutions in the various regions of the phase diagram of our Hubbard-Holstein model and we will extract their spectral properties. The local spectral function can, in fact, be evaluated as

$$\rho(\omega) = -\frac{1}{\pi} \sum_{\mathbf{k}} \mathrm{Im} G(\mathbf{k}, \omega + i0^+) \tag{2.24}$$

In this expression, the sum over **k** can be expressed again in terms of an integral over the energies, to give

$$\rho(\omega) = -\frac{1}{\pi} \mathrm{Im} \int d\epsilon \frac{N(\epsilon)}{\omega + \mu - \epsilon - \Sigma(\omega + i0^+)} \tag{2.25}$$

In the following subsections we describe three of the most successful applications of the DMFT: the Mott transition in the half-filled Hubbard model, the density-driven metal-insulator transition in the same model and the bipolaronic transition in the Holstein model. This will be useful to describe, in chapter 3 and 4, the results obtained for the Hubbard-Holstein model.

2.2.1 The metal-insulator transition in the Hubbard model

As we have discussed in the previous section, the Mott transition is an intrinsically non-perturbative problem. The models which are thought to display this kind of phenomenon, can be studied perturbatively only in the weak and strong coupling regimes, correctly describing the two limiting phases but without saying much about the way the transition takes place in the intermediate regime. In recent years DMFT has been successfully applied to the study of the Hubbard model, showing that a quasiparticle peak exists at low energy and shrinks with the strength of the interaction, surviving up to the critical value for the transition. The weight of the peak is given by the quasiparticle residue Z, which, because of the momentum independence of the self-energy in DMFT, is inversely proportional to the quasiparticle effective mass:

$$\frac{m^*}{m} = \frac{1}{Z} = 1 - \frac{\partial}{\partial \omega} \mathrm{Re}\Sigma(\omega) \bigg|_{\omega=0} \tag{2.26}$$

At the same time high energy incoherent bands develop and absorb the spectral weight lost by the low-energy coherent peak [47]. This can be seen in Fig. 2.2, where we show the spectral function of the Hubbard model at half-filling, calculated with DMFT. The values of U/D increases going from the top to the bottom. In the lowest panel we can see the spectral density of the Mott insulator, in which two bands of width given approx. by $W = 2D$ are centered at $\pm U/2$.

The point where the Z goes to zero and no metallic solutions can be found for larger values of U, is defined as U_{c2}, while, starting from the insulating phase and lowering U, a point is reached where the gap closes and no more insulating solutions exist. This point is called U_{c1}. Since U_{c1} is smaller than U_{c2}, both a metallic and an insulating solution can be found for $U_{c1} < U < U_{c2}$. In the third and fourth panels from the top of Fig. 2.2, U is between $U_{c1} \simeq 2.5D$ and $U_{c2} \simeq 3D$, and the solutions reported are the metallic ones.

It turns out that the metallic phase has the lowest energy in this coexistence region implying that, at zero temperature, the metal-insulator transition takes place at U_{c2}, i.e.

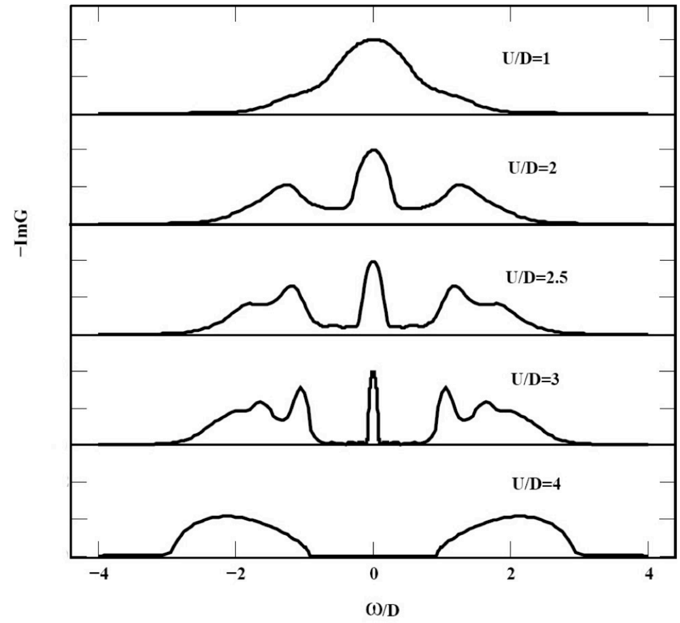

Figure 2.2: Evolution with U of the spectral density in the half-filled Hubbard model. Taken from Ref. [47].

where the metallic peak disappears. Moreover, the Mott transition, at zero temperature, is of second order and it is characterized by a vanishing charge compressibility.

Both U_{c1} and U_{c2} decrease with increasing temperature as it can be seen in Fig. 2.3, where the phase diagram of the Hubbard model calculated with DMFT is reported [80, 81, 82]. The two curves merge at a temperature around 1/50 of the bandwidth W, in a critical point where the metal-insulator transition is, like in the zero temperature case, of second order. Below the critical temperature, the transition is characterized by hysteresis and it is of first order, while above the critical temperature a crossover between a metallic-like and an insulating-like solution is found.

The Hubbard model has been investigated with DMFT also for finite values of the doping level $\delta = 1 - n$. The outcome of the analysis is that a density-driven metal-insulator transition exists for any values of $U > U_{c2}$ [84]. In fact, the metallic phase does not exist at half-filling if u is large, but it can be found for arbitrary large Coulomb repulsion provided that the density is different from 1. The insulating phase instead, exists, within the Hubbard model, only for $n = 1$. Naively, the reason why the Hubbard model is always metallic out of half-filling, is that the presence of empty sites makes electronic

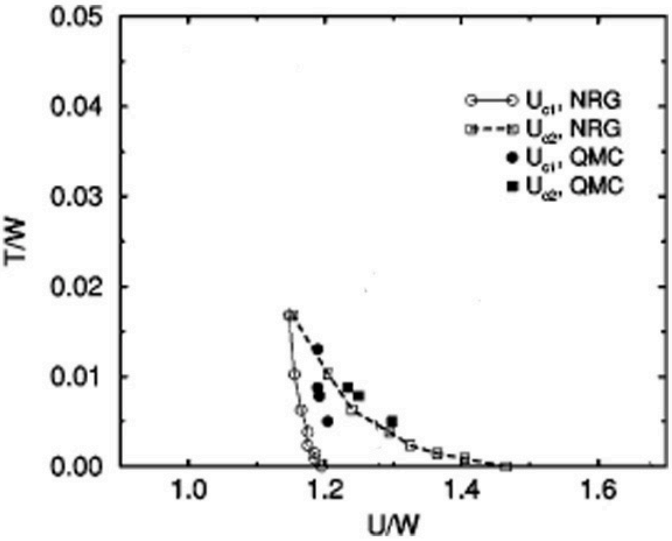

Figure 2.3: U_{c1} and U_{c2} as a function of the temperature, calculated with two different techniques: Numerical Renormalization Group (NRG) and Quantum Monte Carlo (QMC). From Ref. [80].

motion always possible with a reduced cost in terms of double occupancies. In fact, going towards half-filling by tuning the chemical potential μ, one finds the metal as long as $n \neq 1$, and this joins onto the insulator at $n = 1$ with a finite slope in the n-μ curve, i.e., it has a finite charge compressibility $\kappa = \partial n/\partial\mu$ [84, 83]. In the insulating phase a further increase of the chemical potential μ has no effect on the density n, which remains equal to 1 as long as μ lays inside the gap in the spectral density. The Mott insulator is in fact incompressible, i.e. $\kappa = 0$.

In Fig. 2.4 the phase diagram of the Hubbard model is reported, as a function of $\Delta\mu$ (deviation from the chemical potential at half-filling, which is equal to $U/2$) and the interaction U, as calculated within DMFT at zero temperature [83]. The entire insulating region is characterized by $n = 1$, while, in the metallic one, as soon as one leaves the $\Delta\mu = 0$ line, the density departs from 1. As in the case of the Mott transition at half-filling, the density-driven one is accompanied by a region of coexistence of DMFT solutions [85, 86] delimited by two curves of chemical potential, $\mu_{c1}(U)$ and $\mu_{c2}(U)$ (see Fig. 2.4). Of course, the stable solution is the one that minimizes the grand-canonical free energy. At $T = 0$ the metal is stable in the whole coexistence region. This means that the chemical

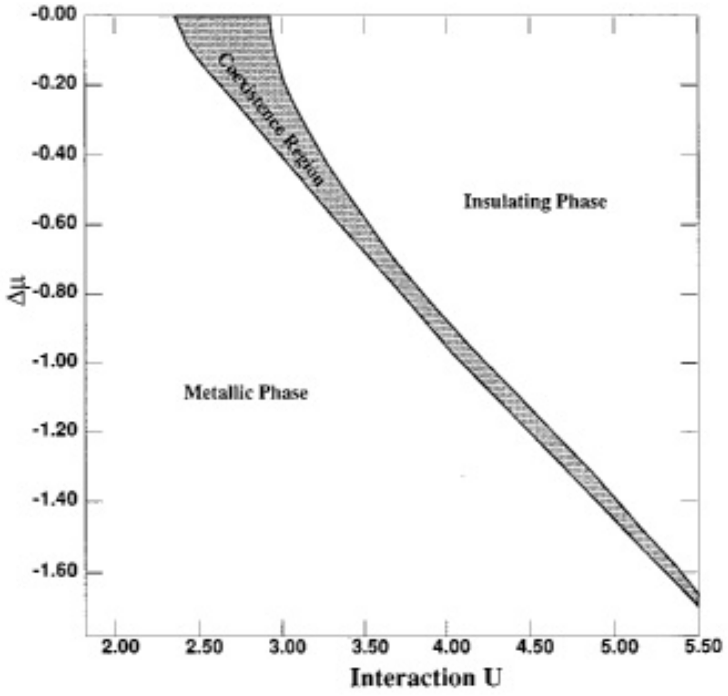

Figure 2.4: Chemical potential $\Delta\mu$ vs. U phase diagram at $T = 0$ from Ref. [83]. $\Delta\mu$ is the deviation from the chemical potential at half-filling. The metallic phase has $n < 1$, while the insulating one, $n = 1$. The coexistence region is characterized by the presence of two DMFT solutions, with the metallic being always the stable one.

potential where the transition takes place is equal to μ_{c2}, for every value of U.

2.2.2 Bipolaronic transition in the Holstein model

In Sec.2.1.2 we have described the most important properties of the electron-phonon interaction. We have seen that, by increasing the electron-phonon coupling, the system enters a strong-coupling polaronic regime characterized by the presence of local lattice distortions. This crossover is strongly influenced by the value of the phonon frequency ω_0: for small $\gamma = \omega_0/D$, λ_{pol} is of order 1, while for large γ, $\lambda_{pol} \propto \omega_0/D$. In the antiadiabatic limit, i.e. for $\omega_0 \to \infty$, no polaronic distortion can be induced, in fact, for any finite value of the electron-phonon coupling λ, since $\lambda_{pol} \to \infty$.

In the polaronic regime, the system is characterized by low-energy excitations which, although strongly renormalized, are still coherent. The weight of the peak at the Fermi level goes to zero only when the localizing power of the electron-phonon interaction is able to form incoherent pairs of polarons with opposite spin (bipolarons). One has in mind that this latter phenomenon should be mostly related to the energetic balance between kinetic energy and the (phonon-mediated) attractive interaction and, for this reason, it should be less sensible to the value of the phonon frequency ω_0. We can understand this better, by taking, for a moment, the antiadiabatic limit, in which the Holstein model maps onto an attractive Hubbard model with $u = \lambda$: It is known that the attractive Hubbard model undergoes a transition to a pair phase by increasing the value of the electron-electron attraction. The metal is characterized by a narrow resonance at the Fermi level which shrinks approaching the transition, but, in contrast with the repulsive Hubbard model, the localized state is characterized by the presence of pairs of electrons with opposite spins and single-occupied sites are almost absent [87]. In the correspondent antiadiabatic Holstein model, therefore, there must be a transition to the same incoherent pair phase for finite values of λ, despite the infinitely large value of the phonon frequency. In the meantime, the polaronic crossover has been shifted for infinitely large values of the coupling.

This rises the following interesting question: What is actually the relation between the bipolaronic transition and the polaron crossover, and what happens away from the peculiar antiadiabatic limit, i.e. when also polaronic distortions can be induced for a finite λ? We know, in fact, that λ_{pol} decreases as γ decreases and reaches a value of order 1 in the opposite adiabatic limit. To understand the behavior of the bipolaronic transition as a function of γ, one needs to look at the value of λ for which the quasiparticle weight Z

goes to zero.

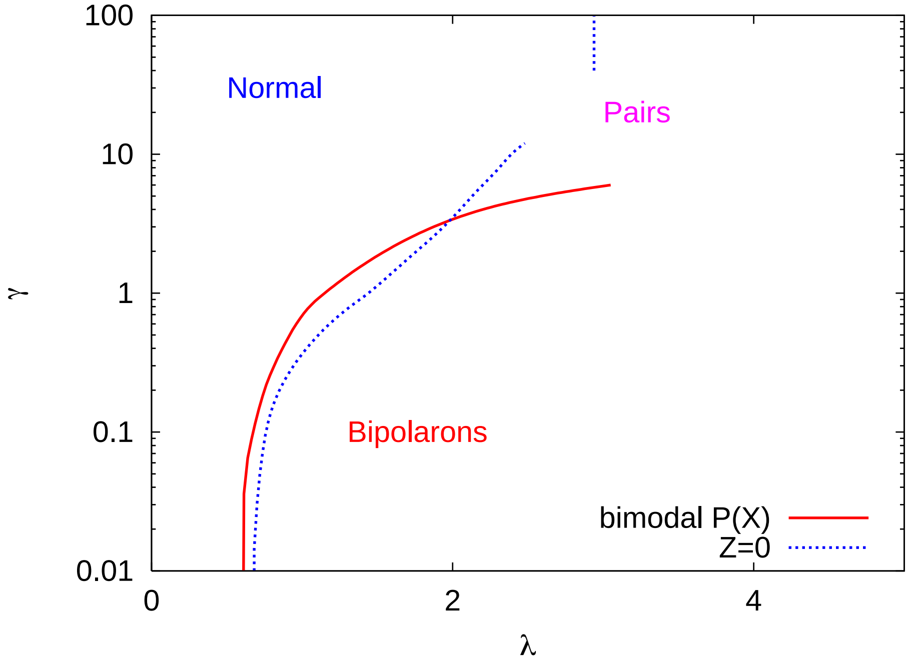

Figure 2.5: Phase diagram of the Holstein model at zero temperature from Ref. [3]. The electron-phonon coupling λ is on the x-axis and the adiabatic parameter γ on the y-axis.

This has been the object of DMFT investigations on the Holstein model, in the adiabatic limit [88] as well as, more recently, for finite ω_0 [67, 3]. In the work by Capone and Ciuchi [3] it has been shown that in the region of most physical interest, i.e. for moderate values of γ, upon increasing λ, a bipolaronic transition, distinct from the polaronic crossover, is reached for slightly larger values: $\lambda_{pair} > \lambda_{pol}$ (see the low part of Fig. 2.5). In fact, when the probability distribution function for the phonon field develops the bimodal shape (see Sec. 2.1.2), the quasiparticle weight Z is still finite (solid red line in Fig. 2.5). The low energy peak of this metallic solution in the presence of lattice polarization, shrinks with increasing λ in a small window, before the system reaches the bipolaronic transition for which Z vanishes (dotted blue line in Fig. 2.5).

The previously sketched picture emerges therefore from a direct calculation: Under the effect of an increasing λ, polarons are formed within the metallic phase; a further increase of the electron-phonon coupling enhances the attraction between polarons of opposite spin and eventually pairs of bipolarons are formed and the transition to the incoherent pairing phase is obtained. In Fig. 2.5 the zero-temperature DMFT results from Ref. [3], are shown also for large values of γ. In the antiadiabatic regime, the sequence obtained for small γ (polaronic crossover followed, quite immediately, by the bipolaronic transition) is reverted, as expected. In fact, it is found that, by increasing λ, polaronic distortions develop only after the quasiparticle weight has gone to zero. The transition to the incoherent pair phase is therefore not associated to lattice polarization. In Fig. 2.5, as a consequence, the dotted blue line where Z goes to zero and the red line where $P(X)$ becomes bimodal, cross each other for γ between 2 and 3.

2.3 Methods of solutions

We have seen in Sec. 2.2, that DMFT describes a quantum interacting problem in terms of a single-site theory subjected to a self-consistency condition which preserves the quantum many-body nature of the original model. As a consequence, the calculation of the local observable, i.e. the Green function $G(i\omega_n)$, is not straightforward, as in classical mean field approaches, and one needs to solve the single impurity action by means of numerical methods. Several techniques have been used for this purpose: Exact Diagonalization (ED), Quantum Monte Carlo (QMC), Wilson's Numerical Renormalization Group (NRG), and others.

In this section we briefly describe ED and QMC, which are the two methods used in this work. In fact, the zero-temperature results of Chapter 3 and 4 on the Hubbard-Holstein model have been derived using ED, while for the Holstein model at finite temperature, studied in Chapter 5, we have worked with QMC.

2.3.1 Zero temperature: Exact Diagonalization

An Hamiltonian description of the local action S_{eff} is introduced in the Exact Diagonalization approach. For this purpose, the single impurity Anderson model can be used, in which the degrees of freedom of the bath, are represented by fictitious auxiliary fermions $b_{i\sigma}$ and $b^\dagger_{i\sigma}$. An hybridization term couples the fermions of the bath to the impurity, described by f_σ and $f^\dagger_\sigma$.

In the case of the Hubbard-Holstein model we have an Anderson impurity with a local phonon on the impurity site [89]. Its Hamiltonian reads

$$H_{AM} = \sum_{k\sigma} \tilde{\epsilon}_k b^\dagger_{k\sigma} b_{k\sigma} - \mu n + \sum_{k\sigma} V_k \left(b^\dagger_{k\sigma} f_\sigma + f^\dagger_\sigma b_{k\sigma} \right) + U n_\uparrow n_\downarrow - g(a + a^\dagger) n + \omega_0 a^\dagger a \quad (2.27)$$

where $\tilde{\epsilon}_k$ and V_k are the energies and the hybridization parameters, n_σ is equal to $f^\dagger_\sigma f_\sigma$, $n = n_\uparrow + n_\downarrow$ and $a^\dagger$ and a are the creation and destruction operators of the local phonons. Since the fermions of the bath are described by quadratic terms, the non-interacting Green function of the impurity problem $\mathcal{G}_0(i\omega_n)$ can be easily expressed in terms of $\tilde{\epsilon}_k$ and V_k:

$$\mathcal{G}_0^{-1}(i\omega_n) = i\omega_n + \mu - \sum_k \frac{V_k^2}{i\omega_n - \tilde{\epsilon}_k} \tag{2.28}$$

In the ED method, the sum over k of Eq. (2.28), is restricted to a finite and small number of levels $N_s - 1$. The Anderson impurity Hamiltonian is first of all discretized and then exactly diagonalized [90]. Let us stress that the truncation does not mean that we are considering a finite small number of sites, since the DMFT equations are defined in the thermodynamic limit.

At zero temperature, the discretized model is solved using the Lanczos method, which allows to compute the Green's function at $T = 0$, through a continued-fraction expansion. Once the Green function G is extracted, a new Weiss field $\mathcal{G}_0$ is obtained from the self-consistency equation (2.19). The study of the Hubbard-Holstein model, from this point of view, does not introduce additional difficulties with respect to the pure Hubbard model, since the self-consistency condition does not involves the phononic degrees of freedom. This is due to the dispersionless spectrum of the Holstein phonons; should one consider non-local phonons, a second self-consistence equation would be needed [91].

In order to obtain the new parameters for the Anderson Hamiltonian and calculate a new Green function, a projection of the Weiss field $\mathcal{G}_0$ onto the finite-N_s subspace is needed. The steps of the entire procedure are sketched in Fig. 2.6.

The method converges rapidly as a function of N_s, and just a few levels are enough to achieve convergence. Most of the results presented in this work are extracted for $N_s = 10$, a sufficiently large number of levels to obtain full converged and reliable results. The phonon Hilbert space has also been truncated by allowing for a finite number of phonons and checking for convergence as a function of this number. When necessary, we considered up to 50 phonons.

With this method one can calculate the expectation value over the ground state of many quantities. For example, the probability distribution function of the phonon field X, that we have introduced in Sec. 2.1.2, can be calculated as

$$P(X) = \langle \psi_0 | X \rangle \langle X | \psi_0 \rangle \tag{2.29}$$

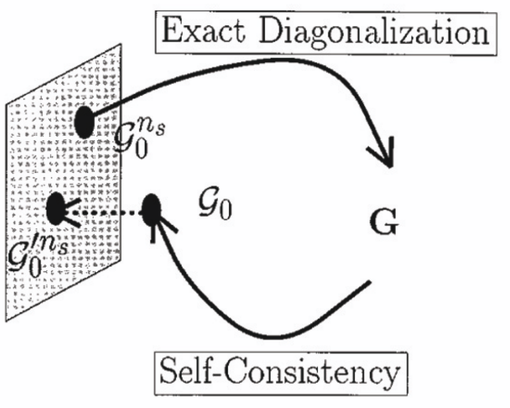

Figure 2.6: Schematic procedure for the projection of the Green function onto the finite-N_s subspace. At self-consistency $\mathcal{G}_0^{N_s} = \mathcal{G}'^{N_s}_0$.

where ψ_0 is the ground state of the system, as determined by the Lanczos method at zero temperature.

One of the biggest advantages of ED is the possibility of performing directly the analytic continuation on the real axis. From the Green's function, the spectral function $\rho(\omega)$, defined in Eq. (2.25), can be obtained. For this purpose, the self-energy must be analytically continued on the real axis. This can be done using the expression for the Weiss field in terms of the Anderson parameters:

$$\Sigma(i\omega_n) = \mathcal{G}_0^{-1}(i\omega_n) - G^{-1}(i\omega_n) = i\omega_n + \mu - \sum_k \frac{V_k^2}{i\omega_n - \tilde{\epsilon}_k} - G^{-1}(i\omega_n) \tag{2.30}$$

The two terms of Eq. (2.30) which contain explicitly the Matsubara frequency are continued on the real axis by directly replacing $i\omega_n$ by $\omega + i0^+$. The same can be done in the ED and Lanczos expression for the Green function which is an explicit function of the frequency, written in terms of the energy levels of the discretized spectrum.

As we have said, the fit of the Green function is done with a basis set which lives on the finite-N_s subspace and this implies that the densities of states that we extract numerically have some spurious dips. In particular, each of the Hubbard bands usually appears as made of two or three main structures (see Fig. 3.2). Nevertheless this does not constitute a problem when we have to compare the densities of states of two different solutions, like in Fig. 3.10, and it is even of some help to resolve the extra satellites of the solution coupled to phonons.

Before concluding this section about the general properties of the ED method, we would like to make some technical comments about determination of a zero quasiparticle weight, in the study of the Mott transition, as well as the bipolaronic transition driven by the electron-phonon coupling. Both phenomena are, in fact, characterized, at zero temperature, by the vanishing of the quasiparticle residue Z, defined in Eq. (2.26). The ED method introduces an intrinsic cut off $1/\tilde{\beta}$, associated to the Matsubara formulation, which truncates all the frequency summations. We keep this fictitious temperature as low as possible, but this can manifest itself through a saturation of a physical quantity, like Z, which is vanishing small in the vicinity of the Mott transition.

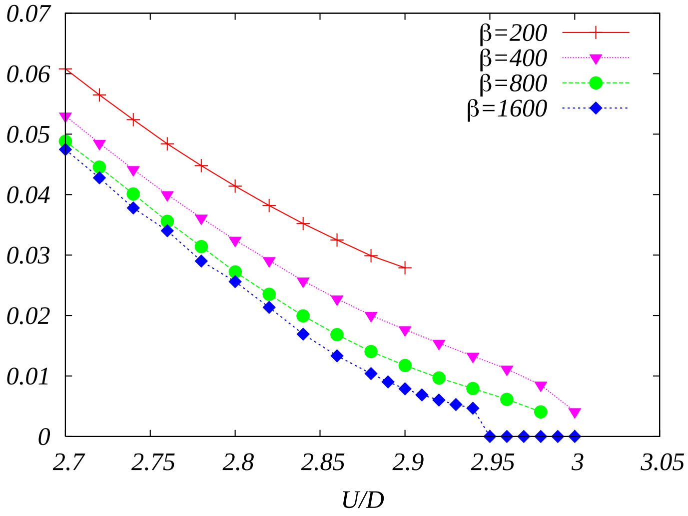

Figure 2.7: Curves of Z, calculated for different values of $\tilde{\beta}$, in the pure Hubbard case. For the smallest value of the cutoff ($\tilde{\beta} = 1600$) we show also the points (blue diamonds) lying on the horizontal axis, which correspond to insulating solutions, to evidence the jump that is obtained even for this small value of the cut off, close to the critical U. For smaller $\tilde{\beta}$ we have reported only metallic converged runs.

The typical situation is depicted in Fig. 2.7, where Z is shown as a function of u, for $\lambda = 0$ and different values of the cut off $\tilde{\beta}$. It is clear that the region of saturation is smaller, the larger is $\tilde{\beta}$. Performing a linear fit of these curves, one gets a value for the critical U which scales with $\tilde{\beta}$ as reported in Fig. 2.8. This analysis shows how the $\tilde{\beta} = 1600$ curve gives a value which is very close to the $\tilde{\beta} = \infty$ extrapolation, and, since we find the same kind of scaling for $\lambda \neq 0$, we have used the linear fit to the $\tilde{\beta} = 1600$ curve to determine U_{c2} through the whole range of λ. In other words, this has been the

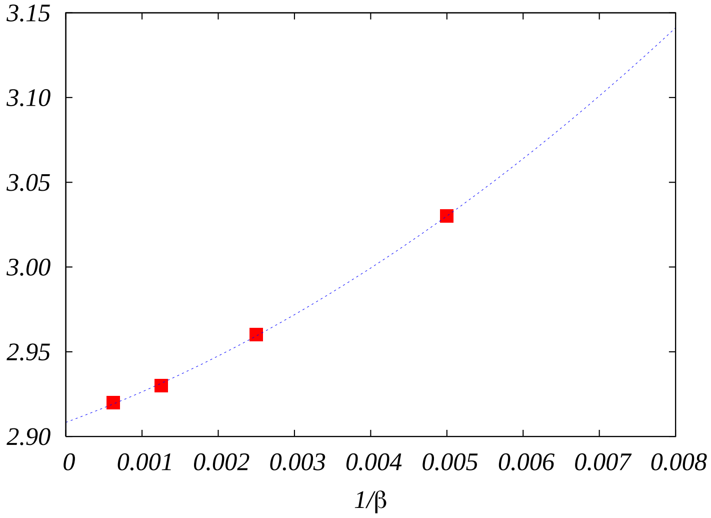

Figure 2.8: $\tilde{\beta}$ scaling to determine U_{c2}, in the pure Hubbard case.

criterion used to draw the red curve in Fig. 3.1.

2.3.2 Finite temperature: Quantum Monte Carlo

In the QMC method implemented for DMFT, the single-site effective action is directly solved through a Monte Carlo simulation. The most successful QMC algorithm is the one due to Hirsch and Fye [77], which has been formulated for the study of the Anderson impurity model. In the action (2.17), the imaginary time interval $[0, \beta]$ is divided into a finite number L of slices of width $\Delta\tau$, with $\beta = L\Delta\tau$. The interaction term is decoupled by means of a discrete Hubbard-Stratonovich transformation which introduces auxiliary Ising spins, which are then sampled with Monte Carlo. The Hirsch-Fye is a very efficient method and it does not suffer from the negative sign problem which in many cases affects Monte Carlo simulations. It has been extensively used in DMFT studies of the Hubbard model at finite temperature [47].

As we have noted for the case of ED, QMC methods used as DMFT impurity solvers are not affected by finite lattice size effects, because the DMFT approach implicitly assumes the thermodynamic limit. Moreover, in contrast with ED, the Hamiltonian description of the impurity model is not introduced in QMC, and the method does not suffer from the exponential growth of the Hilbert space. Its main drawback, instead, is the difficulty in obtaining reliable results for very small temperatures. For too large values of β, in fact, one would have to increase the number L of imaginary time intervals out of the computation possibilities.

For the Anderson-Holstein action, needed in our case, one has to perform a Monte Carlo sampling also on the phonon fields, which, contrary to the Ising spins, are continuous fields and have an infinite range of variability. This can be done by means of the Blankenbecler-Scalapino-Sugar approach [76], which has been introduced for the study of coupled electron-phonon systems in finite dimension. The effective action obtained in DMFT for the Holstein model[3] is made of three terms [92]:

$$S_{el} = \int_0^\beta d\tau \int_0^\beta d\tau' \sum_\sigma c^\dagger_\sigma(\tau)\mathcal{G}_0^{-1}(\tau-\tau')c_\sigma(\tau') \tag{2.31}$$

$$S_{ph} = \int_0^\beta d\tau \left(\frac{1}{2}M\dot{x}^2(\tau) + \frac{1}{2}M\omega_0^2 x^2(\tau)\right) \tag{2.32}$$

$$S_{el-ph} = -g' \int_0^\beta d\tau x(\tau)n(\tau) \tag{2.33}$$

where $n(\tau) = \sum_\sigma c^\dagger_\sigma(\tau)c_\sigma(\tau)$ and M is the mass of the oscillator. g' is the coupling constant already defined in Sec.2.1.2.

The imaginary-time slices are introduced, and the fermions are integrated out analytically. The result of the integration is a fermionic determinant which depends parametrically on the L values of the phonon field along the imaginary-time path $\{x(\tau_i)\}_{i=1,\dots,L}$. The Monte Carlo sampling of the pure-bosonic resulting action, therefore is carried out with a statistical weight of the form

$$\det G^{-1}\left[\{x(\tau_i)\}_{i=1,\dots,L}\right] \mathrm{e}^{-S_{ph}\left[\{x(\tau_i)\}_{i=1,\dots,L}\right]} \tag{2.34}$$

This method works well in the range of temperatures we are interested in for our study (i.e. not too low temperatures) and naturally yields the quantities we want to focus on, namely, electronic and bosonic correlation functions, as well as the probability distributions associated to the phonon fields. The Blankenbecler-Scalapino-Sugar method is not affected by the negative sign-problem, exactly like in the Hirsch and Fye approach, while its main limitation comes from the adiabatic regime ($\omega_0/D \ll 1$) where simulations becomes hard to perform. For the results of Chapter 5, for instance, a number of 32 slices has been sufficient in most cases, except for the lowest temperature ($\beta = 8$) for which

---

[3] Here we limit to the discussion of the pure Holstein model with QMC in DMFT. The finite temperature analysis of this work (Chapt. 5), in fact, is carried out for $U = 0$.

we have used $L = 64$, in order to keep $\Delta\tau$ small. This controls the error due to the discretization of the imaginary time which is proportional to $(\Delta\tau)^2$, while the statistical error that comes from the random sampling is reduced by dividing measurements into several bins and it is evaluated as the variance among the bins.

Chapter 3

Metal-insulator transitions at half-filling

3.1 Phase diagram

The Hubbard-Holstein model is expected to display a rich and complicated phase diagram controlled, as already discussed in the previous chapters, by many different parameters. We want to recall them:

- $u = \frac{U}{D}$ - degree of correlation (ratio of the Hubbard repulsion to the semi-bandwidth)
- $\gamma = \frac{\omega_0}{D}$ - adiabatic parameter (ratio of the phonon frequency to the semi-bandwidth)
- $\lambda = \frac{2g^2}{\omega_0 D}$ - electron-phonon coupling (ratio of the bipolaronic binding energy to the semi-bandwidth)
- $\alpha = \frac{g}{\omega_0}$ - parameter associated to the lattice displacement (ratio of the coupling constant g to the semi-bandwidth)

In this section we first determine the phase diagram at half-filling focusing on the zero-temperature normal phases of the model. This study is still rich even in the absence of broken-symmetry phases and presents two opposite points of view: The first one takes the strongly correlated physics of the Hubbard model as a starting point and analyzes the modifications induced by an electron-phonon interaction. The second starts from the physics of the Holstein model and switch on the Coulomb repulsion U to see its influence on the metallic properties and on polaron formation.

As we have said in Sec.2.2, the Hubbard-Holstein has been the object of DMFT studies [93] which focused on the charge-density wave and superconducting instabilities for different values of the density. More recently, two groups calculated the phase diagram of the Hubbard-Holstein at half-filling in the normal phase [94, 95]. In the present work, adopting the same approach, we study in more detail the region close to the metal-insulator transition at half-filling and out of half-filling. We have seen, in the previous chapter, how DMFT, due to its non-perturbative nature, is able to describe on equal footing, both the "electronic side" ($u \gg \lambda$) and the "phononic side" ($\lambda \gg u$). For this reason we expect it also to give a correct description of the intermediate regime ($u \sim \lambda$) and to give reliable answers to our questions about the correlation-driven and the density-driven Mott transition in the presence of an electron-phonon coupling.

In the following two subsections we discuss the different regions of the phase diagram at half-filling, shown in Fig. 3.1. Our results are obtained using the ED technique to solve the impurity model at zero temperature.

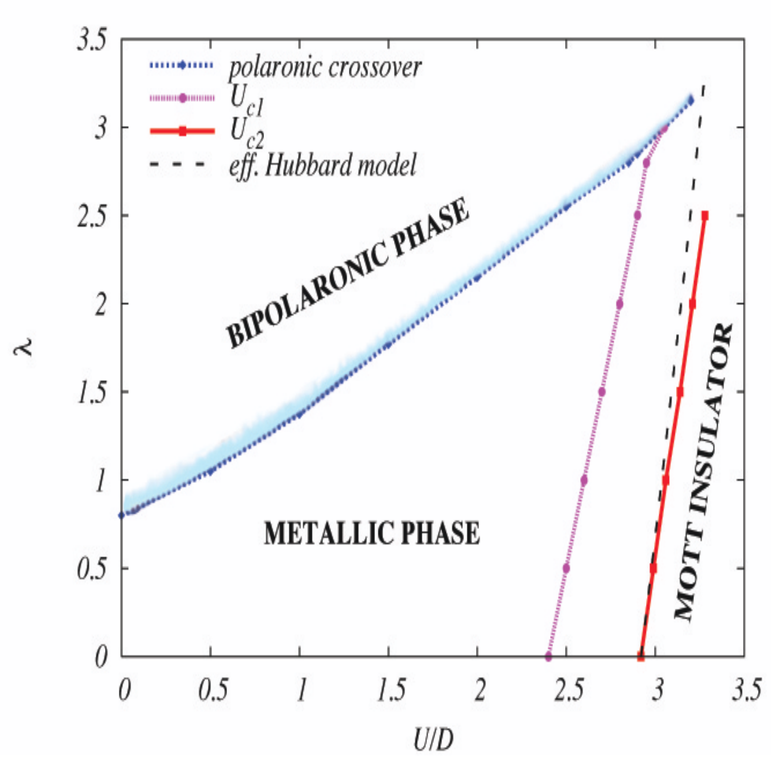

Figure 3.1: Phase diagram of the Hubbard-Holstein model for $\omega_0 = 0.2D$ at $T = 0$, calculated with DMFT. The dashed blue line marks the polaron crossover and the light blue shaded area represents a region with no bipolaronic pairs. The dashed line represents the value of U_{c2} predicted by an effective Hubbard model, as discussed in Sec.3.2.

3.1.1 transition to the Mott insulator

In this section we describe how the Mott transition takes place for finite values of the electron-phonon coupling. At fixed small λ, the metal evolves in a similar way as in the pure Hubbard case and exists up to a value $U_{c2}(\lambda)$, denoted in Fig. 3.1 by a red line. For each λ we have determined the value of $U_{c2}(\lambda)$ and this, as it can be seen in the figure, is a slowly increasing function of λ. For $U > U_{c2}(\lambda)$, only the Mott insulating solution is found, but, as in the pure Hubbard case, the latter exists also for $U < U_{c2}(\lambda)$, down to a value of U denoted by $U_{c1}(\lambda)$ (in purple in the figure). Therefore, between $U_{c1}(\lambda)$ and $U_{c2}(\lambda)$, two solutions exist. $U_{c1}(\lambda)$ is roughly parallel to $U_{c2}(\lambda)$, so that the size of the coexistence region is more or less unaffected by the electron-phonon coupling.

The DMFT studies of the Hubbard model have evidenced that the weight of the narrow metallic peak at the Fermi level continuously vanishes at $U = U_{c2}$. For technical reasons, our analysis in the presence of the electron-phonon interaction is not able to distinguish between a second-order and a weakly first-order transition. The behavior of Z for values of U extremely close U_{c2} is, in fact, very difficult to determine accurately due to the presence of intrinsic cutoffs in ED. This reflects in a saturation of Z, observed slightly before the metallic solutions cease to exist, i.e. when U approaches U_{c2} (see Sec.2.3.1 for details about the extrapolation used to determine U_{c2}). In conclusion, by analyzing the behavior of the saturation region for different values of λ, we can conclude that the metal-insulator transition driven by correlation in the presence of the electron-phonon interaction, is still of second-order or, at maximum, becomes weakly of first-order.

In Sec.2.3.1 we have pointed out that one of the main advantages of the impurity model solved with ED is the possibility of obtaining reliable analytic continuations of the spectra on the real axis. It is thus interesting to follow the evolution of the density of states with u, and compare it to the well known pure Hubbard case [47]. As we have described in Sec.2.1.1, in the pure Hubbard model the broad peak at the Fermi level shrinks with increasing u, while the Hubbard bands, centered at $\omega/D \simeq \pm u/2$, develops as U is increased. For larger u one finds the Mott insulating solution, characterized by well formed Hubbard bands and by the absence of spectral weight at low-energy. The transition takes place when the quasiparticle peak disappears. As it can be seen from the phase diagram of Fig. 3.1, a finite λ determines only a small shift of U_{c2} towards larger values. This can be observed in Fig. 3.2, where the density of states for the Hubbard-Holstein model at fixed $\lambda = 1$ and $\omega_0 = 0.2D$ is shown for increasing values of u. In fact,

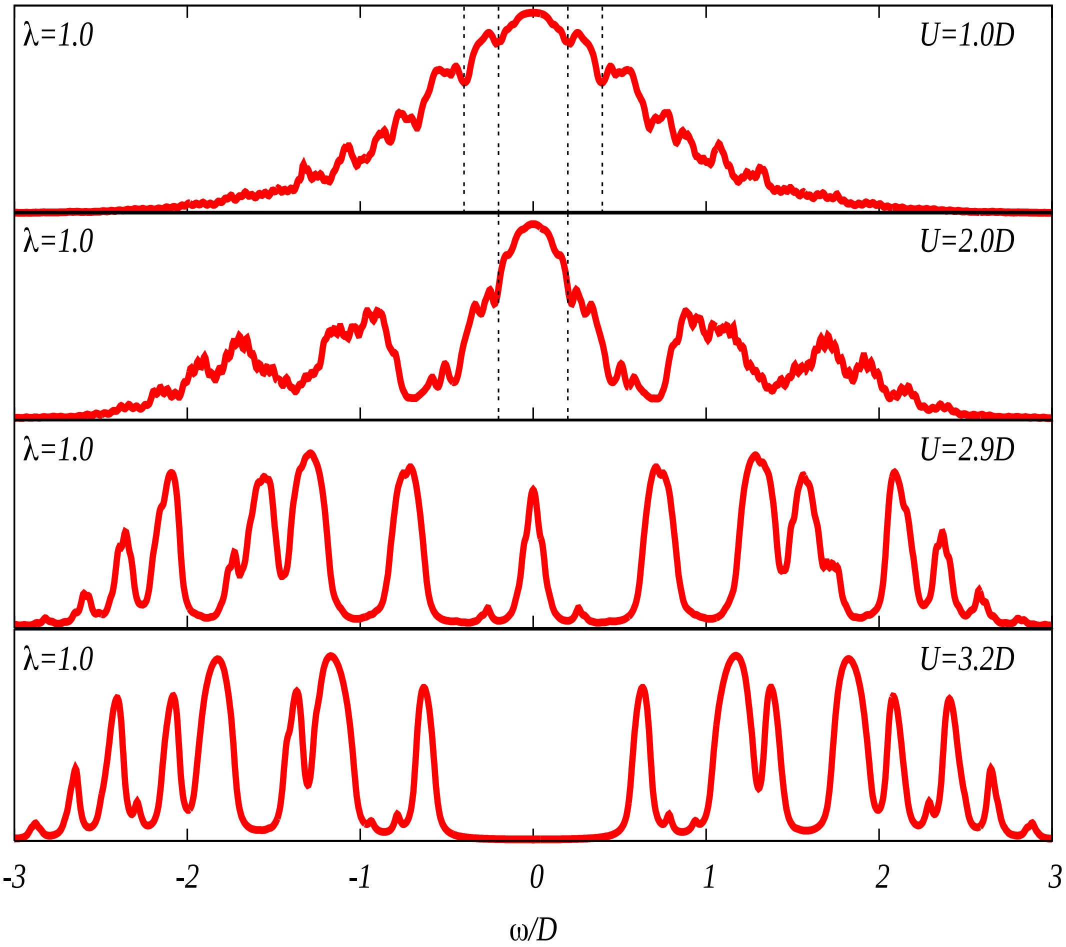

Figure 3.2: Evolution with u of the density of the states for the Hubbard-Holstein at fixed $\lambda = 1$ and $\gamma = 0.2$. The central peak shrinks with increasing u, as it happens in the pure Hubbard case, and, for larger u, only the Mott insulating solution is found.

the values of u for which the metallic solution disappears are not significantly different from those of the pure Hubbard model and a similar picture holds also in this case (the case for $\lambda = 0$ has been shown in Fig. 2.2). Nevertheless the density of states in the weakly correlated metallic phase is visibly influenced by the electron-phonon interaction, which introduces the dips with a periodic spacing of ω_0, one of the typical features of a coupled electron-phonon system [63, 59]. The dips are symmetrically placed around the Fermi level and occurs for $\omega = (\pm 1, \pm 2 \cdots)\omega_0$, as evidenced by the corresponding vertical dashed lines.

3.1.2 polaron and bipolaron formation

In this section we leave the "electronic side" of the phase-diagram and discuss the behavior of the system as a function of the electron-phonon coupling at fixed Hubbard repulsion. With increasing λ, one first reaches the polaron crossover, for all the values of U considered here (blue dotted line in Fig. 3.1). When $U < U_{c2}(\lambda)$, this is followed, quite immediately for this value of the phonon frequency $\omega_0 = 0.2D$, by the transition to the bipolaronic phase characterized by the presence of incoherent pairs of polarons with opposite spin. As we have said, the critical value for the bipolaronic transition has been calculated, for $U = 0$, in Ref. [3] (see Sec.2.2.2). In Fig. 3.1 we have indicated, also for $U \neq 0$, the small region between the polaronic crossover and the bipolaronic transition, with the light blue shaded area.

We have discussed polaron formation within the Holstein model in Sec.2.1.2 where we have shown the evolution of the probability distribution function of the phonon field with λ (Fig. 2.1). Here we are interested in studying how the polaronic crossover is modified by the inclusion of the Hubbard repulsion. In Figure 3.3 the symmetrized probability distribution function of the field $\Phi = (a + a^\dagger)/\sqrt{2} = X\sqrt{M\omega_0}$ is shown[1] for an intermediate value of the Hubbard repulsion: $U = D$. For $U \lesssim D$ the evolution from the unimodal to the bimodal shape is smooth and continuous, in the same way as it occurs in the pure Holstein case (Fig. 2.1). For larger values of U the crossover is qualitatively different (see Fig. 3.4): increasing λ, in fact, two shoulders appear in the distribution of Φ, in addition to the central peak. A further increase of λ determines a sudden change in the distribution, which becomes bimodal. This can be attributed to the fact that single occupied states (which is associated to $\Phi = 0$) are strongly favored when U is sizable.

---

[1] This rescaling has been introduced also in Sec.2.1.2.

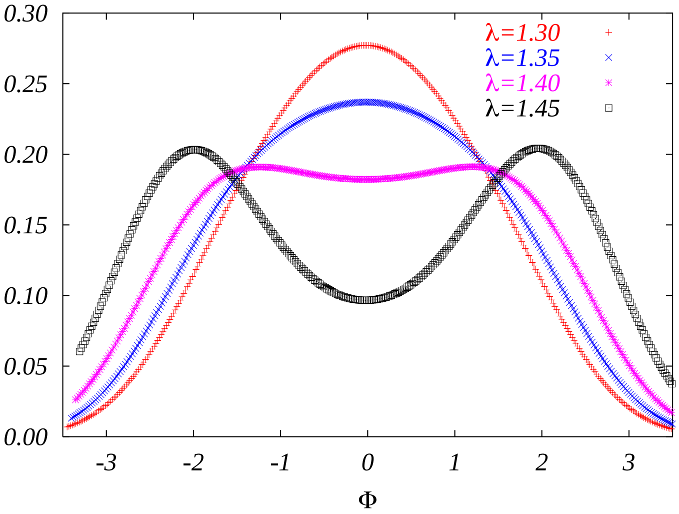

Figure 3.3: Evolution with λ of the phonon displacement distribution $P(\Phi)$ and polaronic crossover for $U = D$ and $\omega_0 = 0.2D$.

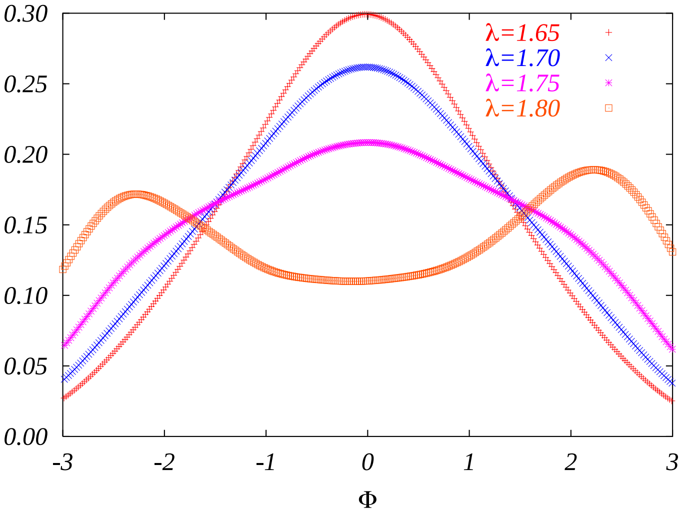

Figure 3.4: Polaron crossover at $U = 1.5D$. $\omega_0 = 0.2D$ at $T = 0$. Differently from the cases with smaller u, two shoulders can be seen for $\lambda = 1.75$, in addition to the central peak. This triple structure is suddenly changed into a bimodal one for stronger coupling.

The situation in which the empty and double-occupied states ($\Phi = \pm\sqrt{2}\alpha$ respectively) have a larger probability than the single-occupied one ($\Phi = 0$) is reached only when the attraction mediated by λ exceeds the total repulsion. This result shows how, for large u, not only the value of λ needed for this balance between attraction and repulsion, is larger (see Fig. 3.1), but also the tendency of avoiding double and empty sites gives a first-order character to the crossover, which is no longer smooth and continuous as in the small-U case.

Before entering the bipolaronic phase characterized by $Z = 0$, a narrow region exists in which polarons are formed but Z, though very small, is different from zero (light blue shaded area in Fig. 3.1). The determination of the exact extension of this region requires a specific analysis which has been carried out only at $U = 0$ by Capone and Ciuchi [3]. The result is that, for small values of γ, bipolarons form for values of λ slightly larger than the polaron crossover. In the presence of the Hubbard repulsion, the situation is quite similar, with the tendency towards a further shrinking of the region with increasing U, as indicated by the light blue shaded area in the figure. The existence, for $U \neq 0$, of a polaronic crossover, followed by the bipolaronic transition, means therefore that the phonon-mediated attraction is able to win over a finite Hubbard repulsion, and, after having polarized the lattice, is also able to form an incoherent pair phase of bipolarons with $Z = 0$.

The situation is different for large ω_0/D (antiadiabatic limit), where the polaron crossover is shifted for $\lambda \gg 1$ and pair formation (still placed for $\lambda \sim 1$) is not of bipolaronic character. In this case, in fact, the localized phase is characterized by the presence of incoherent pairs without lattice distortion since the phonons mediates an interaction which is essentially instantaneous (attractive Hubbard). In Fig. 3.5 we show the expected phase diagram for the Hubbard-Holstein model in the antiadiabatic limit. The two transition lines ($U_{c2}(\lambda)$ and $\lambda_{c2}(U)$) are symmetric with respect to $\lambda = u$. In fact, the Hubbard repulsion is contrasted, in the antiadiabatic limit, by a completely instantaneous attraction and, at half-filling, there is a complete specularity between the transition to the Mott insulator and to the incoherent pair phase. The mapping between the repulsive and the attractive Hubbard models implies, as well, that the value of U_{c2} is equal to λ_{c2} [87]. Away from the antiadiabatic limit, we have found, instead, $\lambda_{c2}(U = 0) < U_{c2}(\lambda = 0)$, as it can be seen in Fig. 3.1. In the case of $\omega_0 < \infty$ in fact, the energetic balance which determines the critical value λ_{c2} for the incoherent pair transition is altered with respect

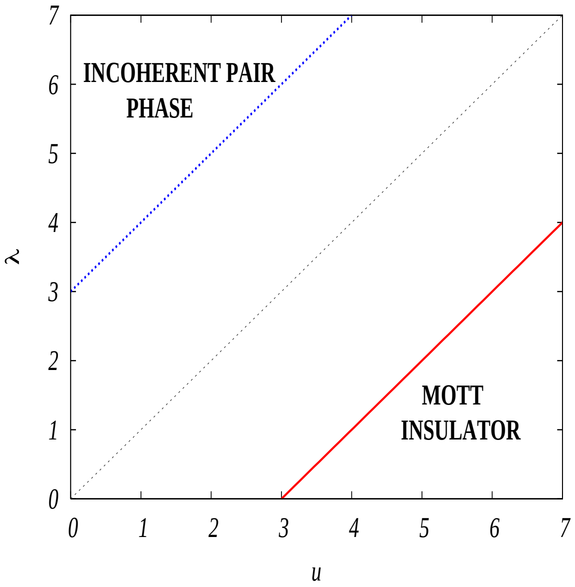

Figure 3.5: Expected phase-diagram for the antiadiabatic half-filled Hubbard-Holstein model.

of the antiadiabatic limit. It can be easily understood that λ_{c2} should be substantially smaller than U_{c2} in the adiabatic regime, for instance, because of the polaronic reduction of the kinetic energy, which makes easier for the attractive interaction to form incoherent pairs.

In summary, in this first paragraph we have analyzed the interplay between an Holstein electron-phonon interaction and a Hubbard repulsion, in the half-filled case at zero temperature, having fixed the value of the adiabatic ratio γ to 0.2. The physics of the correlation-driven Mott transition turns out to be not significantly altered by the Holstein coupling, which is almost inefficient in the strongly correlated regime where charge fluctuations are frozen. This is also evidenced in Fig. 3.1 where the dotted blue line shows that, the more u is large, the more one has to push the system towards the strong electron-phonon coupling regime, to observe the polaronic physics.

3.2 Heavy quasiparticles interacting with the lattice

Motivated by recent experiment suggesting a role of the electron-phonon interaction in the strongly correlated metallic phase of the cuprates, in the present paragraph we analyze in more detail the strongly correlated metallic region close to the Mott transition at half-filling, and discuss the role of the electron-phonon interaction on this phase.

As discussed in Sec.2.2, the local electronic spectral function evaluated with DMFT (see Eq. 2.24) is characterized, in the correlated metallic phase of the Hubbard model, by a narrow resonance at the Fermi level, together with the high-energy Hubbard bands at distance $\pm U/2$ from it. The width of the central peak is proportional to the quasi-particle residue Z, which decreases for increasing U and vanishes at the Mott transition. Due to the momentum independence of the self-energy, Z is also the inverse of the effective mass $Z = m/m^*$ (see Sec. 2.2.1).

We look at the dependence on λ of the quasiparticle residue in the correlated metallic phase, in the region where the metal has not yet developed polaronic features. On extremely general grounds, we can expect two main effects of the electron-phonon coupling on Z, starting from the above described situation:

1. **effective mass enhancement** – in the absence of Coulomb repulsion, the electron-phonon interaction is known to increase the effective mass of the quasiparticles, as we have already seen in Sec. 2.1.2. For small λ and in the adiabatic regime, m^*/m increases linearly for small λ, as it can be calculated perturbatively [23]:

$$\frac{m^*}{m} = 1 + N(E_F)\frac{2g^2}{\omega_0} = 1 + \frac{2}{\pi}\lambda \tag{3.1}$$

where $N(E_F)$ is the density of states at the Fermi level, while the last identity holds for the case of the semicircular band-dispersion (Eq. 2.18). In fact, the standard effect of the electron-phonon interaction is to form heavy quasiparticles and, consequently, to make Z decreasing with λ. This is true also in the antiadiabatic regime, in which the control parameter becomes α, as discussed in Sec. 2.1.2. In this case, the result of the strong coupling expansions is

$$\frac{m^*}{m} = \mathrm{e}^{\alpha^2} \tag{2.9}$$

with the same exponential behavior which rules the effective hopping reduction in the Lang-Firsov approach.

Therefore the width of the low energy peak in the spectral function, upon increasing the electron-phonon coupling, gets smaller, for any value of the parameter γ. One could think that the same happens also when an electron-phonon interaction is added on the correlated metallic phase, where quasiparticle excitations, although with strongly renormalized parameters, still exist.

2. **reduction of the total repulsion** – the electron-phonon interaction induces an attraction between the electrons, as said in Sec. 2.1.2 - Eq. (2.4). In fact, although the phonon-mediated attraction has a finite characteristic time scale so that it is not directly comparable to a static Hubbard repulsion, this attraction will oppose it lowering, to a certain extent, the total degree of repulsion of the system. Putting the two things together, one has a dynamical interaction between electrons with opposite spin, of the form

   $$U_{eff}(\omega) = U - \frac{2g^2\omega_0}{\omega_0^2 - \omega^2} \tag{3.2}$$

   In the antiadiabatic limit, when $\omega_0 \to \infty$, the attraction becomes actually static and equals the bipolaronic binding energy $2g^2/\omega_0$ so that this reduction effect is maximum and the model becomes a Hubbard one with coupling $U - \lambda D$. Nevertheless, independently of the value of γ, if the total repulsion in the correlated metallic phase decreases of a certain amount, the effective mass is expected to get lower.

In fact, while the first effect opposes to the electronic motion, the second instead favors the motion by screening the Hubbard repulsion. The overall effect of the electron-phonon coupling on the correlated metallic phase is therefore hard to predict on intuitive grounds. What we can expect is that the second effect should be visible when $U > 2g^2/\omega_0$, i.e. when the system is in the correlated metallic phase and in the presence of moderate electron-phonon coupling. We need thus to carefully examine Z to understand whether the second effects prevails, once the electron-phonon interaction is switched on in this region of the phase diagram. Still using the DMFT to investigate the normal paramagnetic metallic phase of the Hubbard-Holstein model at half-filling, we calculate the quasiparticle residue Z using the same value $\gamma = 0.2$ of Fig. 3.1, i.e. far from the antiadiabatic regime in which the solution to our problem has a trivial answer. In Fig. 3.6 we plot Z as a function of λ for different values of u. In the absence of Hubbard repulsion, the effect of the electron-phonon coupling is quite naturally to increase the electron effective mass, i.e. decrease Z, eventually reaching the bipolaronic transition [3]. Then we turn on the Hubbard repulsion, and plot the ratio $Z(U,\lambda)/Z(U,0)$ in order to disentangle the effect of the electron-phonon interaction from U. Increasing the value of U, the effect of the electron-phonon interaction

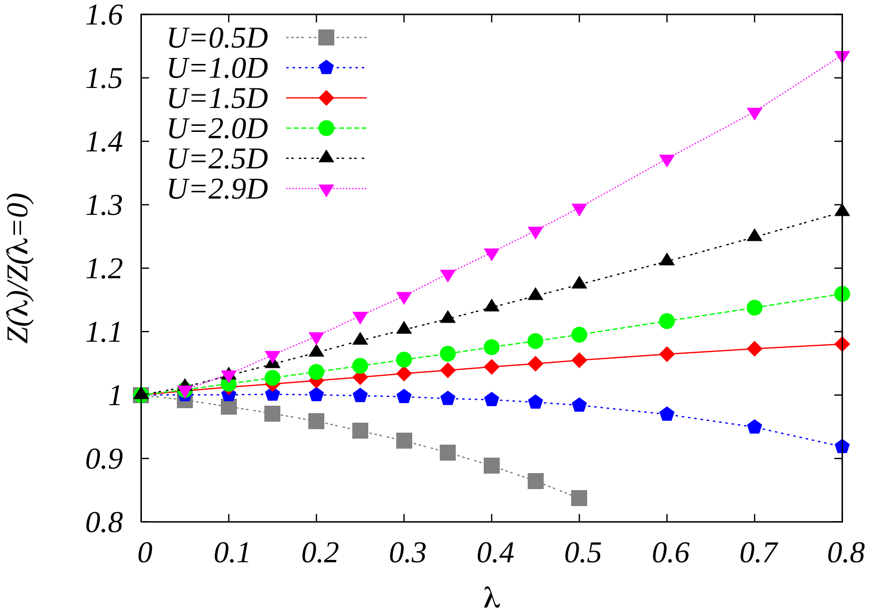

Figure 3.6: Effect of electron-phonon interaction on the quasiparticle weight Z. The ratio $Z(\lambda, U)/Z(0, U)$ is shown for different values of U and $\gamma = 0.2$.

becomes weaker, until a coupling for which the electron-phonon coupling has the surprising effect to increase Z (reduce the effective mass).

Therefore it is clear from Fig. 3.6 that, within the Hubbard-Holstein model, the predominance of one of the effects 1 and 2 depends on the value of the Coulomb repulsion: For small u the standard electron-phonon effects, characterized by a linear decrease of Z followed by an exponential one approaching the polaronic crossover, are at work. Increasing u, the reduction of the effective repulsion due to the electron-phonon coupling prevails, with, on one hand, the bare value $Z(U, \lambda = 0)$ which becomes smaller and smaller with increasing U, and, on the other hand, the full $Z(U, \lambda \neq 0)$ which increases as soon as λ is switched on. In Fig. 3.6 we have plotted the ratio $Z(U, \lambda)/Z(U, 0)$, while, in Fig. 3.7, we have plotted the value $Z(U, \lambda)$ without renormalization, as a function of U at fixed λ. The decreasing behavior of $Z(U, \lambda = 0)$ as a function of U can be seen by looking at the grey triangles (with the point facing down) in Fig. 3.7, obtained by fixing $\lambda = 0$ and varying u. The other curves correspond to larger values of λ. The evolution of Z from a decreasing function of λ to an increasing one observed in Fig. 3.6, here reflects in obtaining an increase of λ from the top curve to the bottom one, for small u, and an opposite trend

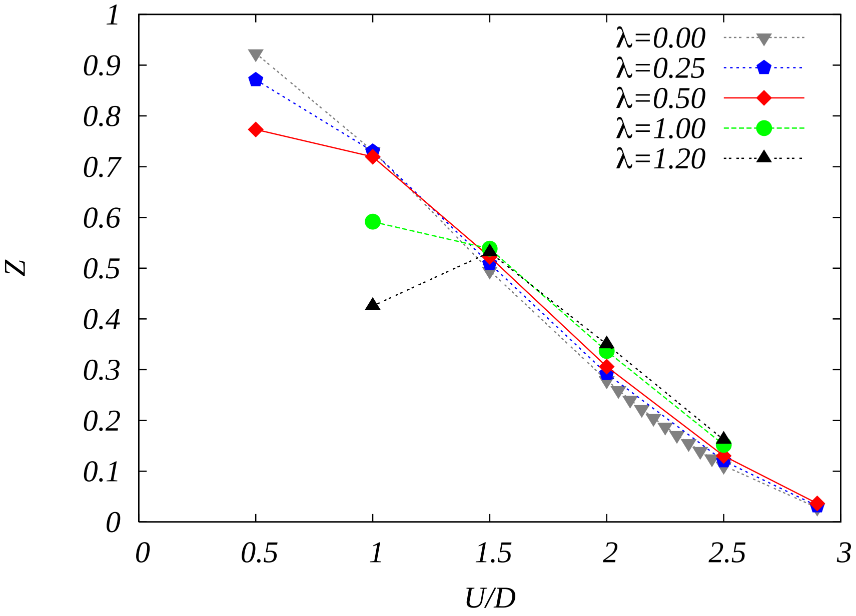

Figure 3.7: Effect of the electron-electron repulsion on the bare quasiparticle weight Z for different values of λ. The same value $\gamma = 0.2$ of Fig. 3.6 has been used.

in the right-hand part of Fig. 3.7. Interestingly, this implies a non-monotonic behavior of Z as a function of u, for $\lambda > 1$, which can be interpreted in the following way: The increasing u is destroying the initial polaronic regime and the quasiparticle residue goes again towards 1. Upon further increasing u, the strongly correlated regime is eventually reached, in which, Z becomes again a decreasing function of the repulsion and vanishes at the metal-insulator transition.

We now want to understand more deeply this regime in which, for the presence of a strong electronic repulsion, the electron-phonon interaction has the counterintuitive effect of enhancing Z and in which the screening of U by λ seems to be the dominant mechanism.

In the antiadiabatic limit ($\gamma \to \infty$) the phonon-mediated attraction, as we have said, becomes static and $u \to u - \lambda$. If we compare Z for $\gamma = \infty$ with the real Z for $\gamma = 0.2$, the antiadiabatic value overestimates the screening of the Coulomb repulsion, suggesting that, far from the antiadiabatic regime, only "a part" of the electron-phonon coupling effectively reduces U. We can try to parametrize an effective static repulsion $u_{eff}(U, \lambda, \omega_0)$ as the value of U/D for which an effective Hubbard model has the same Z as our Hubbard-Holstein model. This leads us to an ansatz for a static $u_{eff} = u - \eta\lambda$, where η is a dimensionless free parameter which has to approach 1 for $\gamma \to \infty$ and is expected to be smaller than 1 for finite γ.

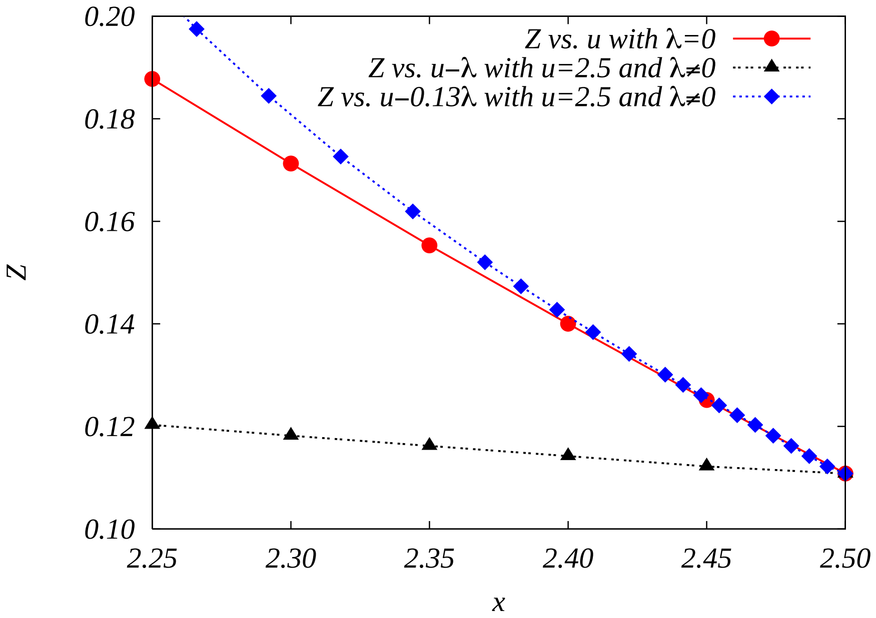

Figure 3.8: Z for the Hubbard and Hubbard-Holstein models. Solid red line with points: pure Hubbard (horizontal axis $x = u$ in this case). Dotted black line with triangles: Hubbard-Holstein as a function of $u - \lambda$ for $u = 2.5$ (horizontal axis $x = 2.5 - \lambda$ in this case). Dotted blue line with diamonds: Hubbard-Holstein as a function of $u - \eta\lambda$ for $u = 2.5$ (horizontal axis $x = 2.5 - 0.13\lambda$ in this case). In this latter case the value of η has been empirically determined in such a way that the Hubbard-Holstein curve fits the pure Hubbard one in the largest possible range of λ. In this case the values of λ range approx. from 0 to 1. In all the other cases, this range is of this order or even bigger.

In order to determine quantitatively the coefficient η and check the validity of our ansatz, we apply a fitting procedure to the quasiparticle residue as a function of λ, U and ω_0. In Fig. 3.8 we show it, using, as an example, the case $u = 2.5$ and $\gamma = 0.2$. The red solid curve with dots represents Z in the Hubbard model, as a function of U (which labels the x-axis), while the black dotted one with triangles, represents the quasiparticle residue of a full Hubbard-Holstein model with $u = 2.5$, as a function of $u - \lambda$ (the x-axis thus has to be read as $2.5 - \lambda$: $x = 2.50$ means $\lambda = 0$ and $x = 2.25$ means $\lambda = 0.25$). Looking at these two curves it is clear that an effective Hubbard model with $u_{eff} = u - \lambda$ does not reproduce the behavior of Z of the full Hubbard-Holstein model, confirming that

$\eta = 1$ overestimates the screening effect. So we look for the best curve obtained in the Hubbard-Holstein case at fixed u, that matches the pure Hubbard one. To do this, we add to Fig. 3.8 the blue dotted curve with diamonds, obtained by plotting the black curve as a function of the combination $u - \eta\lambda$. A variation of the coefficient η, therefore changes, as a consequence, its slope. The variable on the x-axis is given now, in fact, by the combination $u - \eta\lambda$, so that the blue curve has the point $\lambda = 0$ ($x = 2.5$) in common with the red and the black one, but departs from the latter one as soon as η is moved from 1. For this specific set of parameters $\eta = 0.13$ provides the best fit and gives a very good agreement in quite a wide range of the x-axis.

The relevance of our ansatz can be assessed by the behavior of η as a function of model parameters. Computing η for different values of U and ω_0, we find the behavior shown in Fig. 3.9. Each η point in the figure has been calculated following the fitting procedure described above.

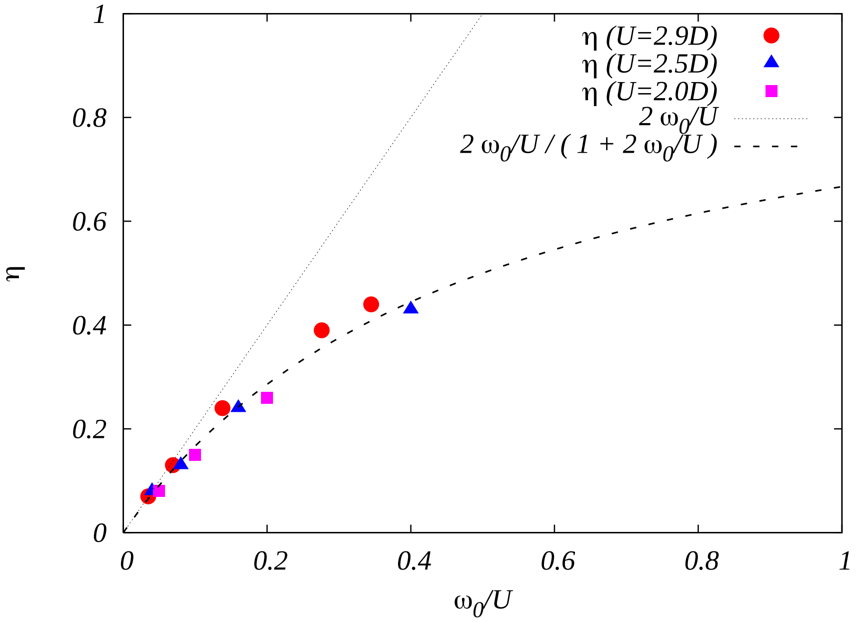

Figure 3.9: The coefficient η which measures the effective reduction of the Hubbard repulsion according to $u_{eff} = u - \eta\lambda$, plotted as a function of ω_0/U. Different symbols refer to different values of U. Dotted line: linear behavior with slope 2 valid for small ω_0/U. Dashed line: analytic result obtained resumming, in perturbation theory, all terms linear in $\lambda D/U$ (see Eq. 3.9).

The result of Fig. 3.9 directly answers to our question about the value of η in the adiabatic regime: For relatively small ω_0/U, we find that η has a linear behavior in ω_0/U, so it is directly proportional to the phonon frequency ω_0 and inversely proportional to U. This means that, as it is reasonable, η is vanishing approaching the adiabatic limit (see Eq. (A.11) of Appendix A). For $\omega_0 = 0$, in fact, the electron-phonon interaction is nonzero only for $\omega = 0$ (see Eq. (2.4)) and the width of the frequency window in which the Hubbard repulsion is contrasted by the electron-phonon interaction becomes zero. The direct proportionality to ω_0, is encouraging also for another reason: From its definition, η is somehow supposed to contain all the dynamical information coming from the phonon-mediated attractive interaction with scale ω_0, so this is the natural way to take into account for this property. The inverse proportionality, instead, with respect of U is, in a way, harder to predict. One could have been tempted to measure the degree of adiabaticity by introducing a sort of effective $\tilde{\gamma} = \omega_0/(ZD)$, where the phonon frequency is compared to the effective bandwidth. ZD, given the small values of Z in the strongly correlated regime, would be much smaller than the bare bandwidth. Consequently, upon increasing U, one would have approached effectively an antiadiabatic regime, so that η should have increased toward 1. This is in contrast to our results which show the opposite trend. The previous argument in fact, does not consider the relevant dynamics associated to the processes involved in the quasiparticle formation. As we will see in the following section, the Kondo processes associated to the coherent peak at the Fermi level, have a time scale $\propto 1/U$, and become faster and faster with increasing the Coulomb repulsion. On the other hand, the phonon time scale is fixed to a scale $\propto 1/\omega_0$ so that, the more U is large, the more the quasiparticle processes become instantaneous with respect to the phonon dynamics, resulting in an adiabatic effective regime, and, consequently, in a smaller η.

After the initial linear behavior, η bends down to eventually reach the asymptotic value $\eta = 1$. It is apparent from Fig. 3.9, that the η points calculated for different values of u and ω_0 fall more or less on a single curve. To be more precise, one can identify three curves, one for each fixed value of u, which are very close one another. Nevertheless, each of these three families follows nicely a behavior of the form $x/(1+x)$, with $x = 2\omega_0/U$, represented by the dashed line in Fig. 3.9. We will discuss this extensively in the following section.

This analysis of the quasiparticle weight thus suggests that the effect of electron-phonon interactions on the strongly correlated metallic phase of the Hubbard model is a partial screening of the repulsion, and the degree of screening is controlled by ω_0/U.

3.3 Effects of the electron-phonon interaction on Kondo processes

In the previous section we have found that the quasiparticle residue of Hubbard-Holstein model in the strongly correlated regime and in a quite large range of λ (typically from 0 to 1), can be reproduced through a pure Hubbard model with a rescaled repulsion u_{eff}. This effective interaction is equal to $u - \eta\lambda$, where the dimensionless parameter η is a function of u and ω_0, which is linear in ω_0/U for $\omega_0 \ll U$ and asymptotically reaches the value of 1 in the opposite limit. Of course, at this level, this result could sound of little physical significance, since it comes simply from a fit procedure. This section aims to give a physical meaning to these findings.

Z also measures the width and weight of the low-energy feature in the single-particle spectral function. Thus, it is natural to compare the spectral function for the Holstein model with the correspondent quantity for the equivalent Hubbard model with reduced repulsion. In Fig. 3.10 we compare the densities of states for the system coupled to phonons (blue dashed line) and the effective pure electronic one (red solid line), in four different cases. Each of the four panels contains, therefore, an example of a density of states for the Hubbard-Holstein model in the strongly correlated regime and moderately adiabatic regime, i.e. for a small value of the combination ω_0/U (see caption), compared to a density of states of the corresponding effective pure Hubbard model with $u_{eff} = u - \eta\lambda$. The three upper panels are for $\lambda = 1$, while the lowest one has $\lambda = 0.5$. This means that we are comparing the full model with phonons and the effective static one without phonons, for intermediate values of the electron-phonon coupling. Three main points emerges, from Fig. 3.10 as well as by the analysis of other collected data, not shown here:

1. as expected, the spectra of both the Hubbard-Holstein and the Hubbard model, have the central peak and the high-energy bands, characteristic of a strongly correlated metal at half-filling[2].

2. as far as $\omega_0 \ll U$, the full model with phonons and the pure Hubbard one with the effective repulsion, not only have the same value of Z, but also display a big

---

[2] The Hubbard bands are made of thick separate peaks, since, as we have explained in Sec. 2.3.1, they come from an Exact Diagonalization calculation.

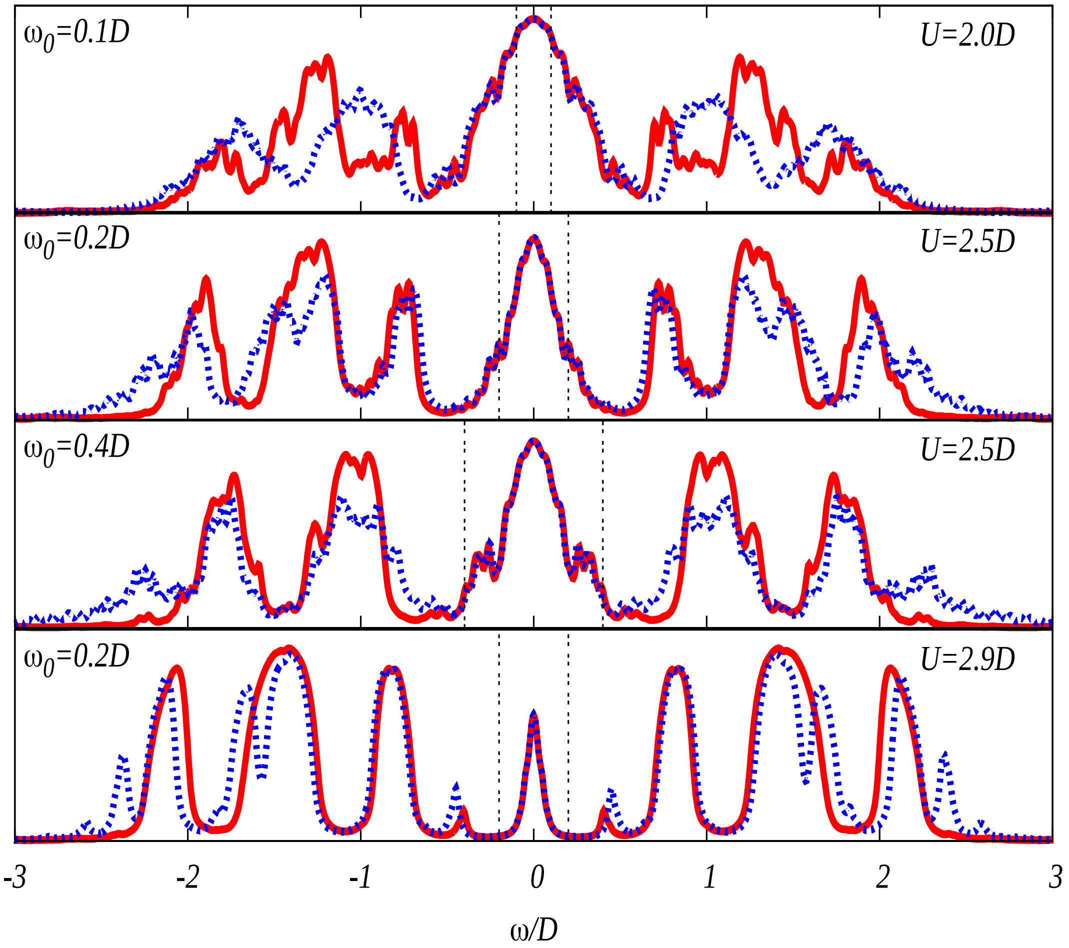

Figure 3.10: The electron spectral function for the Holstein-Hubbard model (dashed curve), compared with a pure Hubbard model with total repulsion equal to $U - \eta\lambda D$ (solid curve), for different values of U and ω_0 (the latter quantity is evidenced by the dot-dashed vertical line). In the three upper panels we have used $\lambda = 1$, while, in the lowest one, $\lambda = 0.5$. The values of the repulsion $U - \eta\lambda D$ used for the spectra of the effective Hubbard model (red solid curves) are, from top to bottom: $1.92D$, $2.37D$, $2.25D$ and $2.84D$.

portion of the low-energy spectra which is basically identical. In other words, no signs of the electron-phonon interaction are visible in the low-energy structure, once the rescaling of u has been done.

3. the same rescaling used for the quasiparticle residue Z and which reproduces the whole low-energy part of the spectra, works for the high-energy part. In fact, the Hubbard bands of the effective pure electronic model with u_{eff} are placed more or less at the same position as the full one with phonons. The interesting result is that signs of the electron-phonon coupling are quite visible at these scales; the peaks in the density of states of the full model are broadened by the electron-phonon interaction and the typical phononic satellites, not reproducible by a pure electronic model, are present.

This findings strongly suggest that our reduction of the dynamical effective interaction to a static quantity is more than a mere fitting, and it unveils some basic physics. We can gain some understanding of this scenario by exploiting the fact that the quasiparticle peak is associated within DMFT to the Kondo effect in the Anderson impurity model [47]. In fact, the formation of the quasiparticle coherent peak coming from the insulating side is associated, in DMFT, to a Kondo effect.

Recently, the Kondo coupling J_K in the presence of an electron-phonon coupling has been calculated, for the Anderson-Holstein model. For large U, the problem is solved by perturbatively projecting out the empty and double occupied states for the impurity deriving an effective Hamiltonian for spin fluctuations [96, 97]. The result is given by

$$J_K(\lambda) = J_K(0) \sum_{m=0}^{\infty} \frac{\left| \langle 0 | \mathrm{e}^{\alpha(a-a^\dagger)} | m \rangle \right|^2}{1 - 2g^2/\omega_0 U + 2m\omega_0/U} \tag{3.3}$$

where the states with zero and m phonons are denoted, respectively, by $|0\rangle$ and $|m\rangle$. Expression (3.3) can be rewritten in a more transparent way, after the following identities

$$\left| \langle m | \mathrm{e}^{\alpha(a^\dagger - a)} | 0 \rangle \right|^2 = \left(\langle m | \mathrm{e}^{-\frac{\alpha^2}{2}} \sum_{l=0}^{\infty} \frac{\alpha^l}{\sqrt{l!}} | l \rangle \right)^2 = \left(\mathrm{e}^{-\frac{\alpha^2}{2}} \frac{\alpha^m}{\sqrt{m!}} \right)^2 = \frac{\alpha^{2m}}{m!} \mathrm{e}^{-\alpha^2} \tag{3.4}$$

The sum in Eq. (3.3) becomes

$$J_K(\lambda) = J_K(0) \mathrm{e}^{-\alpha^2} \sum_{m=0}^{\infty} \frac{\alpha^{2m}}{m! \left(1 - \frac{2g^2}{\omega_0 U} + m \frac{2\omega_0}{U} \right)} \tag{3.5}$$

In the limit $U \to \infty$, the summation over m appearing in Eq. (3.5), completely cancels the exponential $e^{-\alpha^2}$, and one is left with the pure electronic result $J_K(0) = 16V^2/U$, with no signs of the electron-phonon interaction[3]. For finite U, the Kondo coupling is still weakly affected by the electron-phonon interaction, provided that U is larger than any phononic energy scale. In fact, the Kondo coupling arises, at the leading order in $1/U$, from virtual processes in which doubly occupied sites are created, with an energy cost of order U. In the presence of an electron-phonon coupling, the intermediate states can have an arbitrary number of phonons, but, if $\lambda \ll u$ and $\gamma \ll u$, the summation in Eq. (3.5) almost completely compensates the exponential behavior leading to small corrections in $J_K(\lambda)$ with respect to the pure electronic result. Expression (3.5) can be expanded for weak electron-phonon coupling resumming all terms linear in $2g^2/\omega_0 U = \lambda D/U$ (see Appendix A and Ref. [96]):

$$J_K(\lambda) \simeq J_K(0)\left(1 + \frac{\frac{2\omega_0}{U}}{1+\frac{2\omega_0}{U}}\frac{\lambda D}{U}\right) \tag{3.6}$$

This result is actually closely related to a previous calculation addressing the effect of electron-phonon coupling on the superexchange coupling in a Hubbard model [98].

To see the correspondence of this with our DMFT result on the rescaling of the total repulsion, one can write the Kondo coupling in terms of $u_{eff} = u - \eta\lambda$:

$$J_K(\lambda) = \frac{16V^2}{u_{eff}D} = \frac{16V^2}{U - \eta\lambda D} \tag{3.7}$$

Expanding this expression for small values of $\lambda D/U$

$$J_K(\lambda) \simeq J_K(0)(1 + \eta\frac{\lambda D}{U}) \tag{3.8}$$

the comparison with Eq. (3.6) gives the following identification:

$$\eta = \frac{2\omega_0/U}{1 + 2\omega_0/U} \tag{3.9}$$

In perfect agreement with the result of Fig. 3.9, this expression starts linearly in ω_0/U with slope equal to 2 and asymptotically reaches 1 for large ω_0/U. In other words, for small ω_0/U, the effect of the electron-phonon interaction on the strongly correlated metallic phase, can be synthesized through a slight renormalization of the Hubbard repulsion

$$u_{eff} \simeq u - \frac{2\omega_0}{U}\lambda \tag{3.10}$$

---

[3] V^2 indicates an average of the square of the hybridization parameter over the Fermi surface.

while, for large ω_0/U, the electron-phonon coupling λ subtracts completely to the Hubbard repulsion.

We can therefore understand the picture that emerges as follows: When U is large, quasiparticle motion arises from virtual processes in which doubly occupied sites are created. Obviously, these processes are not so frequent, since the energy scale associated is large, but they are instantaneous, and consequently they are only poorly affected by phonon excitations since these, if ω_0 is small with respect to U, have a characteristic low time scale. Therefore, despite the overall electron motion is quite slow due to the small number of virtual processes (which is reflected by the large effective mass), the electron-phonon interaction does not affect it so much.

The new parameter η has thus also the properties of setting a new criterion for the antiadiabatic limit for a strongly correlated system coupled to phonons: Only for $\omega_0 \gg U$, in fact, $\eta = 1$ is obtained. The phonon frequency can be larger than D, but, in the presence of U, the antiadiabatic limit is guaranteed only if ω_0 is larger than U too.

Before coming to the discussion of the isotope effect, which will conclude this chapter, it is interesting to compare the values of $U_{c2}(\lambda)$ calculated for the full Hubbard-Holstein model, with the values obtained through the effective Hubbard model with $u_{eff} = u - \eta\lambda$. The critical value for the metal-insulator transition in the effective Hubbard model can be calculated as $u_{eff}D = U_{c2}(\lambda = 0)$, which means

$$U - \frac{2\omega_0/U}{1 + 2\omega_0/U}\lambda D = 2.92 \tag{3.11}$$

This relation defines a curve in the U-λ plane, which we have depicted in the phase diagram of Fig. 3.1 by a dashed curve labeled by “eff. Hubbard model”. The agreement with the calculated values of U_{c2} of the Hubbard-Holstein model is very good up to $\lambda \sim 1$. For larger values of the electron-phonon interaction, in fact, the definition of the effective Hubbard model is questionable, since the repulsion U ceases to be the largest scale of the problem.

We now make some brief considerations on the last issue of the present section: the isotope effect. The slight rescaling of the Hubbard repulsion caused by the electron-phonon interaction that we have found in a strongly correlated metallic system, can have dramatic effects on quantities which depend strongly on the distance from the critical value U_{c2} for the metal-insulator transition. Among these, there is the effective mass of quasiparticles, m^*, which grows rapidly approaching the metal-insulator transition. Therefore, since the effective repulsion u_{eff} depends linearly on $\eta \simeq 2\omega_0/U$, a small change in ω_0 corresponds to an big change in $Z = m/m^*$, not accounted for by any perturbative approach. As a consequence, we expect a large isotope effect on m^*.

Since the Hubbard-Holstein model reduces to an effective Hubbard one with $u \to u_{eff}$, close to the Mott transition the effective mass will depend in the same way as in the pure Hubbard model on the distance from the U_{c2} [47]:

$$\frac{m^*}{m} = \frac{U_{c2}}{C_Z} \frac{1}{U_{c2} - u_{eff} D} \tag{3.12}$$

where C_Z is a coefficient of order 1. The isotope coefficient on the effective mass is calculated as [26]

$$\alpha_{m^*} = \frac{1}{2} \frac{d \log(m^*/m)}{d \log \omega_0} \tag{3.13}$$

so

$$\log \frac{m^*}{m} \propto \log \frac{1}{U_{c2} - u_{eff} D} = -\log\left(U_{c2} - u_{eff} D\right) = -\log\left(U_{c2} - U + \eta\lambda\right) \tag{3.14}$$

The term containing η has a dramatic consequence on α_{m^*}, with respect to the standard Fermi liquid prediction, obtained by expanding m^* to the subsequent order in γ with respect to the Midgal-Eliashberg theory [26]:

$$\alpha_{m^*} = \frac{\gamma}{2} \frac{m}{m^*} f'(\lambda) \tag{3.15}$$

where $f(\lambda)$ is a mass-enhancement factor. In fact, we have

$$\frac{d \log(m^*/m)}{d \log \omega_0} = -\frac{1}{U_{c2} - U + \eta\lambda} \frac{d\left(U_{c2} - U + \eta\lambda\right)}{d \log \omega_0} \tag{3.16}$$

so that the *opposite* dependence on the effective mass is obtained with respect to Eq. (3.15):

$$\alpha_{m^*} = \frac{1}{2} \frac{d \log(m^*/m)}{d \log \omega_0} = -\frac{C_Z}{U_{c2}} \frac{m^*}{m} \frac{\omega_0}{U} \lambda \tag{3.17}$$

The effective Hubbard model obtained from the full Hubbard-Holstein one, therefore, displays a dramatically large negative isotope effect on the effective mass:

$$\alpha_{m^*} \propto -\frac{1}{Z} \tag{3.18}$$

which *diverges* approaching the transition.

Chapter 4

Phase separation close to the Mott-Hubbard transition

4.1 Density-driven Mott transition

After the discovery of high-temperature superconductivity in cuprates, the search for a theory of this phenomenon determined a dramatic rise in the interest in strongly correlated systems. We have already discussed this in detail in Chapter 1, where we have exposed the most important properties of Copper-oxides: first of all they are antiferromagnetic Mott insulators at half-filling, and, by doping, superconductivity is found with high critical temperatures. This is accompanied by the anomalous features of the non-superconducting metallic phase, which, for small doping, displays the pseudogap phenomenon, a clear tendency to charge-order fluctuations, a linear behavior of resistivity at optimal doping in a extremely wide range of temperatures and so on.

In these and in other anomalies, the strong electronic correlation present in the cuprates, certainly plays an important role. Still in Chapter 1 we have, in fact, given the main motivations for using the t-J model to describe their physics. Nevertheless, although this certainly captures the fundamental properties of a correlated electronic system, it is not a realistic and complete microscopic model for the complicated electronic and crystal structure of the cuprates and, more importantly, it neglects the role of the lattice degrees of freedom. On the contrary, the electron-phonon coupling seems to be important as indicated by many recent experiments (see Sec.1.3), so that, although its behavior is still very puzzling, the inclusion of the electron-phonon interaction in the presence of strong electron-electron interaction is compelling and it is probably one of the unavoidable ingredients for the study of the cuprates.

Since the interesting physics of these compounds emerges at finite doping, and many properties have unusual doping dependence, in this chapter we study the normal phase of a strongly correlated system coupled to phonons for finite values of the doping, extending the analysis of the Hubbard-Holstein model out of the special half-filling situation.

As explained in Sec.2.2.1, the Hubbard model displays, for $n \neq 1$, a metallic phase also for large values of the Coulomb repulsion ($U > U_{c2}$). In this large and interesting new region of the parameter space of our model, the influence of the electron-phonon coupling becomes harder to predict. In our case, we can expect that the electron-phonon interaction should have a deeper influence on the metallic phase, compared to the half-filled case, since density fluctuations are less frozen if $n \neq 1$.

Some indications come from slave-boson studies of the Hubbard-Holstein model (see Sec.2.1.3) finding a phase separation induced by phonons, for intermediate values of λ [72, 73, 74].

Strongly correlated systems have a natural tendency towards phase separation, due to the reduced kinetic energy. In the pure Hubbard model, for example, the system presents phase separation for finite values of the doping, between the Néel antiferromagnet and the paramagnetic metal [99]. In a recent DMFT study on the density-driven Mott transition, phase separation has been found at finite temperatures [100]. In that case, due to the different entropies of the metallic and the insulating phases, the free energy balance is influenced by the finite temperature and, as a consequence, the transition changes from second to first order.

It is therefore interesting to find out whether the electron-phonon interaction can change the order of the density-driven Mott transition at zero temperature and induce phase separation between the metallic and the insulating phase.

We will proceed in close analogy with the case of phase coexistence in gas-liquid mixtures. Phase separation is signaled by the fact that, at low temperatures, the Gibbs function of the liquid and gas phases cross for a given value of the pressure (see, e.g. [101]). In out case, the independent variable is the chemical potential μ, which determines the value of the density n. The stable phase is found by comparing the grand-canonical potentials Ω of the metallic and the insulating phases

$$\Omega = E - TS - \mu n = -PV. \tag{4.1}$$

The analysis of the behavior of Ω as a function of μ says whether or not phase separation takes places. In fact, if the grand-canonical potentials of two phases cross each other, a first order transition occurs and, for that particular value of μ, the system lives as a mixture of two phases with two different densities. This can be easily seen by observing that, at the crossing point, the slopes of Ω for the two solutions must be different. Since the slope of $\Omega(\mu)$ is the opposite of the density

$$n = -\frac{\partial \Omega}{\partial \mu}, \tag{4.2}$$

two phases with a different number of particles coexist.

In the next section, in order to see whether the Hubbard-Holstein model displays phase separation close to the density-driven Mott transition, we will therefore look for a crossing of the grand-canonical potentials of the metallic and the insulating phases.

4.2 Thermodynamic instability induced by the electron-phonon coupling

In order to analyze the effect of the electron-phonon coupling on the density-driven Mott transition, we apply DMFT to the Hubbard-Holstein model, working with $U > U_{c2}$ so that, as we have said, only the Mott insulating phase exists at half-filling. As soon as $n \neq 1$, the stable phase becomes the metallic one (see Fig. 2.4). We fix U to a large value and switch on the electron-phonon coupling λ, in the relatively adiabatic regime $\omega_0 = 0.2D$.

Before showing the DMFT results, we can make the following considerations, based on the discussion of the previous paragraph: On intuitive grounds, the electron-phonon interaction favors the insulating phase with respect to the metal. When the electron-phonon interaction is turned on in the metallic state, two competing effects take place. On one side, the electrons gain potential energy if the lattice is distorted, while, on the other, the effective mass is enhanced, leading to a loss in kinetic energy. As a result of this competition, the electrons cannot completely exploit the electron-phonon coupling to lower the energy. On the other hand, the electrons in the Mott insulator are already localized, so that they can gain potential energy by coupling with phonons without losing kinetic energy. This simple argument already tells us that the energetic balance between the two phases will be changed in favor of the insulator. For the same reasons we can also expect the region of μ where the insulator exists to be larger, i.e., that μ_{c1} (see Fig. 4.1) becomes smaller with increasing λ. We notice that simplified approaches, as the one based on Lang-Firsov and squeezing transformations [102] also suggest that the insulating behavior may be favored by the electron-phonon interaction. As we have seen in Sec.2.1.2, within this approaches the Hubbard-Holstein model is transformed into a Hubbard model with reduced hopping $t^* = te^{-\alpha^2}$, in which the insulating behavior is clearly favored with respect to the case where the electron-phonon interaction is absent.

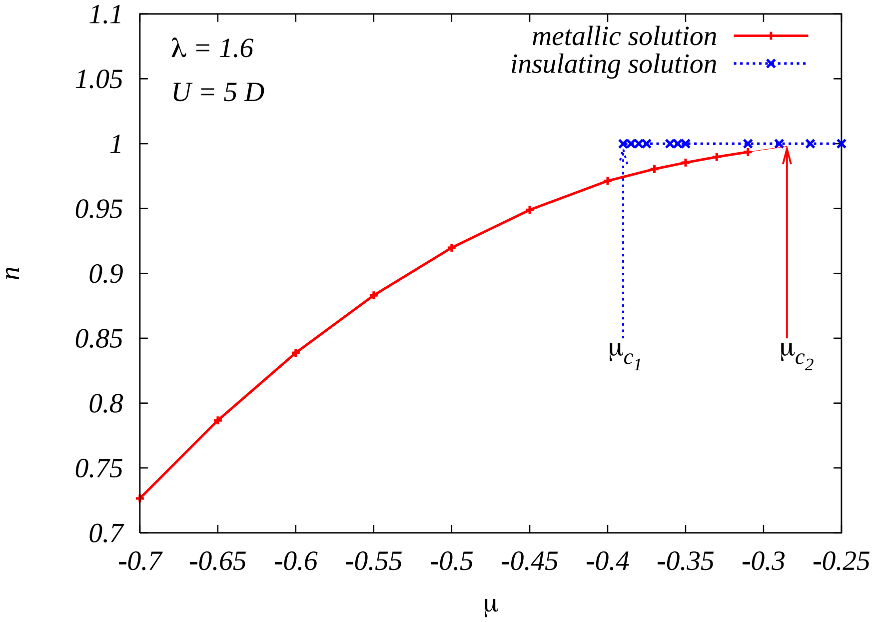

Figure 4.1: n vs μ for the insulating and the metallic phase for the Hubbard-Holstein model with $u = 5$, $\lambda = 1.6$ and $\gamma = 0.2$. μ_{c1} and μ_{c2}, denoted by the vertical arrows, represent, respectively, the values where the insulating and the metallic solution disappear.

These naive arguments are confirmed by the DMFT calculations, which show how, for sufficiently large electron-phonon coupling λ, the insulating phase becomes the stable one in the coexistence region. This is determined through a direct calculation of the grand-canonical potential in the two solutions [1] (The behavior of the grand-canonical potential with λ, has been reported in Fig. 4.3, for a larger value of u).

We illustrate the consequences of this result in Figs. 4.1 and 4.2, where the density of the two solutions, the half-filled insulating and the metallic one with $n < 1$,[1] are reported as a function of the chemical potential μ. The values of the parameters used are $u = 5$ and $\lambda = 1.6$.

---

[1] We consider here hole doping ($n < 1$). Owing to the particle-hole symmetry of the model, this is completely equivalent to electron-doping ($n > 1$)

In Fig. 4.1 the metallic and the insulating curves are both shown. As in the case of the pure Hubbard model the insulating solution (in blue in Fig. 4.1) exists for $\mu > \mu_{c1}$, and the metallic one (in red) for $\mu < \mu_{c2}$, with $\mu_{c1} < \mu_{c2}$ so that a coexistence region is found in between. The metal has a finite compressibility for all values of μ, much as in the case of $\lambda = 0$ at zero temperature.

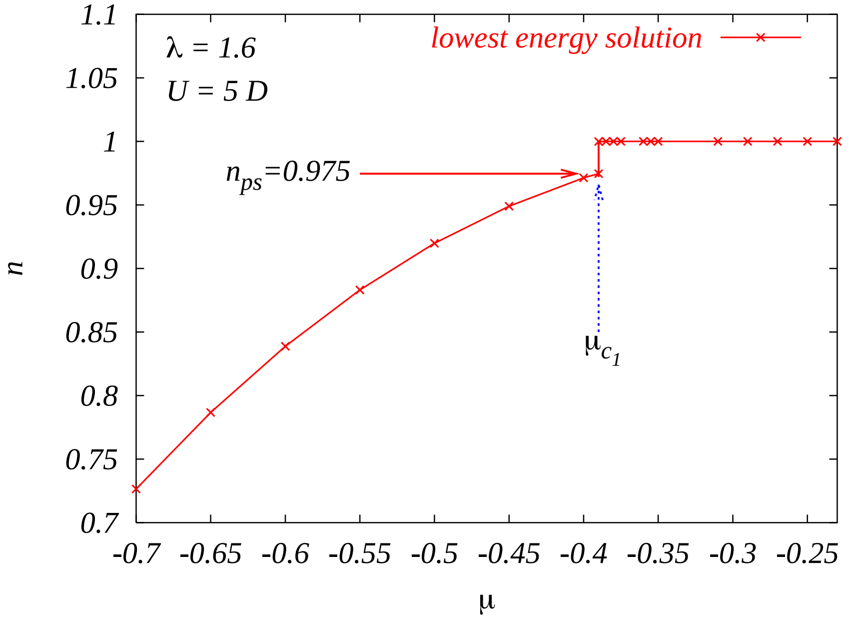

Figure 4.2: n-μ curve for the same parameters of Fig. 4.1 showing the solution with the lowest Ω for each μ. The jump in the density occurs at μ_{c1}, i.e. the insulator has a lower energy than the metal in the whole coexistence region. The density of the metallic solution, at μ_{c1}, is equal to 0.975, while that of the insulator is equal to 1.

It turns out that, contrary to the pure Hubbard case, the insulating solution is stable in almost the whole coexistence region and the n vs. μ curve of Fig. 4.1 becomes that of Fig. 4.2. Here we have in fact plotted the “physical” solution, i.e. the one with the lowest energy. In Fig. 4.2, the phase separation is signaled by the jump in the density for $\mu = \mu_{c1}$. For this value of the chemical potential the system thus lives as a mixture of two phases, one insulating with $n = 1$ and the other metallic with $n = n_{ps}$, and it is not possible to obtain a stable system with $n_{ps} < n < 1$.

We have repeated this analysis for different values of u and studying the evolution with the electron-phonon coupling λ. In Fig. 4.3, the n-μ curves for three increasing values

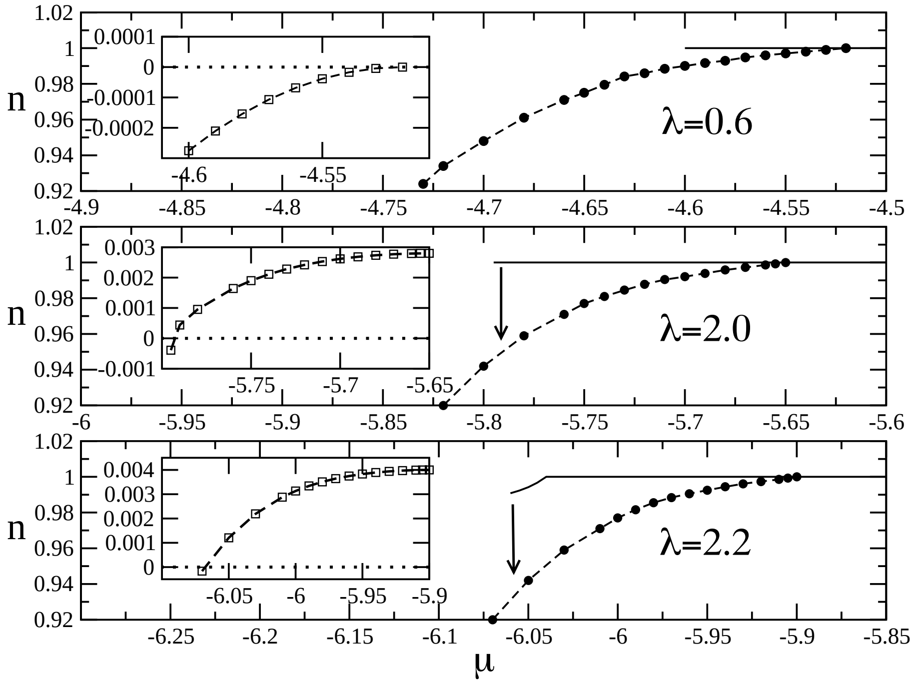

Figure 4.3: n-μ curves for $u = 10$ for $\lambda = 0.6, 2.0$ and 2.2 (from Ref. [1]). Solid circles joined by a dashed line denote the metallic solutions, and the solid line marks the insulating one. The insets show the difference between the grand canonical potentials of the two phases $\Delta\Omega = \Omega_{met} - \Omega_{ins}$. In the two lower panels this quantity is positive signaling the stability of the insulator. An arrow marks the transition point on the n-μ curves.

of λ are plotted for $u = 10$. In the insets of the various panels we show the behavior of the $\Delta\Omega = \Omega_{met} - \Omega_{ins}$ in the whole coexistence region which is negative when the metal is favored, while, vice versa, the insulator wins in the opposite case. $\Delta\Omega$ is also useful to understand whether the transition is of first or second order: If it reaches zero with a vanishing slope, i.e. with no discontinuity in the first derivative of the thermodynamic potential, the transition is of second order, while, if the slope of $\Delta\Omega$ is finite when it crosses the zero, Ω_{met} and Ω_{ins} cross each other and transition is of first order.

For $\lambda = 0$ (not shown in Fig. 4.3) we recover the known results for the Hubbard model, with two solutions in a really small μ interval, and the metal is stable in the whole coexistence region. For small values of λ (upper panel of Fig. 4.3) we observe a slight increase of the coexistence region, but the metal stays at lower energy than the insulator. In fact, similarly to the case for $\lambda = 0$, $\Delta\Omega$ is negative, the transition is of second order and occurs for $\mu = \mu_{c2}$. For $\lambda > 1$ the grand-canonical potential of the insulator becomes lower than the one of the metal. In the middle panel of Fig. 4.3 we show the result for $\lambda = 2$ where it can be seen that $\Delta\Omega$ is positive and crosses zero with a finite slope, close to μ_{c1}. This leads, as said in the previous section, to a jump of the occupation number by continuously varying the chemical potential, which is indicated in the main panels by a vertical arrow at the corresponding value of μ. Again, as in the example of Fig. 4.2, the system is not stable in the interval of density between which the jump occurs, and it undergoes phase separation between the insulating solution with $n = 1$ and a metallic solution with density $n_{ps}(\lambda)$.

A phase diagram can be built by looking at the position of the jump in the density as a function of the electron-phonon coupling λ. In Fig. 4.4 this is done by putting the doping level $\delta = 1 - n$ on the x-axis and λ on the y-axis. On the vertical line $\delta = 0$ there is the half-filled Mott insulating solution, while the curve with solid squares corresponds to $\delta_{ps}(\lambda)$. For $\lambda < 1$ there is no phase separation while, for larger values, $\delta_{ps}(\lambda)$ increases with λ. The two curves delimit a region in which the system is unstable and, for fixed value of λ, phase separation takes places between the Mott insulator with $\delta = 0$ and the metal with doping level given by the corresponding curve $\delta_{ps}(\lambda)$.

If we further increase the coupling, the effect of the electron-phonon interaction becomes even more dramatic. In the case of $u = 10$, and $\lambda \simeq 2.2$, in fact, the insulating solution continuously evolves into a phase with density slightly smaller than 1. The insulator is still energetically favored in the coexistence region (see inset of lower panel in Fig.

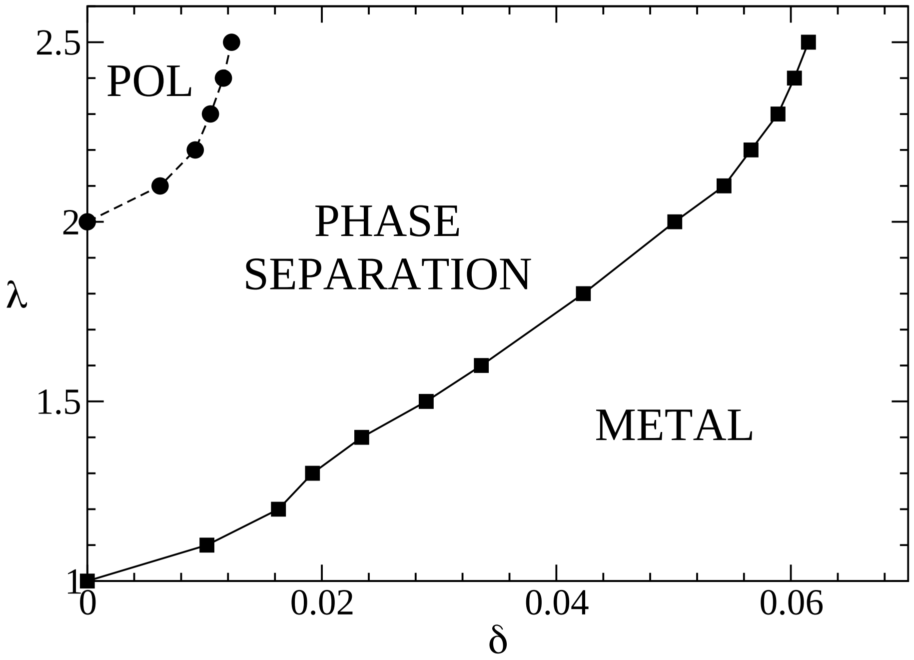

Figure 4.4: Phase diagram at zero temperature for $u = 10$ and $\omega_0 = 0.2D$, as reported in Ref. [1]. The doping value δ_{ps} ($n_{ps} = 1 - \delta_{ps}$) is plotted in solid squares as a function of the electron-phonon coupling λ which ranges, on the vertical axis, from 1 to 2.6. The half-filled Mott insulating phase lives along the whole vertical line $\delta = 0$. For $\lambda > 2$ the phase separation is between a metal and an insulating phase with finite doping and polaronic features (solid circles).

4.3), and, interestingly, this insulating state with $n \neq 1$ displays polaronic features. In fact, it is found that the evolution from the $n = 1$ insulator to this state is accompanied by a change from a unimodal distribution of the phonon displacement to the bimodal distribution characteristic of the polaronic state On the other hand, the metallic solution does not display polaronic features for the same values of λ and so the phase separation in this region, takes place between a polaronic insulator and a non-polaronic metal. This confirms that it is much harder to have polaronic effects on the delocalized metallic phase.

We have found that, in the insulating phase, the system goes slightly out of half-filling with increasing λ and starts to display polaronic features for large, but finite values of the electron-phonon coupling. This kind of evolution is totally unexpected, in light of the results found for smaller values of u. In fact, the polaronic crossover line that we have calculated in the phase diagram of Fig. 3.1 gets monotonically larger with increasing u, so that, extrapolating up to $u = 10$, the system would be non-polaronic in a wide range of λ. In any case, even for enormously large values of the electron-phonon coupling, one expects to reach a *bipolaronic* insulator, as much as it happens for $u \lesssim 3$ (see Fig. 3.1). This shows how the localized phase can influenced by the electron-phonon interaction even for large values of U.

Our findings could be related to some experimental observations in the cuprates. First of all the presence of a (phonon-induced) phase separation close to a Mott insulating phase is suggestive of a chemical potential plateau inferred from photoemission experiments in underdoped cuprates [103]. The formation of doping-induced metallic states with a chemical potential slowly varying with doping inside a Mott gap was also recently deduced from tunneling experiments [104]. In the same experiment, the small mixing of the metallic (superconducting) phase with the antiferromagnetic insulating one indicates that a spatial separation of the two phases can have small interfaces suggesting that the presence of long-range Coulomb forces can easily induce small-scale (presumably stripe-like) domain formation. We also remarkably found that for rather large values of the electron-phonon coupling ($\lambda > 2$ in the $U = 10D$ case) a phase separation can occur between an insulator away from half-filling with a finite density of polarons and a good metal with nearly free carriers. Also this situation of coexisting (but spatially separated) polarons and free carriers could find a realization in underdoped cuprates [105].

4.3 The metallic side of the phase separated region

In this section we give a closer look at the metallic phase and study how its properties are influenced by the electron-phonon interaction. We will extend our analysis to the metallic phase, also when this is not the stable one, i.e. also for those values of λ for which the insulating solution is the stable one in the coexistence region. In particular we will focus on two quantities: the charge compressibility and the quasiparticle weight, both indicative of the metallic behavior of the system in the presence of an electron-phonon coupling.

4.3.1 charge compressibility

Up to now we have found that the Hubbard-Holstein model displays phase separation close to half-filling, due to a first-order phase transition between the insulator and the metal. There have been previous claims of phase separation in the Hubbard-Holstein model mainly based on slave-boson approaches [72, 73]. Even if the main conclusion seems to be the same, a major difference must be underlined. We have shown, in fact, that phase separation occurs close to half-filling, just like in the large$-N$ treatment of the same model. In these studies, however, although prevented by the first order transition due to the Maxwell construction, a divergent compressibility is found within the metallic phase. In our DMFT approach, on the contrary, the electron-phonon interaction does not lead to divergence, but only to a sizable enhancement of the charge compressibility of the metal.

In the infinite-U limit, the large$-N$ approach has found that the charge compressibility is well represented by a simple RPA-like formula,

$$\kappa(\lambda) = \frac{2N^*}{1 + (F_0^S)_e + (F_0^S)_{ph}}, \tag{4.3}$$

where $\kappa(\lambda)$ is the compressibility for a given value of the electron-phonon coupling λ, N^* is the quasiparticle density of states per spin at the Fermi level, $(F_0^S)_{e(ph)}$ is the electronic (phononic) contribution to the symmetric Landau amplitude, and $(F_0^S)_{ph} = -4N^* g^2/\omega_0$, which can be much larger than our λ for the presence of the quasiparticle DOS instead of the bare semi-bandwidth. From Eq. (4.3) it is easy to derive the following expression

$$\frac{\kappa(\lambda)}{\kappa(0)} = \frac{1}{1 - \kappa(0)\lambda D} \tag{4.4}$$

in which all the correlation effects are contained in the purely electronic compressibility calculated at $\lambda = 0$. This implies that, if the electronic compressibility is large, a small or moderate electron-phonon coupling is sufficient to make the system unstable in the charge channel.

In our approach, κ is evaluated directly as the derivative of the number of particles n with respect of the chemical potential μ, and this can be done also following the metallic solution in the regime where it is metastable. In the previous section (see Figs. 4.1 and 4.3), we have seen that the n-μ curves of the metallic solutions have a small finite slope when they approach $n = 1$. However, if we consider the compressibility at fixed density as a function of λ, it turns out that the electron-phonon interaction is substantially increasing it. In Fig. 4.5 we present the inverse of the normalized compressibility as a function

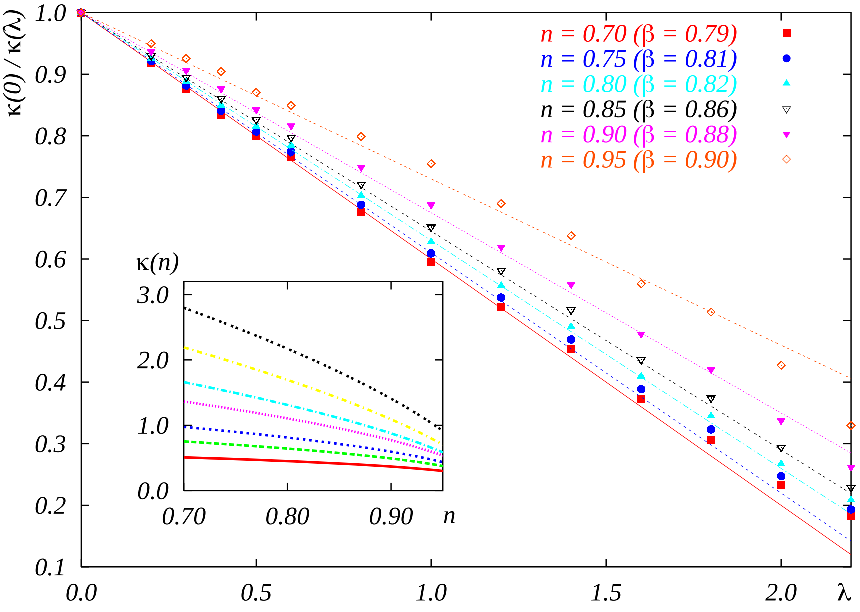

Figure 4.5: The points represent the normalized inverse compressibility $[\kappa(\lambda)/\kappa(0)]^{-1}$ as a function of λ at $U = 5D$ and for different densities, compared with the fit (depicted with lines) described in the text. Inset: Compressibility vs filling for various values of $\lambda = 0.0, 0.8, 1.2, 1.6, 1.8, 2.0, 2.2$ (from the bottom to the top).

of λ at $U = 5D$ for different values of the electron density, ranging from $n = 0.70$ to $n = 0.95$ (plotted with different points in the main panel of the figure). An enhancement of $\kappa(\lambda)/\kappa(0)$ that varies from almost 6 in the $n = 0.70$ case, to around 3 in the $n = 0.95$ case corresponds to the decreasing linear behavior of all the curves seen in the figure. We also calculated the values of the renormalization factor Z which is inversely proportional to the quasiparticle density of states (Z will be shown in Fig. 4.6). Since we found that Z varies much less than κ as a function of λ, such an enhancement of the compressibility cannot be due to mass renormalization alone. This also indicates that, within the Landau Fermi liquid approach, the total F_0^S is expected to be renormalized by the electron-phonon interaction like in the large$-N$ calculations.

Information on this renormalization of the Landau amplitudes can be extracted by simply assuming that a relation similar to Eq. (4.3) holds also for the DMFT solution. We therefore fitted the DMFT data with the relation

$$\frac{\kappa(\lambda)}{\kappa(0)} = \frac{1}{1-\beta\kappa(0)\lambda D}, \tag{4.5}$$

where β is the only fitting parameter. The results of this fit, together with the values of $\kappa(\lambda)$ in the inset, are shown in Fig. 4.5. For almost the whole range of densities the fit is extremely accurate up to $\lambda = 2.2$, with just a small correction to the ideal large-N result $\beta = 1$. The closer we get to half-filling the more β approaches 1, even if at $n = 0.95$ the strong-coupling data display some fluctuations. The values of β are reported in the figure.

We have therefore found that the simple Eq. (4.5) reproduces quite well the way the electron-phonon interaction modifies the charge compressibility in the strong correlated region of the Hubbard-Holstein model. This findings point therefore in the direction of the large$-N$ studies [72, 73], albeit these have found a divergent compressibility for relatively small values of λ. As we have said, the DMFT results indicate only a substantial enhancement. We attribute this discrepancy to the smaller value of the electronic F_0^S found in the large$-N$ with respect to the one found in the present DMFT approach.

4.3.2 quasiparticle weight

As we have seen in Chapter 3, the physics of the strongly correlated metallic phase of the Hubbard-Holstein model at half-filling is mostly characterized by the value of u, which, when it is bigger than the electron-phonon coupling λ, rules, at the same time, the width of the coherent metallic peak at the Fermi level and the position of the lower and upper Hubbard bands. Charge fluctuations are almost completely frozen for $n = 1$; every site is forced to be single-occupied, and this, as we have shown, suppresses largely the effects of the electron-phonon interaction. When the density departs from the value of 1, this is no longer true and the competition between u and λ becomes more “fair”. The electronic spectral density, as a consequence, is not symmetric and the (lower) Hubbard band is pushed towards the Fermi level so that it actually merges with the metallic peak. In other words, a clear separation between low and high energy does not exist for $n \neq 1$.

In the previous chapter we have seen that, as a result of the separation between low and high energy at half-filling, the spectral density of the Hubbard-Holstein solution is well reproduced by an effective Hubbard model with a slightly rescaled repulsion u_{eff}. The value of u_{eff} was determined by imposing that the full and the effective models have the same value of Z [2].

The necessary condition for the introduction of such an effective Hubbard model was that, close to the Mott transition at half-filling, the effect of λ on the quasiparticle weight is opposite to that of the Coulomb repulsion U: the former increases Z, while the latter decreases it. In other words, the electron-phonon interaction pushes the systems slightly away from the metal-insulator transition, if U is sufficiently close to U_{c2}.

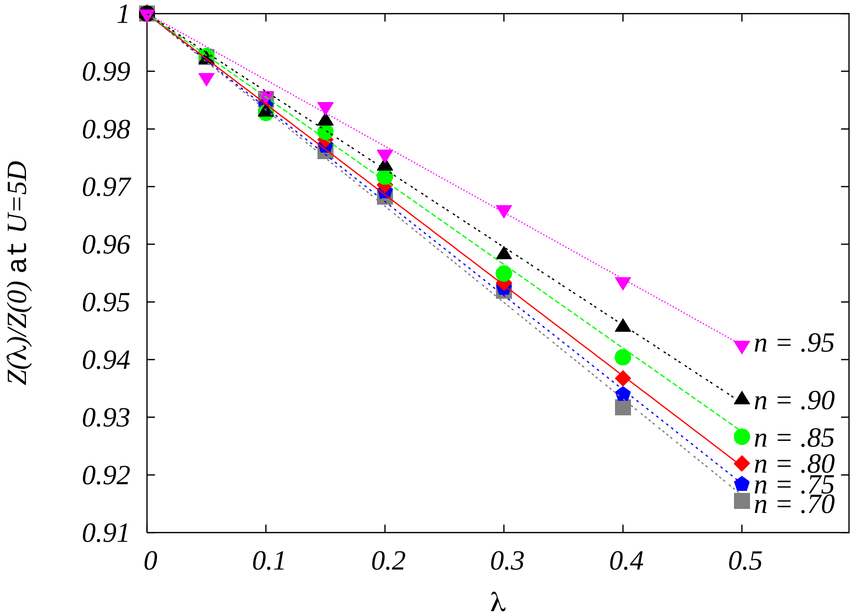

Figure 4.6: $Z(u=5,\lambda)/Z(u=5,\lambda=0)$ for various values of the density. The lines are the result of a linear fit, as described in the text.

As a matter of fact, for finite doping the electron-phonon interaction does not merely screen the Hubbard repulsion as in the half-filled case and does not give rise to the counterintuitive effect of reducing the effective mass. In fact we find that Z always decreases with λ, in the interval of densities between 0.7 and 0.95, as it can be seen in Fig. 4.6

where we show the calculated values for the quasiparticle weight as a function of λ for different densities, for fixed $U = 5D$ and $\omega_0 = 0.2D$. The various curves in the figure are normalized with $Z(\lambda = 0)$ at the corresponding density. We recall that, since we are working with $U > U_{c2}$, the metallic solution does not exist for $n = 1$, so that we find a nonzero quasiparticle weight only for $n \neq 1$.

We have calculated the quasiparticle weight also for larger λ, but in Fig. 4.6 we choose to report it only in the range between 0 and 0.5 to evidence the weak-coupling linear behavior of almost all the curves. A linear fit is in fact satisfactory, apart from a bit of noise displayed by the curves with the highest densities. The slope gets smaller with increasing density and, at the same time, the bare value of $Z(\lambda)$ decreases approaching half-filling (see the right hand panel of Fig. 4.7).

The effect of λ on Z is, in any case, small, compared to that of n. A strong dependence of the quasiparticle effective mass on the distance from half-filling, is in fact, observed in this region of the phase diagram. This can be seen in the right hand panel of Fig. 4.7 where the bare value of the effective mass for $U = 5D$ is plotted as a function of λ, for different values of the density. The small slope of the curves with different values of n and the fact that they are almost parallel to each other, indicate that the electron-phonon coupling λ has a strongly reduced effect on mass renormalization when U is large. The comparison with the left hand panel, where the same quantity is reported for $U = 0$, confirms this observation: in this case m^* first increases linearly with λ and then follows the well-known exponential behavior when the polaronic regime is reached ($\lambda_{pol} \approx 0.8$). On the contrary, we know that, for large values of U, the polaronic crossover is found for larger values of λ. The points of the right hand panel are still far from the polaronic regime and, as a consequence, increase slowly with λ.

Similar results have been found with a semi-analytic approach to coupled electron-phonon systems in the presence of correlation [106, 107]. In this approach, which is based on an expansion over the adiabatic regime, an effective low-frequency action is derived and then solved within DMFT. The effective electron-phonon coupling is found to be strongly suppressed in systems near the Mott transition, in the case of Holstein phonons [108].

The comparison between the two panels of Fig. 4.7 shows, as well, how the bare values of the effective mass are enhanced by more than one order of magnitude because of the strong repulsion. However if we push U to larger values, m^* saturates and almost does not increase any more. In other words, for such large values of U, m^* depends weakly on

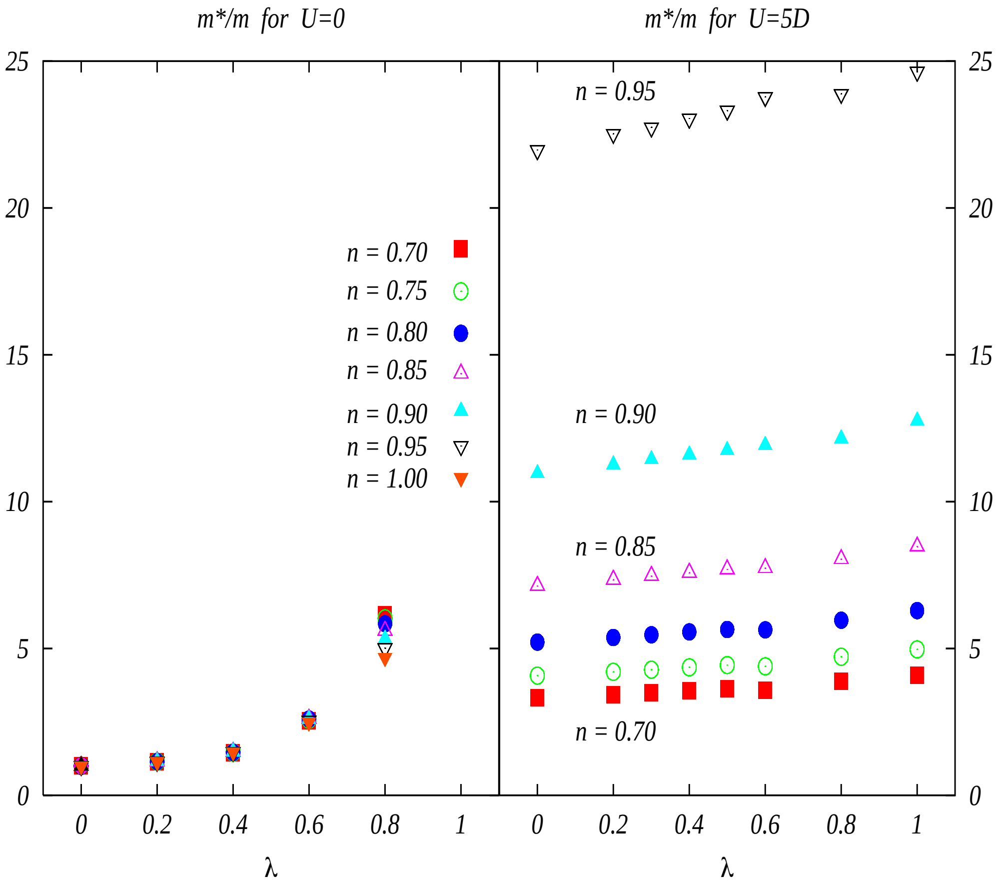

Figure 4.7: Calculated values of m^*/m as a function of λ for various values of the density. The left panel contains the results for $U = 0$ while in the right panel the data for $U = 5D$ are reported.

the value of the repulsion, while the biggest dependence is upon the doping δ.

Therefore, in this region of the phase diagram, both U and λ act in the same direction of giving mass to the quasiparticles, and an effective Hubbard model with simply a rescaled repulsion cannot be defined. A possible line of thought would be the following: At half-filling, the quasiparticle weight Z strongly depends on the difference $U - U_{c2}$. Now, for $U \gg U_{c2}$ and $n \neq 1$, we have seen that Z depends weakly on U, while the distance from the Mott transition is controlled by δ. Therefore, the role played by the repulsion in the half-filled case, could be now taken by the doping and, in analogy with the analysis at half-filling, two solutions with the same value of Z can be found by suitably varying δ.

Nevertheless, it turns out that the spectral densities of two solutions with the same value of Z, one for $\lambda = 0$ and the other for $\lambda \neq 0$, are not so similar one another, as it happens in the case of half-filling. This can be seen, for example, by looking at Figs. 4.8 and 4.9, where we show the spectral densities in the pure Hubbard model (Fig. 4.8) and in the Hubbard-Holstein for $\lambda = 1.8$ (Fig. 4.9). In both cases we fixed $U = 5D$, while the chemical potential has been varied in order to obtain, more or less, the same value of the quasiparticle weight $Z = 0.081$. Apart from the more pronounced effect of the electron-phonon coupling which shows up in the presence of phonon replica on sides

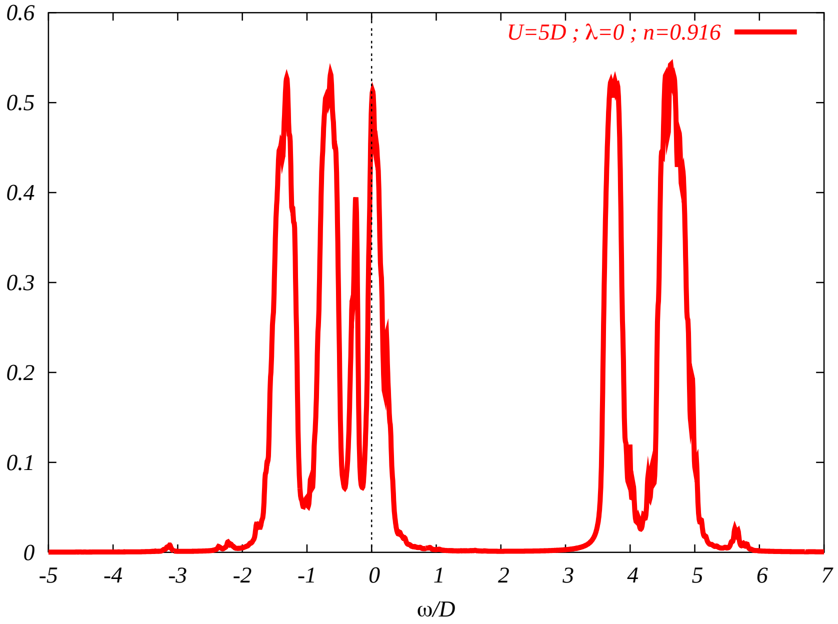

Figure 4.8: Spectral density for $u = 5$ and $\lambda = 0$. The density is equal to 0.916.

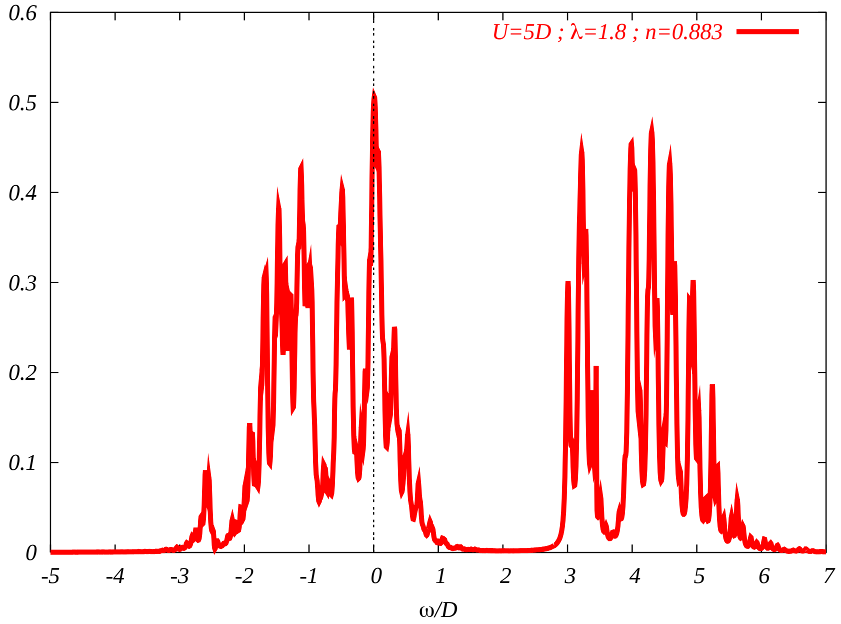

Figure 4.9: Spectral density for $u = 5$ and $\lambda = 1.8$. The density is equal to 0.883.

of the quasiparticle peak, the distance between the lower and the upper Hubbard bands is different in the two cases. In fact, while for $\lambda = 0$ the upper Hubbard band is placed at a distance of order U from the lower one, for $\lambda = 1.8$ this distance is reduced and part of the spectral weight is transferred to the left edge of the band. This is the main difference with the analysis at half-filling, where the same rescaling holds both for the low and for the high part of the spectrum.

With respect to the half-filled case therefore, the action of λ at finite doping can no longer be synthesized through a single effective quantity embodying the dynamical renormalization of U at low energy and the analysis of the influence of the electron-phonon coupling on quasiparticle properties is less transparent.

One can think that, because of finite doping, correlation should be in a sense, less crucial and a perturbative treatment of the electron-phonon interaction could be done starting from a renormalized Fermi liquid. To check this statement, we discuss, in the remaining of this section, a weak coupling approach to the interaction between quasiparticles and phonons and show that our DMFT results are in reasonable agreement with it.

We can separate two contributions to the self-energy and write the Green function as

$$G(\mathbf{k},\omega)^{-1} = \omega - \xi_{\mathbf{k}} - \Sigma_U(\mathbf{k},\omega) - \Sigma_{res}(\mathbf{k},\omega) \tag{4.6}$$

where Σ_{res} denotes the self-energy due to the additional interaction (all the bare and dressed electron-phonon processes) beyond the pure U. Expanding for small $\mathbf{k}$ and ω one has:

$$G(\mathbf{k},\omega) = \frac{Z_U}{\omega - \xi^{qp}_{\mathbf{k}} + i\gamma^{qp}_{\mathbf{k}} - Z_U \Sigma_{res}(\mathbf{k},\omega)} \tag{4.7}$$

where

$$Z_U^{-1} = 1 - \left.\frac{\partial \Sigma'_U(\mathbf{k},\omega)}{\partial \omega}\right|_{\omega=0} \tag{4.8}$$

This quantity is related to the full quasiparticle weight in the following way:

$$Z^{-1} = 1 - \left.\frac{\partial \Sigma'(\mathbf{k},\omega)}{\partial \omega}\right|_{\omega=0} = Z_U^{-1}\left(1 - Z_U \left.\frac{\partial \Sigma'_{res}(\mathbf{k},\omega)}{\partial \omega}\right|_{\omega=0}\right) \tag{4.9}$$

The wave-function renormalization, due to the additional interaction, for the quasiparticles created by U, is given by

$$\frac{Z}{Z_U} = \frac{1}{1 - Z_U \left.\frac{\partial \Sigma'_{res}(\mathbf{k},\omega)}{\partial \omega}\right|_{\omega=0}} \tag{4.10}$$

Now we extract the wave-function renormalization, due to the presence of the electron-phonon interaction. The quasiparticles are renormalized by the quantity Z/Z_U, given in Eq. (4.10), and we can apply the weak-coupling result to the quasiparticles: $Z_U \Sigma'_{res} \propto -\omega$. For this purpose one needs the quasiparticle density of states, which is equal to $N(E_F)/Z$, as well as the expression for the interaction. This latter quantity brings in a factor Z^2. In the specific case: $Z_U^2 \lambda$. In the evaluation of the self-energy for the quasiparticle ($Z_U \Sigma'_{res}$) we have to take into account the density vertex with the phonon dressed by all the possible electronic processes. In the self-energy diagram with one phonon line, we have two density vertices denoted by Λ, containing one fermionic bubble each [109]. We can thus go on as in the case of free-particles [23]. The last thing to remember is to multiply the result by $1/Z_U$, because of the quasiparticle density of states. In this way we obtain our result:

$$Z_U \Sigma'_{res} = -\left(\frac{1}{Z_U} N(E_F) Z_U^2 \Lambda^2 \lambda D\right)\omega \tag{4.11}$$

We can obtain an explicit expression for the density vertex Λ only in two specific cases: the static and the dynamic limit. In fact, two Ward Identities can be used for this purpose

[109]:

$$Z_U \Lambda(q \to 0, \omega = 0) = \frac{1}{1 + F_0^{s(e)}} \tag{4.12}$$

and

$$Z_U \Lambda(q = 0, \omega \to 0) = 1 \tag{4.13}$$

Because we are considering electronic processes only, we have, in the static limit

$$\Lambda = \frac{\kappa^{(e)}}{\kappa_0^{(e)}} \tag{4.14}$$

where $\kappa^{(e)}$ is the compressibility of the Fermi liquid in the absence of coupling with the lattice, while $\kappa_0^{(e)}$ is the non-interacting value $2N(E_F)$. Then Eq. (4.11) can be written, in the static limit, as

$$Z_U \Sigma'_{res} = -\left(N(E_F) Z_U \left[\frac{\kappa^{(e)}}{\kappa_0^{(e)}} \right]^2 \lambda D \right) \omega \tag{4.15}$$

In the opposite dynamic limit, instead:

$$\Lambda = \frac{1}{Z_U} \tag{4.16}$$

and Eq. (4.11) becomes

$$Z_U \Sigma'_{res} = -\left(\frac{N(E_F)}{Z_U} \lambda D \right) \omega \tag{4.17}$$

Using Eq. (4.10), the wave-function renormalization for quasiparticles becomes

$$Z^{qp} = \frac{Z}{Z_U} = \frac{1}{1 + \bar{\alpha}\lambda D} \simeq 1 - \bar{\alpha}\lambda D \tag{4.18}$$

If the "residual" part of the self-energy, Σ_{res}, is really due to electron-phonon processes only, one can approximate $\bar{\alpha}$ with $Z_U \Lambda^2 N(E_F)$, as long as one considers those self-energy diagrams in which the correlation dresses exclusively the vertex. However it is important to recall that there are other diagrams which cannot written in terms of vertex correction that can contribute giving a different result for the wave-function renormalization of the quasiparticles.

Working at $U/D = 5$, we have calculated Z with DMFT (see Fig. 4.6), and extracted the coefficient $\bar{\alpha}$ which appears in Eq. (4.18) from a linear fit of the quantity Z/Z_U for small λ. The results of the fit are shown, as well, in Fig. 4.6, while the behavior of $\bar{\alpha}$ as a function of the density is reported in Fig. 4.10 with solid red squares. In our DMFT results all the possible contributions to the electronic self-energy are considered, so it is interesting to compare them to the outcome of the perturbative approach. We have seen that, if the two density vertices in the self-energy are taken in their static limits,

$$\bar{\alpha} = N(E_F) Z_U \left[\frac{\kappa^{(e)}}{\kappa_0^{(e)}} \right]^2 \tag{4.19}$$

while, if they are considered in the opposite dynamic limits,

$$\bar{\alpha} = \frac{N(E_F)}{Z_U} \tag{4.20}$$

The behavior obtained in the dynamic limit is completely different from what it is found with DMFT, since the coefficient $1/Z_U$ diverges when the density n approaches 1, while the DMFT points stay finite. The values for $\bar{\alpha}$ obtained with Eq. (4.20) lays outside the range of Fig. 4.10. The static result of Eq. (4.19) is instead depicted in Fig. 4.10. It has been evaluated using the values of the quasiparticle weight Z_U and of the compressibility $\kappa^{(e)}$, calculated in the absence of electron-phonon coupling. This prediction is less inconsistent with the DMFT data compared to the dynamic limit, but, in any case, it largely underestimates the DMFT result and, differently from that, it is vanishing small approaching half-filling.

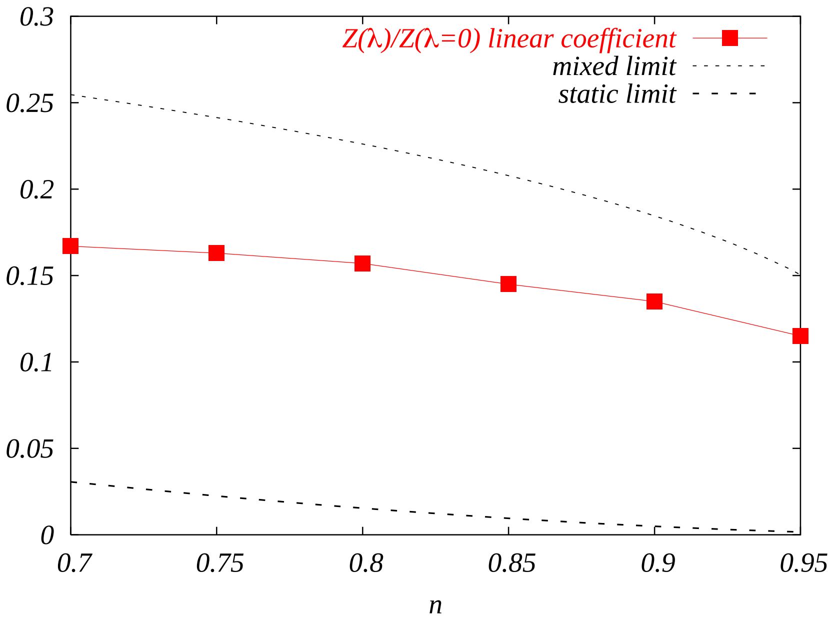

Figure 4.10: linear coefficient of Z for various values of the density.

The results of the fit on the DMFT data are instead closer to a combination of the static and the dynamic limits, reported in Fig. 4.10 with the label “mixed limit”. This is obtained by considering one of the two density vertices in the static limit and the other one in the dynamic limit. As a consequence we have to consider, in Eq. (4.11), for one of the two vertices, $Z_U\Lambda = 1$, while, for the other, $Z_U\Lambda = 1/(1+F_0^{s(e)})$, obtaining the following result

$$\bar{\alpha} = N(E_F)\frac{\kappa^{(e)}}{\kappa_0^{(e)}} = \frac{\kappa^{(e)}}{2} \tag{4.21}$$

The agreement between the fit on the DMFT data and the “mixed limit” curve is quite remarkable. Both curves stay finite and have almost the same behavior approaching half-filling, whereas the static limit goes to zero and the dynamic one diverges.

We argue that the “mixed limit” solution gives a good description of the DMFT result because it represents a geometrical average between the static and the dynamic limit. The local density vertex entering the expression of the DMFT self-energy, experiences a dramatic variation since it assumes values which ranges between the two limits, which are enormously different one another. Plausibly, the result of the compensation between these two limits, can be well approximated by an arithmetical average between the logarithms of the static and the dynamic vertices, which is equivalent to take the geometrical average

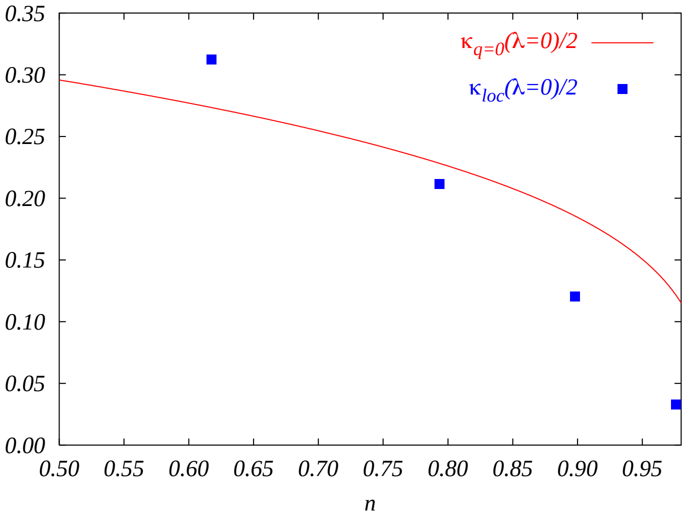

Figure 4.11: Comparison between $\kappa_{q=0}(\lambda = 0)$ and $\kappa_{loc}(\lambda = 0)$ as a function of the density. Note that the red solid curve is the same as the “mixed-limit” one of Fig. 4.10.

between the vertices themselves.

As a last attempt we have also tried to use, in Eq. (4.21), the *local* compressibility, instead of the *uniform* ($q = 0$) one, extracted directly from the derivative of n with respect to μ. The curve for $\bar{\alpha}$ evaluated using the local compressibility should be more consistent with the result for the quasiparticle weight Z, extracted from the DMFT self-energy. In Fig. 4.11 the behavior of $\bar{\alpha}$ in the "mixed limit", Eq. (4.21), is shown using κ_{loc}. The result is similar to $\kappa_{q=0}$, but κ_{loc} bends down more pronouncedly towards zero approaching half-filling.

Chapter 5

Finite temperature study of the pure Holstein case

5.1 Retardation effects on localization transitions in attractive and repulsive models

In the previous chapters we have extensively analyzed the metal-insulator transition in the Hubbard model and the effect of the electron-phonon interaction on it. We have seen that, at the basis of this phenomenon there is the competition between the kinetic and the repulsive term. If the repulsion is sufficiently large, the “localizing power” of U prevails, at half-filling, over the tendency towards delocalization due to the hopping term, leading to a Mott insulating phase made of localized spin 1/2 electrons. Usually this phase is referred to as a localized moment phase. Within the Hubbard model, this localization transition has been studied with DMFT both at zero and finite temperature, evidencing how the free energies of the metallic and the insulating phase cross along a line which ends in a second-order critical point at a temperature around 1/50 of the bandwidth (see Sec. 2.2.1). Above the critical point, a crossover between an insulating- and a metallic-like regime has been identified [47]. The whole high-temperature region is characterized by a smooth behavior of the free energy as a function of U, and the metallic and the insulating phases are no longer clearcut distinguishable, due to the unavoidable presence, even for large values of U, of spectral weight at the Fermi level. Nevertheless, the crossover can be characterized by the evolution of local moments. These, in fact, are formed by increasing U, even if T is large. Therefore, a border between the two regimes exists, but it is not easy to find and to draw in a phase diagram.

These considerations can be reformulated in the context of an attractive Hubbard model. In fact, it is known that the repulsive Hubbard model can be mapped onto an attractive Hubbard one in a bipartite lattice [110]. The mapping is realized through a particle-hole transformation on the down spins $c_{i\downarrow} \rightarrow (-1)^i c_{i\downarrow}^\dagger$. The repulsive model with a finite density n is transformed into a half-filled attractive model with a finite magnetization $m = n - 1$ and the chemical potential is transformed into a magnetic field $h = \mu$. In the $n = 1$ case (half-filling) the two models are therefore completely equivalent. We notice that the above mapping does not only hold for the normal phases, but extends to the broken symmetry solutions. The three components of the antiferromagnetic order parameter of the repulsive Hubbard model are in fact mapped onto a staggered charge-density-wave parameter (z component of the spin) and an s-wave superconducting order parameter ($x - y$ components). Therefore, the magnetic moment formation in the repulsive Hubbard model corresponds to the transition to the incoherent pair phase in the attractive model, as we have also briefly mentioned in Sec. 3.1.2 [87].

In this Chapter we are interested in studying how incoherent pair formation is modified by the inclusion of retardation. This can be naturally done within the Holstein model in which the Hubbard term is replaced by the electron-electron retarded interaction mediated by an Einstein phonon, which plays the role of a bosonic mediator with a characteristic frequency ω_0.

In fact, the attractive Hubbard model can be viewed as the antiadiabatic limit (done by letting $\omega_0 \rightarrow \infty$, keeping the electron-phonon coupling λ finite) of the Holstein model, as we have already discussed in Chapter 2 (see Sec.2.1.2 and 2.2.2). When the phonon frequency is the largest energy scale, the interaction between the electrons mediated by the phonons

$$V_{el-ph}(\omega) = -\frac{g^2\omega_0}{\omega_0^2 - \omega^2} = -\frac{\lambda D}{2}\frac{\omega_0^2}{\omega_0^2 - \omega^2}, \tag{2.4}$$

becomes instantaneous and the final result is a static attraction, of strength $\lambda D = 2g^2/\omega_0$, between electrons with opposite spin. Away from this specific limit, the Holstein model configures, therefore, as an ideal playground for the study of retardation effects on incoherent pair formation.

The introduction of the phononic degrees of freedom implies that also lattice polarization comes into the game, when ω_0 is finite. Our main concern will be, therefore, to define an appropriate method to determine the temperatures at which incoherent pairs start to form and at which the lattice starts to be polarized, and to study the effect of retardation on both phenomena. We will carry out this finite temperature study with

DMFT and using QMC as impurity solver (see Sec. 2.3.2). Consequently, we can reliably analyze the intermediate-to-large temperature range. In particular, we stay always above the critical temperature for the metal-insulator transition displayed by the antiadiabatic Holstein model (the attractive Hubbard one) at half-filling.

We already know some of the properties of the Holstein model at zero temperature, from the DMFT study of the previous chapters. In particular, we have discussed the differences between the antiadiabatic and the adiabatic regimes, as far as lattice polarization and behavior of coherent quasiparticle excitations are concerned. The phase diagram of the Holstein model, calculated in Ref. [3], has been reported in Fig. 2.5. We recall the main outcomes: In the antiadiabatic regime, we have the physics of the negative Hubbard model and the width of the quasiparticle peak vanishes for a critical value of λ equal to U_{c2}/D. This marks the transition to the incoherent pair phase. Lattice polarization, instead, cannot be induced for finite λ. In the opposite adiabatic regime, i.e. for small values of $\gamma = \omega_0/D$, polaron formation is first encountered by increasing λ and the quasiparticle weight Z goes to zero for slightly larger values, signaling the transition to the bipolaronic state. In this case, the incoherent pairs are associated to lattice polarization (bipolarons), contrary to the large-γ regime. The aim of the present chapter is therefore to extend at finite temperatures this kind of analysis on the half-filled Holstein model.

The inclusion of retardation on the negative-U Hubbard model is considered of great interest for its implications in the attractive physics (BCS-Bose Einstein crossover, preformed pair scenario, and so on). Nevertheless, thanks to the mapping between the attractive and the repulsive Hubbard model, this study directly addresses the crucial question of how local moment formation is influenced by the presence of retardation in the repulsive model. The spectral properties are expected to be modified as well by the inclusion of retardation. In a recent DMFT study on the Hubbard model, a transfer of spectral weight from high to low energy has been observed at high temperatures [111]. The Mott gap, in any case, does not close with increasing temperature. Abandoning the instantaneous picture of the Hubbard model, one expects to observe additional non-trivial temperature dependences. Namely, the interaction itself, which now contains a finite characteristic frequency scale, is expected to be modified when the temperature reaches this scale, inducing more dramatic effects on the spectral density.

In conclusion the present study of the Holstein model will shed light, indirectly, on an apparent unrelated phenomenon like the formation of localized moments at high temperature in the repulsive Hubbard model in the presence of retardation, which constitutes the main motivation for this chapter.

5.2 Pairing and polarization as a function of temperature

The distinction between the metallic- and the insulating-like phase is more difficult to establish at finite temperature than in the zero temperature case, because of the presence of spectral weight at the Fermi level. We have recalled that this problem is encountered in the characterization of the Mott transition in the Hubbard model at finite temperature, and that, at half filling the same results hold for negative U, with the incoherent pairs playing the role of localized magnetic moments. Also in this case the characterization of different regimes rather than different phases, still pose the serious problem to define a suitable quantity that is able to distinguish clearly the different regions in the phase diagram.

When the presence of a finite intrinsic scale ω_0 for the phonon dynamics is considered, the scenario is enriched by the possibility of inducing of lattice polarization. As we have seen, in fact, the presence of retardation allows to define an adiabatic regime in which electronic degrees of freedom are faster than bosonic ones. In this regime the crossover from quasi-free electrons to almost localized polarons can be unambiguously defined by looking at the polarization properties of the phonon field [92, 88]. As we have extensively discussed for the zero temperature case, the polaron crossover is signaled by the development of a bimodal characteristic in the probability distribution function $P(X)$. In the formalism of QMC, which is the technique we use in this finite temperature DMFT study (see Sec. 2.3.2), $P(X)$ can be defined as the probability distribution of the endpoint of the phonon path in imaginary time

$$P(X) = \langle \delta(X - x(0)) \rangle \tag{5.1}$$

The phonon also mediates an attractive interaction which can be strong as well, and produce pairing. As we will see in the following, we are able to disentangle this process from polarization in the normal phase and define unambiguously also the pairing crossover. The quantity which we can monitor, in fact, is, in this case, the distribution function of the center of mass ("centroid") of the phonon path[1]

$$P(X_c) = \left\langle \delta(X_c - \frac{1}{\beta}\int_0^\beta x(\tau)d\tau)\right\rangle \tag{5.2}$$

In both the definitions, the averages are done with the action given in Eqs. 2.31-2.33 (see Sec. 2.3.2).

In fact, if polaron formation can be inspected by looking at $P(X)$, which is the probability distribution of the polarization field [88], the formation of local pairs is associated to the development of a multi-modal characteristic in $P(X_c)$ (this statement is demonstrated in the specific case of the antiadiabatic atomic limit of the Holstein model, in Appendix B). The possibility of disentangling pairing and polarization is extremely useful because the larger is the characteristic frequency ω_0, the more the two things are different one another, opening an interesting regime in between. Moreover this allows us to draw, both for small and large frequencies ω_0, two well-defined lines for all temperatures ($\lambda_{pair}(T)$ and $\lambda_{pol}(T)$), whereas many other quantities vary smoothly and change behavior too gradually to identify a precise point to place the crossover. It is customary to look, alternatively, at maxima or minima in some physical quantities, like specific heat or a susceptibility, but in that case the connection with local pair formation is more difficult to demonstrate.

A simple argument to understand the relevance of our criterion can be derived by considering directly the interaction term (2.33) in the action: $-g' \int_0^\beta d\tau x(\tau)n(\tau)$. In the adiabatic limit ($\omega_0 \to 0$, $M \to \infty$, λ finite) the kinetic term of the action enforces the boson path to be τ-independent. The boson field becomes a classical field and the interaction term can be written as $-g'X \int_0^\beta d\tau n(\tau)$, where X indicates the common value assumed by all the $x(\tau)$ along the imaginary time path. In this limit the centroid coordinate X_c is equal to X and the two distributions $P(X)$ and $P(X_c)$ are the same. In this sense, in the classical limit, both the endpoint and the centroid collapse into the classical position of the particle.

In the antiadiabatic limit ($\omega_0 \to \infty$, $M \to 0$, λ finite) the kinetic term in the bosonic action disappears, the boson becomes an Hubbard-Stratonovich field which is coupled to the z-component of the pseudo-spin [87]. In this case the Holstein model maps onto the negative-U Hubbard model. The Hubbard-Stratonovich field is the one which decouple the quartic Hubbard term. It is useful to exploit analytically the properties of $P(X_c)$ and

---

[1] Notice that the centroid of a particle has the physical meaning of the classical position of the particle itself.

$P(X)$ in the atomic $D = 0$ limit in which electron density becomes a constant of motion (see Appendix B). The interaction term (2.33) takes the transparent form $-g'n \int_0^\beta d\tau x(\tau)$ where the electron density is directly coupled to the centroid of the Hubbard-Stratonovich field. As we have shown in Appendix B, the average appearing in Eq. (5.2) can be more easily carried out in the occupation number basis giving a probability distribution function which becomes bimodal for temperatures below the activation temperature of the double occupancies ($T < g'^2/2M\omega_0^2$). We thus associate bimodality of $P(X_c)$ to pair formation. We remark that all the conclusions drawn in this limit for the attractive Hubbard can be recast for the repulsive model upon substituting the pseudo-spin with magnetization. Therefore in this case the bimodality of $P(X_c)$ can be associated to the formation of local magnetic moments. In the same limit it can be checked that the endpoint distribution $P(X)$ has infinite variance and as a consequence no definite polarization as well as no polaronic phase exists any more (see Appendix B).

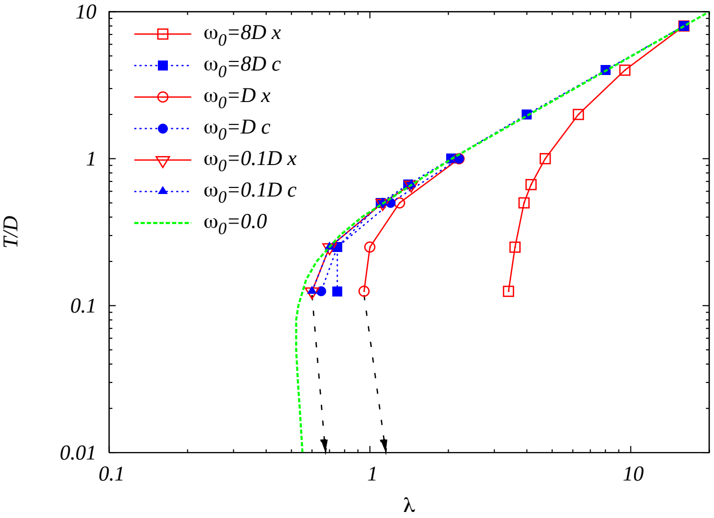

Figure 5.1: Behavior of $\lambda_{pair}(T)$ (in blue and with the letter c) and $\lambda_{pol}(T)$ (in red and with the letter x) at $\omega_0 = 0.1D$, D and $8D$, respectively indicated by solid and open triangles, solid and open circles and solid and open squares. The green dashed line represents the $\omega_0 = 0$ result for both $\lambda_{pair}(T)$ and $\lambda_{pol}(T)$. The dashed arrows indicates the zero-temperature results for the polaron crossover at the various values of ω_0 [3].

To analyze the evolution of $P(X)$ and $P(X_c)$ at finite D and ω_0 we calculate both of them with QMC. Before discussing the results, we note that the explicit form derived for $P(X_c)$ in the atomic limit and for $\omega_0 = \infty$ (see Eq. B.24 of Appendix B), coincides with that of $P(X)$ for $\omega_0 = 0$, still in the atomic limit [88]. Since for $\omega_0 = 0$, the endpoint and centroid distributions are the same, this means that in the atomic limit $P(X_c)$ is the same for $\omega_0 = 0$ and $\omega_0 = \infty$. By looking at Fig. 5.1, it is clear that $P(X)$ and $P(X_c)$ have the same behavior already for $\omega_0 = 0.1D$, while they differ for $\omega_0 = D$ and $8D$. In these cases, in fact, for temperatures less than ω_0, λ_{pol} is shifted towards strong couplings. On the other hand the line where $P(X_c)$ becomes bimodal is only slightly shifted for larger couplings with increasing ω_0. This is strongly suggesting of the behavior of the bipolaronic transition in the Holstein model at zero temperature, whose critical coupling is slowly increasing with ω_0 and then saturates to the asymptotic $\omega_0 = \infty$ value [3]. On the other hand, the polaron crossover is more or less directly proportional to ω_0 [3].

Both at zero and at finite temperature the line where the centroid becomes bimodal does not coincide with the bipolaronic transition line, obtained looking at the condition $Z = 0$, but it can be considered a precursor which depends in a very similar way on ω_0 and on λ.

Our DMFT results can also be compared with the semi-analytical results for $\omega_0 = 0$ [88], which is represented by the green dashed line in Fig. 5.1. It can be seen that the $\omega_0 = 0.1D$ case is in very good agreement with the adiabatic result, and also the $\omega_0 = D$ and $8D$ cases, at high temperature, fall on the same curve. It must be observed also that, in the full DMFT calculation, the centroid distribution depends weakly on ω_0, as suggested by the atomic limit.

Interestingly the green dashed line displays a re-entrance at low temperatures. Although the QMC simulations cannot reach sufficiently low temperatures, we find that the re-entrance is present also for ω_0 different from zero, as indicated by the arrows in Fig. 5.1, which point to the zero temperatures results for the polaron crossover of the zero-temperature DMFT calculation for the Holstein model [3]. This phenomenon has been also reported for the metal-insulator transition in the positive-U Hubbard model [81, 82], here, by analogy, we can speculate about a pseudo-spin entropy contribution which adds to the free energy of the insulator after temperature increase leading to the stabilization of the insulating phase. In a recent study of the two-site Holstein model, the re-entrant curve for the polaronic crossover has been observed [112].

Another important difference between the development of a bimodal character in the centroid and in the endpoint distributions is the behavior of the double occupancies $\langle n_\uparrow n_\downarrow \rangle$. This quantity is equal to 1/4 in the non interacting case and approaches, with different slopes depending on the value of ω_0 and of the temperature T, the asymptotic value of $1/2$ for strong couplings.

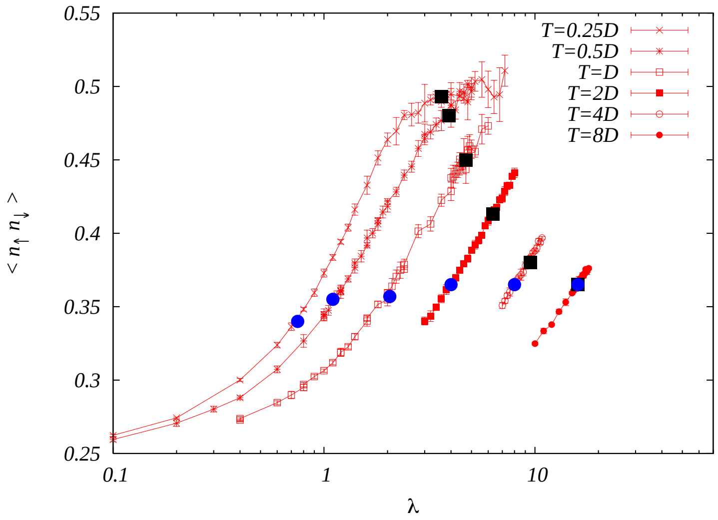

Figure 5.2: Double occupancies for different temperatures at $\omega_0 = 8D$. The blue solid circle (black solid square) denotes the coupling where $P(X_c)$ ($P(X)$) develops the bimodal character.

In Fig. 5.2 we have plotted the double occupancies for different temperatures at $\omega_0 = 8D$, which is representative of the antiadiabatic limit [2]. In this limit λ_{pol} is much bigger than λ_{pair} for temperatures lower than ω_0, so we can clearly see the difference between the double occupancies at λ_{pol} and at λ_{pair}. In Fig. 5.2 these two values are denoted, respectively, by a black solid square and a blue solid circle, for each temperature. $\langle n_\uparrow n_\downarrow \rangle$ calculated at λ_{pol} is rapidly increases with decreasing temperature, while $\langle n_\uparrow n_\downarrow \rangle$ calculated at λ_{pair} is almost constant with temperature, or rather is even slightly decreasing at low temperatures. So, when the centroid distribution becomes multi-modal, the double occupancies are approximately 70% of the saturation value of $1/2$ as suggested by the atomic limit result, which shows that the double occupancies activate at λ_{pair}. A similar result is found also for $\omega_0 = D$ and $0.1D$, with the only difference that the bifurcation in the double occupancies is less pronounced, since λ_{pol} is closer to λ_{pair}.

---

[2] Notice that exactly the same curves have been found in the attractive Hubbard model, at half-filling with exact diagonalization - Alessandro Toschi, private communication and [113]

5.3 Phase diagram of the Holstein model

In light of these results we draw in Fig. 5.3 a schematic phase diagram for the Holstein model where three regions can be identified: normal, pairs and bipolarons.

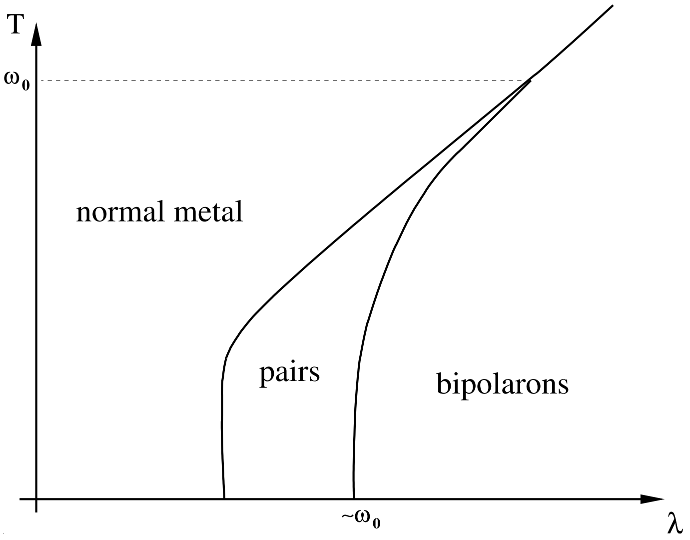

Figure 5.3: Schematic phase diagram for the Holstein model in the antiadiabatic regime. λ_{pair} is the curve separating the "normal metal" from the "pair" region and λ_{pol} the "pair" from the "bipolarons" region.

These three phases are delimited by two clearcut lines where the probability distributions for the centroid and for the endpoint of the phononic path, develop a bimodal shape. While the border between pair and the bipolaronic phase, given by λ_{pol}, is shifted to the right with increasing ω_0, the λ_{pair} curve between the normal and the local pair phase is weakly dependent on the ω_0. For finite values of ω_0, λ_{pair} and λ_{pol} merge for temperatures of the order of ω_0. In the antiadiabatic limit, therefore, λ_{pair} will be more or less in the same position of the blue curve with empty squares of Fig. 5.1, calculated for $\omega_0 = 8D$, while the bipolaronic regime will no longer exist. This is in agreement with other studies, carried out directly on the antiadiabatic limit. The behavior of λ_{pair} is, in fact, similar to that displayed by the T^* curve in a three-dimensional study of the attractive Hubbard model with QMC [114], found by looking at the maximum of the spin susceptibility. Moreover, the λ_{pair} curve closely resembles T^* extracted in a recent DMFT study [113] from the spin susceptibility and from the evolution of the broad peak in the specific heat. Also the reentrant behavior of the centroid curve, found in the adiabatic limit and which we expects to extend also for finite ω_0, is remarkably reproduced by the T^* line of Ref. [113].

Our analysis has determined, therefore, that in the presence of retardation, the region of incoherent pairs gets narrow and shrinks with increasing temperature. Approaching the attractive Hubbard limit, i.e. increasing ω_0, the pair phase region becomes gradually larger. Nevertheless, even in the absence of retardation, the incoherent pair region does not extend to arbitrarily large temperatures since λ_{pair} bends for large values of T, to reach the asymptotic line $T/D = \lambda/2$. Starting from a point inside the phase with incoherent pairs, these are rapidly destroyed by raising T and the “normal metal” region is reached.

In this work we do not present the results of a study on the real axis of the Monte Carlo data, which, at the moment, is underway. This further investigation aims at analyzing the evolution with temperature of the spectral function evidencing also the effect of retardation. Such a study would be of great interest and it is a necessary step in the comprehension of the high temperature physics of all those models which display a localization transition by increasing the strength of the interaction. In particular DMFT studies on the attractive Hubbard model [113] have evidenced that, starting from the pair phase at low temperature, the gap in the spectral function partially fills in when the temperatures is raised (of the order of some fraction of U). Finite dimensional QMC studies on the same model indicate a more pronounced effect of the temperature on the spectral density, which assumes, at high temperatures, the shape of a single broad peak [115, 116]. The problem of the spectral properties for large values of T, has been also attacked from the side of the repulsive Hubbard model. In a recent DMFT investigation [111], as we have already mentioned, a partial filling of the Mott gap has been found. Therefore, already in the absence of retardation, the evolution with the temperature of the spectral function in the pair phase is in clear contrast to the phenomenology of a band insulator, in which the temperature modifies only the occupation of the bands, without adding spectral weight inside the gap.

Conclusions

In this work the interplay between the electron-phonon interaction and strong correlation is analyzed with a non-perturbative approach. Dynamical Mean Field Theory is used, in fact, to solve the Hubbard-Holstein model, focusing on the strongly correlated regime both at half-filling and for finite values of the doping in the normal phase.

We have found that the properties of a local Holstein electron-phonon interaction are deeply modified when a strong electronic repulsion is present in the system. In general, the ability of eventually leading to polaronic effects is substantially depressed by a large Coulomb repulsion which freezes charge fluctuations so that the phonon-induced effective mass enhancement is also strongly reduced. One could be tempted to conclude that a Holstein electron-phonon interaction has almost no effect when the Hubbard repulsion U is large, but this is not the case, as we have shown in Chapter 3 and in Chapter 4. We have, in fact, detailed that the electron-phonon interaction is able to modify the phase diagram of a strongly correlated system and we have shown that the interplay between a strong electron-electron repulsion and a moderate electron-phonon attraction leads to highly non-trivial effects.

In the half-filling case, where the correlated system displays a clear separation between high and low energy physics, we have found that the effect of the electron-phonon interaction on the metallic system can be synthesized through a renormalization of the static Hubbard repulsion $U \rightarrow U - \eta\lambda D$, ruled by the parameter

$$\eta = \frac{2\omega_0/U}{1 + 2\omega_0/U}$$

which only involves the ratio between the phonon frequency ω_0 and the electronic repulsion U. We have understood the meaning of this result in terms of the Kondo physics underlying the Mott-Hubbard transition in DMFT. When U is larger than ω_0, the Kondo spin-flips associated to the formation of the coherent metallic peak at the Fermi level, are *rare* but *fast* processes, during which the phonons have no time to react. Only a small fraction

$\eta \simeq 2\omega_0/U$ of the total electron-phonon coupling λ therefore subtracts to the Hubbard repulsion, in this limit. The lack of time for phonons to rearrange during the quasiparticle processes determines the absence of phononic fingerprints in the low energy spectrum for the Hubbard-Holstein model, which is perfectly reproduced by the effective Hubbard model with rescaled repulsion $U - \eta\lambda D$.

The small screening effect of the electron-phonon interaction on the correlated half-filled metallic phase has dramatic consequences on quantities which strongly depend on the distance from the metal-insulator transition. One of these is the quasiparticle effective mass, which experiences a tremendous change if the effective U is changed, even of a small amount close to the metal-insulator transition. This results in a substantial dependence of m^* on the phonon frequency, since this is contained in the parameter η entering the expression for the effective repulsion. The isotope coefficient for m^*, in fact, is found to be inversely proportional to Z.

The parameter η contains also another crucial information: it says when the antiadiabatic limit is reached, in the presence of repulsion. In fact, in the antiadiabatic limit, the Hubbard-Holstein model becomes an Hubbard model with the strength of the interaction given by $U - \lambda D$, i.e. $\eta = 1$. The behavior of η evidenced by our DMFT analysis indicates therefore, that the antiadiabatic limit is recovered when ω_0 is larger than U, no matter how large is the value of the bare adiabatic parameter $\gamma = \omega_0/D$.

For finite values of the doping, low and high energies are no longer separable and the effect of the electron-phonon interaction cannot be described as a simple screening of the repulsion. The introduction of sensible effective parameters is less transparent, in this case, and the results of the interplay between the electron-phonon and strong correlation become harder to predict. Nevertheless, helped by the DMFT, we have been able to evidence the ability of the electron-phonon interaction of changing the order of the density-driven Mott transition, when a sizable Coulomb repulsion is present in the system. This effect determines a phase separation instability, which occurs between the Mott insulating phase with $n = 1$ and the correlated metallic one, with a finite value of the doping. Despite the sizable values of the electron-phonon coupling needed to observe the instability, the large values of U prevent the metallic system from displaying polaronic features. Quite remarkably, these are instead visible within the insulating phase, provided that its average number of particle slightly deviates from 1. Polaron distortions are visible, therefore, within the localized phase, albeit the values of the Hubbard repulsion used reach five times the bandwidth.

In the last chapter, we have worked on the half-filled Holstein model at finite temperature, in order to analyze the role of retardation on the localization transition displayed by the attractive Hubbard model as well as by the repulsive one. The mapping between the attractive and the repulsive Hubbard model, in fact, permits, in both cases, to introduce retardation effects through the Holstein model, in which an Einstein phonon of characteristic frequency ω_0 mediates the interaction between the electrons. We have found a criterion, valid at all temperatures, to determine unambiguously the crossover to the incoherent pair regime and the crossover to the regime in which lattice polarization is also present.

Appendix A

Kondo coupling in the presence of the electron-phonon interaction

The expression for the Kondo and for the antiferromagnetic couplings in the presence of phonons are calculated, perturbatively in $1/U$, respectively in Ref. [96, 97] and in Ref. [98]. The two calculations are carried out in different contexts, but they both come to the same result:

$$J_{PT}(t, \alpha^2, \lambda, U) = \frac{4t^2}{U} \mathrm{e}^{-2\alpha^2} \sum_{l=0}^{\infty} \frac{(2\alpha^2)^l}{l!(1 - \frac{\lambda D}{U} + \frac{\omega_0}{U} l)} \tag{A.1}$$

where $\alpha^2 = \lambda D/2\omega_0$, accordingly to the standard definitions of the parameters of the Hubbard-Holstein model, given in Sec. 2.1.

We want to expand this expression in power of $\frac{\lambda D}{U}$ and $\frac{\omega_0}{U}$. For this purpose, we introduce the function $f(\alpha^2, \lambda, U)$, given by

$$f(\alpha^2, \lambda, U) = \frac{U}{4t^2} \mathrm{e}^{2\alpha^2} J_{PT} = \sum_{l=0}^{\infty} \frac{(2\alpha^2)^l}{l!(1 - \frac{\lambda D}{U} + \frac{\omega_0}{U} l)} = \frac{1}{1 - \frac{\lambda D}{U}} \sum_{l=0}^{\infty} \frac{(2\alpha^2)^l}{l!} \frac{1}{1 + a\frac{\omega_0}{U} l} \tag{A.2}$$

where $a = \frac{1}{1 - \frac{\lambda D}{U}}$.

Now,

$$\frac{1}{1 + a\frac{\omega_0}{U} l} = 1 - a\frac{\omega_0}{U} l + (a\frac{\omega_0}{U} l)^2 - (a\frac{\omega_0}{U} l)^3 + ... \tag{A.3}$$

and then

$$\begin{aligned} f(\alpha^2, \lambda, U) &= \frac{1}{1 - \frac{\lambda D}{U}} \sum_{l=0}^{\infty} \frac{(2\alpha^2)^l}{l!} \left(1 - a\frac{\omega_0}{U} l + (a\frac{\omega_0}{U} l)^2 - (a\frac{\omega_0}{U} l)^3 + ...\right) \\ &= \frac{1}{1 - \frac{\lambda D}{U}} \left(\sum_{l=0}^{\infty} \frac{(2\alpha^2)^l}{l!} - a\frac{\omega_0}{U} \sum_{l=0}^{\infty} \frac{(2\alpha^2)^l}{l!} l + \right. \end{aligned}$$

$$+a^2(\frac{\omega_0}{U})^2\sum_{l=0}^{\infty}\frac{(2\alpha^2)^l}{l!}l^2-a^3(\frac{\omega_0}{U})^3\sum_{l=0}^{\infty}\frac{(2\alpha^2)^l}{l!}l^3+...\Bigg) \tag{A.4}$$

The first series gives $e^{2\alpha^2}$. The second one gives

$$\sum_{l=0}^{\infty}\frac{(2\alpha^2)^l}{l!}l=\sum_{l=1}^{\infty}\frac{(2\alpha^2)^l}{(l-1)!}=\sum_{m=0}^{\infty}\frac{(2\alpha^2)^{m+1}}{m!}=2\alpha^2\sum_{m=0}^{\infty}\frac{(2\alpha^2)^m}{m!}=2\alpha^2e^{2\alpha^2}. \tag{A.5}$$

The third series can be evaluated writing $l^2=l(l-1)+l$ in order to have the following expression:

$$\sum_{l=0}^{\infty}\frac{(2\alpha^2)^l}{l!}(l(l-1)+l)=\sum_{l=2}^{\infty}\frac{(2\alpha^2)^l}{(l-2)!}+\sum_{l=1}^{\infty}\frac{(2\alpha^2)^l}{(l-1)!}=\left((2\alpha^2)^2+2\alpha^2\right)e^{2\alpha^2} \tag{A.6}$$

The fourth one can be evaluated by writing $l^3=l(l-1)(l-2)+3l(l-1)+l$. This gives

$$\sum_{l=0}^{\infty}\frac{(2\alpha^2)^l}{l!}(l(l-1)(l-2)+3l(l-1)+l)=\left((2\alpha^2)^3+3(2\alpha^2)^2+2\alpha^2\right)e^{2\alpha^2} \tag{A.7}$$

In this way, Eq. (A.4) becomes

$$\begin{aligned} f(\alpha^2,\lambda,U) &= \frac{e^{2\alpha^2}}{1-\frac{\lambda D}{U}}\Bigg(1-a\frac{\omega_0}{U}2\alpha^2+a^2\left(\frac{\omega_0}{U}\right)^2\left(2\alpha^2\right)^2+a^2\left(\frac{\omega_0}{U}\right)^2 2\alpha^2+ \\ &\quad -a^3\left(\frac{\omega_0}{U}\right)^3(2\alpha^2)^3-3a^3\left(\frac{\omega_0}{U}\right)^3(2\alpha^2)^2-a^3\left(\frac{\omega_0}{U}\right)^3 2\alpha^2\Bigg) \\ &= \frac{e^{2\alpha^2}}{1-\frac{\lambda D}{U}}\Bigg(1-\frac{a\lambda D}{U}+\frac{a^2(\lambda D)^2}{U^2}+\frac{a^2\lambda D\omega_0}{U^2}+ \\ &\quad -\frac{a^3(\lambda D)^3}{U^3}-3\frac{a^3(\lambda D)^2\omega_0}{U^3}-\frac{a^3\lambda D\omega_0^2}{U^3}\Bigg) \end{aligned} \tag{A.8}$$

This expression is useful in the adiabatic limit ($\omega_0 \to 0$ at finite λ). In that case, in fact, all the terms proportional to ω_0 vanish, leaving us with a series that can be resummed:

$$1-\frac{a\lambda D}{U}+\left(\frac{a\lambda D}{U}\right)^2-\left(\frac{a\lambda D}{U}\right)^3...=\frac{1}{1+a\frac{\lambda D}{U}}=\frac{1}{1+\frac{\lambda D/U}{1-\lambda D/U}}=1-\frac{\lambda D}{U} \tag{A.9}$$

So, the adiabatic result is simply

$$f(\lambda,U,0)=e^{2\alpha^2} \tag{A.10}$$

and consequently

$$J_{PT} = \frac{4t^2}{U} \tag{A.11}$$

The expression (A.8) can be written as

$$\begin{aligned} f(\alpha^2, \lambda, U) &= \mathrm{e}^{2\alpha^2} \left(a - a^2 \frac{\lambda D}{U} + a^3 \frac{(\lambda D)^2}{U^2} + a^3 \frac{\lambda D \omega_0}{U^2} + \right. \\ & \left. -a^4 \frac{(\lambda D)^3}{U^3} - 3a^4 \frac{(\lambda D)^2 \omega_0}{U^3} - a^4 \frac{\lambda D \omega_0^2}{U^3} \right) \end{aligned} \tag{A.12}$$

$$\begin{aligned} f(\alpha^2, \lambda, U) &= \mathrm{e}^{2\alpha^2} \left(1 + \frac{\lambda D}{U} + (\frac{\lambda D}{U})^2 - \left[1 + 2\frac{\lambda D}{U} + 3(\frac{\lambda D}{U})^2 \right] \frac{\lambda D}{U} + \right. \\ & + \left[1 + 3\frac{\lambda D}{U} + 6(\frac{\lambda D}{U})^2 \right] (\frac{\lambda D}{U})^2 + \left[1 + 3\frac{\lambda D}{U} + 6(\frac{\lambda D}{U})^2 \right] \frac{\lambda D}{U^2} \omega_0 + \\ & - \left[1 + 4\frac{\lambda D}{U} + 10(\frac{\lambda D}{U})^2 \right] \frac{(\lambda D)^3}{U^3} - 3 \left[1 + 4\frac{\lambda D}{U} + 10(\frac{\lambda D}{U})^2 \right] \frac{(\lambda D)^2 \omega_0}{U^3} + \\ & \left. - \left[1 + 4\frac{\lambda D}{U} + 10(\frac{\lambda D}{U})^2 \right] \frac{\lambda D \omega_0^2}{U^3} \right) \\ &\simeq \mathrm{e}^{2\alpha^2} \left(1 + \frac{\lambda D}{U} - \frac{\lambda D}{U} + \frac{\lambda D \omega_0}{U^2} - \frac{\lambda D \omega_0^2}{U^3} \right) \end{aligned} \tag{A.13}$$

where, in the last passage, we have neglected $\mathcal{O}(\frac{\lambda D}{U})^2$ and higher terms. We are thus left with the following expression

$$f(\alpha^2, \lambda, U) = \mathrm{e}^{2\alpha^2} \left(1 + \frac{\lambda D}{U^2} \omega_0 - \frac{\lambda D}{U^3} \omega_0^2 \right) \tag{A.14}$$

that means

$$J_{PT}(t, \alpha^2, \lambda, U) = \frac{4t^2}{U} \left(1 + \frac{\omega_0}{U} \frac{\lambda D}{U} - \left(\frac{\omega_0}{U} \right)^2 \frac{\lambda D}{U} \right) \tag{A.15}$$

Going on in the expansion, the linear terms in λ can be resummed, to give

$$\begin{aligned} J_{PT}(t, \alpha^2, \lambda, U) &= \frac{4t^2}{U} \left(1 + \frac{\omega_0}{U} \frac{\lambda D}{U} \left[1 - \frac{\omega_0}{U} + \left(\frac{\omega_0}{U} \right)^2 - \cdots \right] \right) \\ &= \frac{4t^2}{U} \left(1 + \frac{\omega_0}{U} \frac{\lambda D}{U} \frac{1}{1 + \frac{\omega_0}{U}} \right) \end{aligned} \tag{A.16}$$

The Kondo coupling J_K given in Eq. (3.5) is equivalent to $J_{PT}(\sqrt{2}V, \alpha^2/2, \lambda/2, U/2)$, so, from A.16, its expansion, linearly in $\lambda D/U$, reads

$$J_K = \frac{16V^2}{U}\left(1 + \frac{\frac{2\omega_0}{U}}{1+\frac{2\omega_0}{U}}\frac{\lambda D}{U}\right) \tag{A.17}$$

As written in Sec. 3.3, this corresponds to the following expression for the coefficient η, introduced to take into account the screening of U, induced by λ:

$$\eta = \frac{2\omega_0/U}{1+2\omega_0/U} \tag{3.9}$$

This correctly reproduces the linear behavior for small ω_0/U and asymptotically reaches 1 for large ω_0/U (see Fig. 3.9).

Appendix B

Pairing and polarization crossovers from phonon distribution functions: An analytic example

In this Appendix we show how pair formation can be detected by studying the evolution of the distribution of the center of mass of the phonon path in imaginary time ("centroid") [117]. We address this question within a specific case which can be analytically solved: the Holstein model in the antiadiabatic limit. As we have shown in Sec.2.1.2, this is an attractive Hubbard model with $U = g'^2/K = \lambda D$. In the atomic limit, its Hamiltonian reads

$$H = -2U\hat{\rho}_z^2 + \frac{U}{2} \tag{B.1}$$

where the operator $\hat{\rho}_z$ is defined as

$$\hat{\rho}_z = \frac{1}{2}\left(\hat{n}_\uparrow + \hat{n}_\downarrow - 1\right) = \frac{1}{2}\left(\hat{n} - 1\right) \tag{B.2}$$

The partition function of this model can be easily derived. The quartic term can in fact be decoupled through a Hubbard-Stratonovich transformation:

$$\mathrm{e}^{-\beta H} = \int \frac{dY}{\sqrt{2\pi/\beta}} \mathrm{e}^{-\beta\frac{Y^2}{2} - 2\beta\sqrt{U}\hat{\rho}_z Y} \mathrm{e}^{-\beta\frac{U}{2}} \tag{B.3}$$

The Hubbard-Stratonovich Y field can be viewed as the Holstein phonon field in the antiadiabatic limit. In fact, apart from a rescaling of the chemical potential by U, the Holstein model in the antiadiabatic limit (in which the phonon has no kinetic term), is recovered with the following substitution:

$$Y = -X\sqrt{K} + \sqrt{U} = -X\sqrt{M\omega_0^2} + \sqrt{U} \tag{B.4}$$

$\hat{\rho}_z$ can assume three values

$$\rho_\alpha = \begin{cases} -1/2 & \longleftrightarrow & |0\rangle \\ 0 & \longleftrightarrow & |\uparrow\rangle, |\downarrow\rangle \\ 1/2 & \longleftrightarrow & |\uparrow\downarrow\rangle \end{cases} \tag{B.5}$$

The partition function can thus be written in terms of the following Gaussian integral:

$$\begin{aligned} \mathrm{Tr}\,\mathrm{e}^{-\beta H} &= \int \frac{dY}{\sqrt{2\pi/\beta}} \mathrm{e}^{-\beta\frac{Y^2}{2}} \mathrm{e}^{-\beta\frac{U}{2}}\, \mathrm{Tr}\,\mathrm{e}^{-2\beta\sqrt{U}\hat{\rho}_z Y} \\ &= \sum_\alpha \int \frac{dY}{\sqrt{2\pi/\beta}} \mathrm{e}^{-\beta\frac{Y^2}{2} - 2\beta\sqrt{U}\rho_\alpha Y} \mathrm{e}^{-\beta\frac{U}{2}} \end{aligned} \tag{B.6}$$

We have therefore introduced the Hubbard-Stratonovich field Y which couples to $\hat{\rho}_z$ in the Hamiltonian of the atomic attractive Hubbard model. Now we calculate the same partition function within a path-integral approach and, once we have introduced the path in imaginary time, we want to understand what is the object in imaginary time which couples to $\hat{\rho}_z$, i.e. the object which plays the role of Y.

For this purpose we divide the interval $[0;\beta]$ in L time slices, as in the Quantum Monte Carlo formulation, described in Sec. 2.3.2. $L-1$ identities are inserted in the expression for the partition function:

$$\mathrm{Tr}\,\mathrm{e}^{-\beta H} = \sum_\alpha \sum_{\alpha_1,\alpha_2,\ldots,\alpha_{L-1}} \langle\alpha|\mathrm{e}^{-\tau H}|\alpha_1\rangle\langle\alpha_1|\mathrm{e}^{-\tau H}|\alpha_2\rangle \ldots .\langle\alpha_{L-1}|\mathrm{e}^{-\tau H}|\alpha\rangle \tag{B.7}$$

Introducing L Hubbard-Stratonovich fields y_k, each bracket in Eq. (B.7) can be written as

$$\langle\alpha_k|\mathrm{e}^{-\tau H}|\alpha_{k+1}\rangle = \int \frac{dy_k}{\sqrt{2\pi/\tau}} \mathrm{e}^{-\tau\frac{y_k^2}{2} - 2\tau\sqrt{U}\rho_{\alpha_k} y_k} \mathrm{e}^{-\tau\frac{U}{2}} \delta_{\alpha_k,\alpha_{k+1}} \tag{B.8}$$

Eq. (B.7) becomes therefore

$$\begin{aligned} \mathrm{Tr}\,\mathrm{e}^{-\beta H} &= \sum_\alpha \prod_{k=0}^{L-1} \left(\int \frac{dy_k}{\sqrt{2\pi/\tau}} \mathrm{e}^{-\tau\frac{y_k^2}{2} - 2\tau\sqrt{U}\rho_\alpha y_k} \mathrm{e}^{-\tau\frac{U}{2}} \right) \\ &= \sum_\alpha \int \left(\prod_{k=0}^{L-1} \frac{dy_k}{\sqrt{2\pi/\tau}} \right) \mathrm{e}^{-\frac{1}{2}\sum_k \tau y_k^2 - 2\sqrt{U}\rho_\alpha \sum_k \tau y_k} \mathrm{e}^{-\beta\frac{U}{2}} \end{aligned} \tag{B.9}$$

Let us introduce now the centroid Y_c of the imaginary-time path:

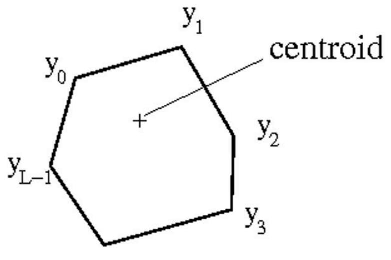

Figure B.1: Schematic picture of the centroid of the imaginary path

$$Y_c = \frac{1}{\beta}\sum_{k=0}^{L-1} \tau y_k \tag{B.10}$$

In terms of Y_c, the partition function (B.9) is

$$\mathrm{Tr}\,\mathrm{e}^{-\beta H} = \sum_\alpha \int d(\beta Y_c) \int \left(\prod_{k=0}^{L-1} \frac{dy_k}{\sqrt{2\pi/\tau}}\right) \delta\left(\beta Y_c - \sum_{k=0}^{L-1} \tau y_k\right) \mathrm{e}^{-\frac{1}{2}\sum_k \tau y_k^2 - 2\sqrt{U}\rho_\alpha \beta Y_c} \mathrm{e}^{-\beta\frac{U}{2}} \tag{B.11}$$

Since we have to express all terms in Eq. (B.11) in terms of the centroid coordinate, we must deal with the following integral:

$$\int \left(\prod_{k=0}^{L-1} \frac{dy_k}{\sqrt{2\pi/\tau}}\right) \delta\left(\beta Y_c - \sum_{k=0}^{L-1} \tau y_k\right) \mathrm{e}^{-\frac{1}{2}\sum_k \tau y_k^2} \tag{B.12}$$

By shifting all the y_k:

$$y_k = Y_c + u_k \tag{B.13}$$

the δ function becomes

$$\delta\left(\beta Y_c - \sum_{k=0}^{L-1} \tau (Y_c + u_k)\right) = \delta\left(\sum_{k=0}^{L-1} \tau u_k\right) \tag{B.14}$$

and the integral in Eq. (B.12)

$$\int \left(\prod_{k=0}^{L-1} \frac{du_k}{\sqrt{2\pi/\tau}}\right) \delta\left(\sum_{k=0}^{L-1} \tau u_k\right) \mathrm{e}^{-\frac{1}{2}\sum_k \tau (Y_c + u_k)^2} \tag{B.15}$$

This is equal to

$$\mathrm{e}^{-\frac{1}{2}\beta Y_c^2} \int \left(\prod_{k=0}^{L-1} \frac{du_k}{\sqrt{2\pi/\tau}}\right) \delta\left(\sum_{k=0}^{L-1} \tau u_k\right) \mathrm{e}^{-Y_c \sum_k \tau u_k - \frac{1}{2}\sum_k \tau u_k^2} \tag{B.16}$$

and, in turn, to

$$\mathrm{e}^{-\frac{1}{2}\beta Y_c^2}\int\left(\prod_{k=0}^{L-1}\frac{du_k}{\sqrt{2\pi/\tau}}\right)\delta\left(\sum_{k=0}^{L-1}\tau u_k\right)\mathrm{e}^{-\frac{1}{2}\sum_k \tau u_k^2} \tag{B.17}$$

with no dependence on Y_c. We denote the integral in (B.17) by $c_L(\tau)$ and solve it explicitly. The solution can be found by isolating the contribution from the "endpoint" of the imaginary-time path:

$$\sum_{k=0}^{L-1}\tau u_k = \tau u_0 + \sum_{k=1}^{L-1}\tau u_k \tag{B.18}$$

Then

$$\begin{aligned}
c_L(\tau) &= \int\frac{du_0}{\sqrt{2\pi/\tau}}\int\left(\prod_{k=1}^{L-1}\frac{du_k}{\sqrt{2\pi/\tau}}\right)\delta\left(\tau u_0+\sum_{k=1}^{L-1}\tau u_k\right)\mathrm{e}^{-\frac{1}{2}\tau u_0^2}\mathrm{e}^{-\frac{1}{2}\sum_{k=1}^{L-1}\tau u_k^2} \\
&= \frac{1}{\sqrt{2\pi\tau}}\int\left(\prod_{k=1}^{L-1}\frac{du_k}{\sqrt{2\pi/\tau}}\right)\mathrm{e}^{-\frac{1}{2\tau}\left(\sum_{k=1}^{L-1}\tau u_k\right)^2-\frac{1}{2}\sum_{k=1}^{L-1}\tau u_k^2} \\
&= \frac{1}{\sqrt{2\pi\tau}}\left(\prod_{k=1}^{L-1}\frac{1}{\sqrt{2\pi/\tau}}\right)\left(\prod_{k=1}^{L-1}\frac{1}{\sqrt{2\pi}}\right)\frac{1}{(\det\mathcal{A}^{-1})^{1/2}} \\
&= (2\pi)^{-L+\frac{1}{2}}\,\tau^{\frac{L}{2}-1}\frac{1}{(\det\mathcal{A}^{-1})^{1/2}}
\end{aligned} \tag{B.19}$$

where the fermionic matrix $\mathcal{A}$ is given by

$$\mathcal{A}=\begin{pmatrix} 2 & 1 & 1 & \cdots \\ 1 & 2 & 1 & \ddots \\ 1 & 1 & \ddots & \ddots \\ \vdots & \vdots & \ddots & \ddots \end{pmatrix} \tag{B.20}$$

The partition function (B.11) is thus given by

$$\mathrm{Tr}\,\mathrm{e}^{-\beta H} = \beta c_L(\tau)\sum_\alpha\int dY_c\mathrm{e}^{-\beta\frac{Y_c^2}{2}-2\beta\sqrt{U}\rho_\alpha Y_c}\mathrm{e}^{-\beta\frac{U}{2}} \tag{B.21}$$

Apart from unimportant constant factors, this expression is the same as Eq. (B.6). We have therefore shown that the centroid of the Hubbard-Stratonovich field's path in imaginary-time is the object that couples to $\hat{\rho}_z$.

We can define the distribution function of the centroid:

$$P(Y_c)=\frac{1}{\mathcal{Z}}\sum_\alpha\beta c_L(\tau)\mathrm{e}^{-\beta\frac{Y_c^2}{2}-2\beta\sqrt{U}\rho_\alpha Y_c-\beta\frac{U}{2}} \tag{B.22}$$

which is a well-defined distribution in the limit $\tau \to 0$. The sum over α can be easily carried out:

$$\sum_{\alpha} \mathrm{e}^{-2\beta\sqrt{U}\rho_\alpha Y_c} = 2\left[\cosh(\beta\sqrt{U}Y_c) + 1\right] \tag{B.23}$$

and $P(Y_c)$ becomes

$$P(Y_c) = \frac{1}{\mathcal{N}}\mathrm{e}^{-\beta V(Y_c)} \tag{B.24}$$

where $\mathcal{N}$ is a finite normalization factor and

$$V(Y_c) = \frac{1}{2}Y_c^2 - \frac{1}{\beta}\log\left\{2\left[\cosh(\beta\sqrt{U}Y_c) + 1\right]\right\} \tag{B.25}$$

In Fig. (B.2), the evolution of $V(Y_c)$ with T is reported. It can be seen that, at low temperatures, the double-well characteristic is obtained. Meanwhile, $P(Y_c)$ assumes the bimodal shape and the empty or double-occupied configurations become more likely than the single-occupied one. At high temperatures, the monomodal shape is obtained and the single-occupied configurations are privileged.

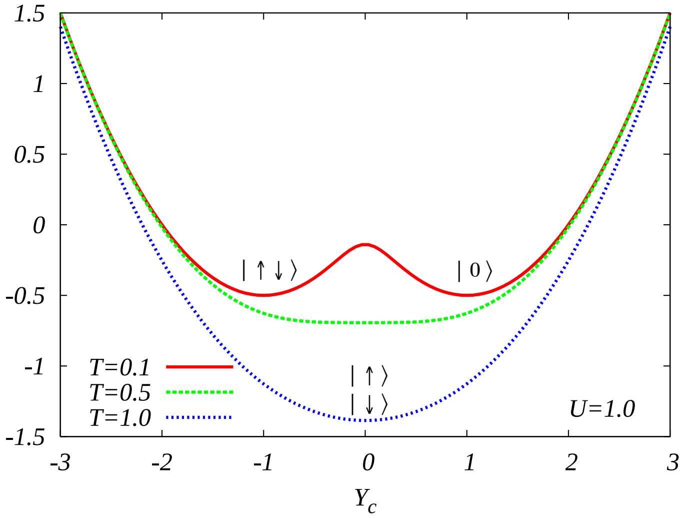

Figure B.2: Evolution of $V(Y_c)$ with T.

In the attractive Hubbard model in the atomic limit, we have therefore explicitly found a crossover from a low-temperature regime characterized by incoherent pairs to a normal high-temperature one. The value of the temperature at which the crossover takes place, can be unambiguously placed by following the evolution of the distribution of the centroid of the Hubbard-Stratonovich (phonon) field's path. The probability distribution function of the endpoint y_0 of the path can be calculated following the same algebra and the result is a Gaussian distribution of variance proportional to $1/\tau$. This means that the probability of the endpoint is always unimodal in the antiadiabatic limit.

List of Figures

Bibliography

[1] M. Capone, G. Sangiovanni, C. Castellani, C. Di Castro *et al.* *Phys. Rev. Lett.* **92**, 106401 (2004)

[2] G. Sangiovanni, M. Capone, C. Castellani and M. Grilli. *Phys. Rev. Lett.* (2004). (in press) - cond-mat/0409510

[3] M. Capone and S. Ciuchi. *Phys. Rev. Lett.* **91**, 186405 (2003)

[4] M. Capone, S. Ciuchi and G. Sangiovanni. (unpublished)

[5] J. Hubbard. *Proc. R. Soc. London, A* **276**, 238 (1963)

[6] E. Dagotto. *Rev. Mod. Phys.* **66**, 763 (1994)

[7] F. C. Zhang and T. M. Rice. *Phys. Rev. B* **37**, 3759 (1988)

[8] P. W. Anderson. *Science* **235**, 1196 (1987)

[9] S. Sorella, G. Martins, F. Becca, C. Gazza *et al.* *Phys. Rev. Lett.* **88**, 117002 (2002)

[10] Y. Yanase, T. Jujo, T. Nomura, H. Ikeda *et al.* *Physics Reports* **387**, 1 (2003)

[11] D. Duffy, A. Nazarenko, S. Haas, A. Moreo *et al.* *Phys. Rev. B* **56**, 5597 (1997)

[12] A. Paramekanti, M. Randeria and N. Trivedi. *Phys. Rev. Lett.* **87**, 217002 (2001)

[13] M. Capone, M. Fabrizio, C. Castellani and E. Tosatti. *Science* **296**, 2364 (2002)

[14] M. Capone, M. Fabrizio, C. Castellani and E. Tosatti. *Phys. Rev. Lett.* **93**, 047001 (2004)

[15] B. Batlogg, R. J. Cava, A. Jayaraman, R. B. van Dover *et al.* *Phys. Rev. Lett.* **58**, 2333 (1987)

[16] P. Franck, J. Jung, M. A.-K. Mohamed, S. Gygax *et al.* *Phys. Rev. B* **44**, 5318 (1991)

[17] T. Schneider and H. Keller. *Phys. Rev. Lett.* **69**, 3374 (1992)

[18] Guo-Meng Zhao, M. B. Hunt, H. Keller and K. A. Müller. *Nature (London)* **385**, 236 (1997)

[19] J. Hofer, K. Conder, T. Sasagawa, Guo-Meng Zhao *et al.* *Phys. Rev. Lett.* **84**, 4192 (2000)

[20] R. Khasanov, A. Shengelaya, K. Conder, E. Morenzoni *et al.* *J. Phys.: Condens. Matter* **15**, L17 (2003)

[21] R. Khasanov, D. G. Eshchenko, H. Luetkens, E. Morenzoni *et al.* *Phys. Rev. Lett.* **92**, 057602 (2004)

[22] A. B. Migdal. *Zh. Éksp. Teor. Fiz.* **34**, 1438 (1958). [Sov. Phys. JETP **7**, 996 (1958)]

[23] A. A. Abrikosov, L. P. Gorkov and I. E. Dzyaloshinski. *Methods of Quantum Field Theory in Statistical Physics* (Dover Publications, 1963)

[24] D. R. Temprano, J. Mesot, S. Janssen, K. Conder *et al.* *Phys. Rev. Lett.* **84**, 1990 (2000)

[25] S. Andergassen, S. Caprara, C. Di Castro and M. Grilli. *Phys. Rev. Lett.* **87**, 056401 (2001)

[26] P. Paci, M. Capone, E. Cappelluti, S. Ciuchi *et al.* (2004). cond-mat/0405053

[27] S. L. Chaplot, W. Reichardt, L. Pintschovius and N. Pyka. *Phys. Rev. B* **52**, 7230 (1995)

[28] L. Pintschovius and W. Reichardt. In A. Furrer, editor, *Neutron Scattering in Layered Copper-Oxide Superconductors*, volume 20, page 165 (Kluwer Academic, Dordrecht, 1998)

[29] L. Pintschovius and M. Braden. *Phys. Rev. B* **60**, 15039 (1999)

[30] R. J. McQueeney, Y. Petrov, T. Egami, M. Yethiraj *et al.* *Phys. Rev. Lett.* **82**, 628 (1999)

[31] L. Pintschovius, D. Reznik, W. Reichardt, Y. Endoh *et al.* *Phys. Rev. B* **69**, 214506 (2004)

[32] O. Rösch and O. Gunnarsson. *Phys. Rev. Lett.* **92**, 146403 (2004)

[33] P. V. Bogdanov, A. Lanzara, S. A. Kellar, X. J. Zhou *et al.* *Phys. Rev. Lett.* **85**, 2581 (2000)

[34] A. Lanzara, P. V. Bogdanov, X. J. Zhou, S. A. Kellar *et al.* *Nature* **412**, 510 (2001)

[35] X. J. Zhou, T. Yoshida, A. Lanzara, P. V. Bogdanov *et al.* *Nature (London)* **423**, 398 (2003)

[36] T. Cuk, F. Baumberger, D. H. Lu, N. Ingle *et al.* *Phys. Rev. Lett.* **93**, 117003 (2004)

[37] J. Hwang, T. Timusk and G. D. Gu. *Nature (London)* **427**, 714 (2004)

[38] A. Kaminski, M. Randeria, J. C. Campuzano, M. R. Norman *et al.* *Phys. Rev. Lett.* **86**, 1070 (2001)

[39] G. Seibold and M. Grilli (2004). cond-mat/0409506

[40] T. P. Devereaux, T. Cuk, Z.-X. Shen and N. Nagaosa. *Phys. Rev. Lett.* **93**, 117004 (2004)

[41] G.-H. Gweon, T. Sasagawa, S. Y. Zhou, J. Graf *et al.* *Nature (London)* **430**, 187 (2004)

[42] M. C. Gutzwiller. *Phys. Rev. Lett.* **10**, 159 (1963)

[43] J. Kanamori. *Prog. Theor. Phys.* **30**, 275 (1963)

[44] R. Peierls. *Proc. Phys. Soc. London, A* **49**, 72 (1937)

[45] N. F. Mott. *Proc. Phys. Soc. London, A* **62**, 416 (1949)

[46] J. C. Slater. *Phys. Rev.* **82**, 538 (1951)

[47] A. Georges, G. Kotliar, W. Krauth and M. J. Rozenberg. *Rev. Mod. Phys.* **68**, 13 (1996)

[48] W. F. Brinkman and T. M. Rice. *Phys. Rev. B* **2**, 4302 (1970)

[49] G. Kotliar and A. E. Ruckenstein. *Phys. Rev. Lett.* **57**, 1362 (1986)

[50] R. Raimondi and C. Castellani. *Phys. Rev. B* **48**, 11453 (1993)

[51] C. Castellani, G. Kotliar, R. Raimondi, M. Grilli *et al.* *Phys. Rev. Lett.* **69**, 2009 (1992)

[52] D. B. McWhan, A. Menth, J. P. Remeika, W. F. Brinkman *et al.* *Phys. Rev. B* **7**, 1920 (1973)

[53] G. Kotliar and D. Vollhardt. *Physics Today* **57**, 3 (March), 53 (2004)

[54] P. Limelette, A. Georges, D. Jérome, P. Wzietek *et al.* *Science* **302**, 89 (2003)

[55] P. Limelette, P. Wzietek, S. Florens, A. Georges *et al.* *Phys. Rev. Lett.* **91**, 016401 (2003)

[56] T. Holstein. *Ann. Phys* **8**, 325 (1959)

[57] T. Holstein. *Ann. Phys* **8**, 343 (1959)

[58] M. Capone, W. Stephan and M. Grilli. *Phys. Rev. B* **56**, 4484 (1997)

[59] S. Ciuchi, F. de Pasquale, S. Fratini and D. Feinberg. *Phys. Rev. B* **56**, 4494 (1997)

[60] M. Capone, C. Grimaldi and S. Ciuchi. *Europhys. Lett.* **42**, 523 (1998)

[61] I. G. Lang and Y. A. Firsov. *Zh. Éksp. Teor. Fiz.* **42**, 1843 (1962). [Sov. Phys. JETP **16**, 1301 (1963)]

[62] R. T. Scalettar, N. E. Bickers and D. J. Scalapino. *Phys. Rev. B* **40**, 197 (1989)

[63] S. Engelsberg and J. R. Schrieffer. *Phys. Rev.* **131**, 993 (1963)

[64] L. Pietronero, S. Strässler and C. Grimaldi. *Phys. Rev. B* **52**, 10516 (1995)

[65] C. Grimaldi, L. Pietronero and S. Strässler. *Phys. Rev. B* **52**, 10530 (1995)

[66] E. Cappelluti, C. Grimaldi, L. Pietronero and S. Stässler. *Phys. Rev. Lett.* **85**, 4771 (2000)

[67] D. Meyer, A. Hewson and R. Bulla. *Phys. Rev. Lett.* **89**, 196401 (2002)

[68] J. E. Hirsch and E. Fradkin. *Phys. Rev. B* **27**, 4302 (1983)

[69] H. D. Raedt and A. Lagendijk. *Phys. Rev. B* **27**, 6097 (1983)

[70] H. D. Raedt and A. Lagendijk. *Phys. Rev. B* **30**, 1671 (1984)

[71] M. Hohenadler, H. G. Evertz and W. von der Linden. *Phys. Rev. B* **69**, 024301 (2004)

[72] M. Grilli and C. Castellani. *Phys. Rev. B* **50**, 16880 (1994)

[73] F. Becca, M. Tarquini, M. Grilli and C. Di Castro. *Phys. Rev. B* **54**, 12443 (1996)

[74] E. Cappelluti, B. Cerruti and L. Pietronero. *Phys. Rev. B* **69**, 161101(R) (2004)

[75] R. Zeyher and M. Kulic. *Phys. Rev. B* **53**, 2850 (1996)

[76] R. Blankenbecler, D. J. Scalapino and R. L. Sugar. *Phys. Rev. D* **24**, 2278 (1981)

[77] J. E. Hirsch and R. M. Fye. *Phys. Rev. Lett.* **56**, 2521 (1986)

[78] Z. B. Huang, W. Hanke, E. Arrigoni and D. J. Scalapino. *Phys. Rev. B* **68**, 220507 (2003)

[79] W. Metzner and D. Vollhardt. *Phys. Rev. Lett.* **62**, 324 (1989)

[80] R. Bulla, T. A. Costi and D. Vollhardt. *Phys. Rev. B* **64**, 045103 (2001)

[81] J. Schlipf, M. Jarrell, P. G. J. van Dongen, N. Blümer *et al.* *Phys. Rev. Lett.* **82**, 4890 (1999)

[82] M. J. Rozenberg, R. Chitra and G. Kotliar. *Phys. Rev. Lett.* **83**, 3498 (1999)

[83] H. Kajueter, G. Kotliar and G. Moeller. *Phys. Rev. B* **53**, 16214 (1996)

[84] D. S. Fisher, G. Kotliar and G. Moeller. *Phys. Rev. B* **52**, 17112 (1995)

[85] A. Georges and W. Krauth. *Phys. Rev. B* **48**, 7167 (1993)

[86] M. J. Rozenberg, G. Kotliar and X. Y. Zhang. *Phys. Rev. B* **49**, 10181 (1994)

[87] R. Micnas, J. Ranninger and S. Robaszkiewicz. *Rev. Mod. Phys.* **62**, 113 (1990)

[88] A. J. Millis, R. Mueller and B. I. Shraiman. *Phys. Rev. B* **54**, 5389 (1996)

[89] A. C. Hewson and D. Meyer. *J. Phys.: Condens. Matter* **14**, 427 (2002)

[90] M. Caffarel and W. Krauth. *Phys. Rev. Lett.* **72**, 1545 (1994)

[91] Y. Motome and G. Kotliar. *Phys. Rev. B* **62**, 12800 (2000)

[92] J. K. Freericks, M. Jarrell and D. J. Scalapino. *Phys. Rev. B* **48**, 6302 (1993)

[93] J. K. Freericks and M. Jarrell. *Phys. Rev. Lett.* **75**, 2570 (1995)

[94] Gun Sang Jeon, Tae-Ho Park, Jung Hoon Han, Hyun C. Lee *et al.* *Phys. Rev. B* **70**, 125114 (2004)

[95] W. Koller, D. Meyer, Y. Ōno and A. C. Hewson. *Europhys. Lett.* **66**, 559 (2004)

[96] P. S. Cornaglia, H. Ness and D. R. Grempel. *Phys. Rev. Lett.* **93**, 147201 (2004)

[97] P. S. Cornaglia, H. Ness and D. R. Grempel (2004). cond-mat/0409021

[98] W. Stephan, M. Capone, M. Grilli and C. Castellani. *Phys. Lett. A* **227**, 120 (1997)

[99] R. Zitzler, T. Pruschke and R. Bulla. *Eur. Phys. J. B* **27**, 473 (2002)

[100] G. Kotliar, S. Murthy and M. J. Rozenberg. *Phys. Rev. Lett.* **89**, 046401 (2002)

[101] H. B. Callen. *Thermodynamics: an introduction to the physical theories of equilibrium thermostatics and irreversible thermodynamics* (John Wiley and Sons, New York, 1960)

[102] D. Feinberg, S. Ciuchi and F. de Pasquale. *Int. J. Mod. Phys. B* **4**, 1317 (1990)

[103] A. Ino, T. Mizokawa, A. Fujimori, K. Tamasaku *et al.* *Phys. Rev. Lett.* **79**, 2101 (1996)

[104] I. Bozovic, G. Logvenov, M. A. J. Verhoeven, P. Caputo *et al.* *Nature* **422**, 873 (2003)

[105] K. A. Müller, Guo-Meng Zhao, K. Conder and H. Keller. *J. Phys.: Condens. Matter* **10**, L291 (1998)

[106] A. Deppeler and A. J. Millis. *Phys. Rev. B* **65**, 100301 (2002)

[107] A. Deppeler and A. J. Millis. *Phys. Rev. B* **65**, 224301 (2002)

[108] A. Deppeler and A. J. Millis (2002). cond-mat/0204617

[109] P. Nozières. *Theory of Interacting Fermi Systems* (W. A. Benjamin, New York, 1964)

[110] A. Auerbach. *Interacting Elecetrons and Quantum Magnetism* (Springer-Verlag, New York, 1994)

[111] S.-K. Mo, H.-D. Kim, J. W. Allen, G.-H. Gweon *et al.* *Phys. Rev. Lett.* **93**, 076404 (2004)

[112] S. Paganelli and S.Ciuchi. private communication

[113] A. Toschi, P. Barone, M. Capone and C. Castellani. *New Jour. of Phys.* (2004). (in press) - cond-mat/0411637

[114] A. Sewer, X. Zotos and H. Beck. *Phys. Rev. B* **66**, 140504(R) (2002)

[115] J. M. Singer, M. H. Pedersen, T. Schneider, H. Beck *et al.* *Phys. Rev. B* **54**, 1286 (1996)

[116] J. M. Singer, T. Schneider and M. H. Pedersen. *Eur. Phys. J. B* **2**, 17 (1998)

[117] F. de Pasquale and S. Ciuchi. *Physica B* **284-288**, 1573 (2000)